The QCD Pomeron with optimal renormalization

S. J. Brodsky
Stanford Linear Accelerator Center, Stanford University, Stanford, CA 94309, USA

V. S. Fadin
Budker Institute of Nuclear Physics, 630090 Novosibirsk, Russia

V. T. Kim
St. Petersburg Nuclear Physics Institute, 188350 Gatchina, Russia; International Institute of Theoretical and Applied Physics, Ames, IA 50011, USA

L. N. Lipatov
St. Petersburg Nuclear Physics Institute, 188350 Gatchina, Russia

G. B. Pivovarov*)
Institute for Nuclear Research, 117312 Moscow, Russia; International Institute of Theoretical and Applied Physics, Ames, IA 50011, USA

(Submitted 18 June 1999)
Pis'ma Zh. Éksp. Teor. Fiz. **70**, No. 3, 161–166 (10 August 1999)

It is shown that the next-to-leading order (NLO) corrections to the QCD Pomeron intercept obtained from the Balitsky–Fadin–Kuraev–Lipatov (BFKL) equation, when evaluated in non-Abelian physical renormalization schemes with Brodsky–Lepage–Mackenzie (BLM) optimal scale setting, do not exhibit the serious problems encountered in the $\overline{MS}$ scheme. A striking feature of the NLO BFKL Pomeron intercept in the BLM approach is that it yields an important approximate conformal invariance. © *1999 American Institute of Physics.* [S0021-3640(99)00115-2]

PACS numbers: 12.38.Cy, 11.10.Gh

The discovery of rapidly increasing structure functions in deep inelastic scattering at HERA at small-x is in agreement with the expectations of the QCD high-energy limit. The Balitsky–Fadin–Kuraev–Lipatov (BFKL)[1] resummation of energy logarithms is anticipated to be an important tool for exploring this limit. The highest eigenvalue, $\omega^{\max}$, of the leading order BFKL equation[1] is related to the intercept of the Pomeron which in turn governs the high-energy asymptotics of the cross sections: $\sigma \sim s^{\alpha_{IP}-1} = s^{\omega^{\max}}$. The BFKL Pomeron intercept in LO turns out to be rather large: $\alpha_{IP}-1=\omega_L^{\max}=12\ln 2\,(\alpha_S/\pi)$ $\simeq 0.55$ for $\alpha_S=0.2$; hence, it is very important to know the next-to-leading order (NLO) corrections.

Recently the NLO corrections to the BFKL resummation of energy logarithms were calculated; see Refs. 2 and 3 and references therein. The NLO corrections[2,3] to the highest eigenvalue of the BFKL equation turn out to be negative and even larger than the LO contribution for $\alpha_S > 0.157$. However, one should stress that the NLO calculations, as

any finite-order perturbative results, contain both renormalization scheme and renormalization scale ambiguities. The NLO BFKL calculations[2,3] were performed by employing the modified minimal subtraction scheme ($\overline{MS}$) to regulate the ultraviolet divergences with arbitrary scale setting.

In this work we consider the NLO BFKL resummation of energy logarithms[2,3] in physical renormalization schemes in order to study the renormalization scheme dependence. To resolve the renormalization scale ambiguity we utilize Brodsky–Lepage–Mackenzie (BLM) optimal scale setting.[4] We show that the reliability of QCD predictions for the intercept of the BFKL Pomeron at NLO when evaluated using BLM scale setting within non-Abelian physical schemes, such as the momentum space subtraction (MOM) scheme[5] or the Υ scheme based on $\Upsilon \to ggg$ decay, is significantly improved compared to the $\overline{MS}$ scheme result.[2,3]

We begin with the representation of the $\overline{MS}$-result of NLO BFKL[2,3] in physical renormalization schemes. The eigenvalue of the NLO BFKL equation at transferred momentum squared $t=0$ in the $\overline{MS}$ scheme[2,3] can be represented as the action of the NLO BFKL kernel (averaged over azimuthal angle) on the leading order eigenfunctions $(Q_2^2/Q_1^2)^{-1/2+i\nu}$ (Ref. 2):

$$\omega_{\overline{MS}}(Q_1^2,\nu)=\int d^2Q_2\ K_{\overline{MS}}(\mathbf{Q}_1,\mathbf{Q}_2)\left(\frac{Q_2^2}{Q_1^2}\right)^{-\frac{1}{2}+i\nu}$$
$$=N_C\chi_L(\nu)\frac{\alpha_{\overline{MS}}(Q_1^2)}{\pi}\left[1+r_{\overline{MS}}(\nu)\frac{\alpha_{\overline{MS}}(Q_1^2)}{\pi}\right], \tag{1}$$

where

$$\chi_L(\nu)=2\psi(1)-\psi(1/2+i\nu)-\psi(1/2-i\nu)$$

is the function related with the leading order eigenvalue, $\psi=\Gamma'/\Gamma$ denotes the Euler ψ function, the ν variable is conformal weight parameter,[6] N_C is the number of colors, and $Q_{1,2}$ are the virtualities of the reggeized gluons.

The calculations of Refs. 2 and 3 allow us to decompose the NLO coefficient $r_{\overline{MS}}$ of Eq. (1) into β-dependent and conformal (β-independent) parts:

$$r_{\overline{MS}}(\nu)=r^{\beta}_{\overline{MS}}(\nu)+r^{\rm conf}_{\overline{MS}}(\nu), \tag{2}$$

where

$$r^{\beta}_{\overline{MS}}(\nu)=-\frac{\beta_0}{4}\left[\frac{1}{2}\chi_L(\nu)-\frac{5}{3}\right] \tag{3}$$

and

$$r^{\rm conf}_{\overline{MS}}(\nu)=-\frac{N_C}{4\chi_L(\nu)}\left[\frac{\pi^2\sinh(\pi\nu)}{2\nu\cosh^2(\pi\nu)}\left(3+\left(1+\frac{N_F}{N_C^3}\right)\frac{11+12\nu^2}{16(1+\nu^2)}\right)\right.$$
$$\left.-\chi_L''(\nu)+\frac{\pi^2-4}{3}\chi_L(\nu)-\frac{\pi^3}{\cosh(\pi\nu)}-6\zeta(3)+4\varphi(\nu)\right] \tag{4}$$

with

$$\varphi(\nu)=2\int_0^1 dx\,\frac{\cos(\nu\ln(x))}{(1+x)\sqrt{x}}\left[\frac{\pi^2}{6}-\mathrm{Li}_2(x)\right],\quad \mathrm{Li}_2(x)=-\int_0^x dt\,\frac{\ln(1-t)}{t}. \tag{5}$$

Here $\beta_0=(11/3)N_C-(2/3)N_F$ is the leading coefficient of the QCD β function, N_F is the number of flavors, $\zeta(n)$ stands for the Riemann zeta function, $\mathrm{Li}_2(x)$ is the Euler dilogarithm (Spence function). In Eq. (4) N_F denotes flavor number of the Abelian part of the $gg\to q\bar{q}$ process contribution. The Abelian part is not associated with the running of the coupling[7] and is consistent with the corresponding QED result for the $\gamma^*\gamma^*\to e^+e^-$ cross section.[8]

The β-dependent NLO coefficient $r_{\overline{MS}}^{\beta}(\nu)$, which is related to the running of the coupling, receives contributions from the gluon reggeization diagrams, from the virtual part of the one-gluon emission, from the real two-gluon emission, and from the non-Abelian part[7] of the $gg\to q\bar{q}$ process.

The NLO BFKL Pomeron intercept then reads for $N_C=3$ (Ref. 2):

$$\alpha_{IP}^{\overline{MS}}-1=\omega_{\overline{MS}}(Q^2,0)=12\ln 2\,\frac{\alpha_{\overline{MS}}(Q^2)}{\pi}\left[1+r_{\overline{MS}}(0)\,\frac{\alpha_{\overline{MS}}(Q^2)}{\pi}\right]; \tag{6}$$

$$r_{\overline{MS}}(0)\simeq -20.12-0.1020N_F+0.06692\beta_0, \tag{7}$$

$$r_{\overline{MS}}(0)_{|N_F=4}\simeq -19.99.$$

One of the most popular physical schemes is the MOM scheme,[5] based on renormalization of the triple-gluon vertex at some symmetric off-shell momentum. In order to eliminate the dependence on gauge choice and other theoretical conventions inherent to the MOM scheme, one can consider renormalization schemes based on physical processes,[4] e.g., V scheme based on heavy quark potential or Υ scheme based on $\Upsilon\to ggg$ decay.[9]

A finite renormalization due to the change of scheme can be accomplished by a transformation of the QCD coupling:[5]

$$\alpha_S\to\alpha_S\left[1+T\frac{\alpha_S}{\pi}\right], \tag{8}$$

where T is some function of N_C, N_F, and for the MOM scheme, of a gauge parameter ξ. Then the NLO BFKL eigenvalue in the MOM scheme can be represented as follows

$$\omega_{\mathrm{MOM}}(Q^2,\nu)=N_C\chi_L(\nu)\,\frac{\alpha_{\mathrm{MOM}}(Q^2)}{\pi}\left[1+r_{\mathrm{MOM}}(\nu)\,\frac{\alpha_{\mathrm{MOM}}(Q^2)}{\pi}\right],$$

$$r_{\mathrm{MOM}}(\nu)=r_{\overline{MS}}(\nu)+T_{\mathrm{MOM}}. \tag{9}$$

The corresponding T function for the transition from the $\overline{MS}$ scheme to the MOM-, V- and Υ-schemes can be found from Refs. 5, 4, and 9 (Table I).

One can see from Table I that in spite of a weak renormalization scheme dependence the problem of a large NLO BFKL coefficient remains. The large size of the perturbative corrections leads to significant renormalization scale ambiguity. The renormalization

TABLE I. Scheme-transition function and the NLO BFKL coefficient in physical schemes.

Scheme		$T=T^{\rm conf}+T^{\beta}$	$r(0)=r^{\rm conf}(0)+r^{\beta}(0)$	$r(0)$ $(N_F=4)$
MOM	$\xi=0$	$7.471-1.281\beta_0$	$-12.64-0.1020N_F-1.214\beta_0$	-22.76
	$\xi=1$	$8.247-1.281\beta_0$	$-11.87-0.1020N_F-1.214\beta_0$	-21.99
	$\xi=3$	$8.790-1.281\beta_0$	$-11.33-0.1020N_F-1.214\beta_0$	-21.44
V		$2-0.4167\beta_0$	$-18.12-0.1020N_F-0.3497\beta_0$	-21.44
Υ		$6.47-0.923\beta_0$	$-13.6-0.102N_F-0.856\beta_0$	-21.7

scale ambiguity problem can be resolved if one can optimize the choice of scales and renormalization schemes according to some sensible criteria. In the BLM optimal scale setting,[4] the renormalization scales are chosen such that all vacuum polarization effects from the QCD β function are resummed into the running couplings.

In the present case one can show that within the V scheme (or the $\overline{MS}$ scheme) the BLM procedure does not change significantly the value of the NLO coefficient $r(\nu)$. This can be understood since the V scheme, as well as $\overline{MS}$ scheme, are adjusted primarily to the case when in the leading order there are dominant QED (Abelian) type contributions, whereas in the BFKL case there are important leading order gluon-gluon (non-Abelian) interactions. Thus one can choose for the BFKL case the MOM scheme[5] or the Υ scheme.

Adopting BLM scale setting, the NLO BFKL eigenvalue in the MOM scheme is

$$\omega^{\rm MOM}_{\rm BLM}(Q^2,\nu)=N_C\chi_L(\nu)\,\frac{\alpha_{\rm MOM}(Q^{\rm MOM\,2}_{\rm BLM})}{\pi}\left[1+r^{\rm MOM}_{\rm BLM}(\nu)\,\frac{\alpha_{\rm MOM}(Q^{\rm MOM\,2}_{\rm BLM})}{\pi}\right], \tag{10}$$

$$r^{\rm MOM}_{\rm BLM}(\nu)=r^{\rm conf}_{\rm MOM}(\nu)\,. \tag{11}$$

The β-dependent part of the $r_{\rm MOM}(\nu)$ defines the corresponding BLM optimal scale

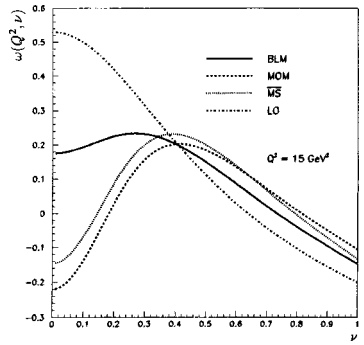

FIG. 1. ν dependence of the NLO BFKL eigenvalue: BLM (in the MOM scheme) — solid, MOM scheme (Yennie gauge: $\xi=3$) — dashed, $\overline{MS}$ scheme — dotted. LO BFKL ($\alpha_S=0.2$) — dot-and-dash.

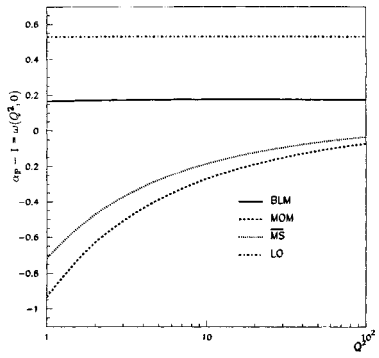

FIG. 2. Q^2 dependence of the BFKL Pomeron intercept in the NLO. The notation is as in Fig. 1.

$$Q^{2\,\mathrm{MOM}}_{\mathrm{BLM}}(\nu)=Q^2\exp\left[-\frac{4r^{\beta}_{\mathrm{MOM}}(\nu)}{\beta_0}\right]=Q^2\exp\left[\frac{1}{2}\chi_L(\nu)-\frac{5}{3}+2\left(1+\frac{2}{3}I\right)\right], \tag{12}$$

where $I=-2\int_0^1 dx\ln(x)/[x^2-x+1]\simeq 2.3439$. At $\nu=0$ we have $Q^{2\,\mathrm{MOM}}_{\mathrm{BLM}}(0)=Q^2(4\exp[2(1+2I/3)-5/3])\simeq Q^2\,127$.

Figures 1 and 2 and Table II give the results for the eigenvalue of the NLO BFKL kernel. We have used the QCD parameter $\Lambda=0.1\,\mathrm{GeV}$ which corresponds to $\alpha_S=4\pi/[\beta_0\ln(Q^2/\Lambda^2)]\simeq 0.2$ at $Q^2=15\,\mathrm{GeV}^2$.

One of the striking features of this analysis is that the NLO value for the intercept of the BFKL Pomeron, improved by the BLM procedure, has a very weak dependence on the gluon virtuality Q^2. The minor Q^2 dependence obtained leads to approximate scale and conformal invariance. Thus one may use conformal symmetry[6,10] for the continuation of the present results to the case $t\neq 0$.

Note that the application of fast apparent convergence[11] and the principle of minimal sensitivity[12] to the NLO BFKL eigenvalue problem lead to difficulties with the conformal weight dependence, an essential ingredient of BFKL calculations.[13]

It is worth noting also that since the BFKL equation can be interpreted as the ''quantization'' of a renormalization group equation[10] the effective scale should depend

TABLE II. The NLO BFKL Pomeron intercept in the BLM scale setting within non-Abelian physical schemes.

Scheme		$r_{\mathrm{BLM}}(0)$	$\alpha_{IP}^{\mathrm{BLM}}-1=\omega_{\mathrm{BLM}}(Q^2,0)$		
		$(N_F=4)$	$Q^2=1\ \mathrm{GeV}^2$	$Q^2=15\ \mathrm{GeV}^2$	$Q^2=100\ \mathrm{GeV}^2$
MOM	$\xi=0$	-13.05	0.134	0.155	0.157
	$\xi=1$	-12.28	0.152	0.167	0.166
	$\xi=3$	-11.74	0.165	0.175	0.173
Υ		-14.01	0.133	0.146	0.146

on the BFKL eigenvalue ω, associated with the Lorentz spin, rather than on ν. This issue and other recent approaches to the NLO BFKL[14] will be discussed in more detail in the extended version of this work.[13]

To conclude, we have shown that the NLO corrections to the BFKL equation for the QCD Pomeron become controllable and meaningful provided one uses physical renormalization scales and schemes relevant to non-Abelian gauge theory. BLM optimal scale setting sets the appropriate physical renormalization scale by absorbing the non-conformal β-dependent coefficients. The strong renormalization scale dependence of the NLO corrections to BFKL resummation then largely disappears. A striking feature of the NLO BFKL Pomeron intercept in the BLM approach is its very weak Q^2 dependence, which provides approximate conformal invariance.

VTK, LNL and GBP are thankful to A. R. White for warm hospitality at the Argonne National Laboratory. VTK and GBP thank Fermilab Theory Group for their kind hospitality. This work was supported in part by the Russian Foundation for Basic Research (RFBR): Grant 96-02-16717, 96-02-18897, 98-02-17885; INTAS: Grant 1867-93; INTAS-RFBR: Grant 95-0311; CRDF: Grant RP1-253; and the U. S. Department of Energy: Contract DE-AC03-76SF00515.

*)e-mail: gbpivo@ms2.inr.ac.ru

[1] V. S. Fadin, E. A. Kuraev, and L. N. Lipatov, Phys. Lett. B **60**, 50 (1975); L. N. Lipatov, Yad. Fiz. **23**, 642 (1976) [Sov. J. Nucl. Phys. **23**, 338 (1976)]; E. A. Kuraev, L. N. Lipatov, and V. S. Fadin, Zh. Éksp. Teor. Fiz. **71**, 840 (1976) [Sov. Phys. JETP **44**, 443 (1976)]; *ibid.* **72**, 377 (1977) [**45**, 199 (1977)]; Ya. Ya. Balitskiĭ and L. N. Lipatov, Yad. Fiz. **28**, 1597 (1978) [Sov. J. Nucl. Phys. **28**, 822 (1978)].
[2] V. S. Fadin and L. N. Lipatov, Phys. Lett. B **429**, 127 (1998).
[3] G. Camici and M. Ciafaloni, Phys. Lett. B **430**, 349 (1998).
[4] S. J. Brodsky, G. P. Lepage, and P. B. Mackenzie, Phys. Rev. D **28**, 228 (1983).
[5] W. Celmaster and R. J. Gonsalves, Phys. Rev. D **20**, 1420 (1979); Phys. Rev. Lett. **42**, 1435 (1979); P. Pascual and R. Tarrach, Nucl. Phys. **174**, 123 (1980); (E) B **181**, 546 (1981).
[6] L. N. Lipatov, Phys. Rep. **286**, 131 (1997).
[7] S. J. Brodsky and P. Huet, Phys. Lett. B **417**, 145 (1998).
[8] V. N. Gribov, L. N. Lipatov, and G. V. Frolov, Phys. Lett. B **31**, 34 (1970); Yad. Fiz. **12**, 994 (1970) [Sov. J. Nucl. Phys. **12**, 543 (1971)]; H. Cheng and T. T. Wu, Phys. Rev. D **1**, 2775 (1970).
[9] P. B. Mackenzie and G. P. Lepage, Phys. Rev. Lett. **47**, 1244 (1981).
[10] L. N. Lipatov, Zh. Éksp. Teor. Fiz. **90**, 1536 (1986) [Sov. Phys. JETP **63**, 904 (1986)]; R. Kirschner and L. Lipatov, Z. Phys. C **45**, 477 (1990).
[11] G. Grunberg, Phys. Lett. B **95**, 70 (1980); **114**, 271 (1982); Phys. Rev. D **29**, 2315 (1984).
[12] P. M. Stevenson, Phys. Lett. B **100**, 61 (1981); Phys. Rev. D **23**, 2916 (1981).
[13] S. J. Brodsky, V. S. Fadin, V. T. Kim *et al.*, in preparation.
[14] V. S. Fadin and L. N. Lipatov, *Proceedings of the Theory Institute on Deep Inelastic Diffraction*, ANL, Argonne, September 14–16, 1998; G. Salam, J. High Energy Phys. **9807**, 019 (1998); B. Andersson, G. Gustafson, and H. Kharraziha, Phys. Rev. D **57**, 5543 (1998); J. R. Forshaw, G. P. Salam, and R. S. Thorne, University of Manchester, MC-TH-98/23, 1998, http://xxx.lanl.gov/abs/hep-ph/9812304; M. Ciafaloni and D. Colferai, Phys. Lett. B **452** (1999).

Published in English in the original Russian journal. Edited by Steve Torstveit.

Improvement of perturbation theory in QCD for $e^+e^- \to$ hadrons and the problem of α_s freezing

B. V. Geshkenbein*) and B. L. Ioffe†)
Institute of Theoretical and Experimental Physics, 117218 Moscow, Russia

(Submitted 15 June 1999)
Pis'ma Zh. Éksp. Teor. Fiz. **70**, No. 3, 167–170 (10 August 1999)

A method of improving perturbation theory in QCD is developed which can be applied to any polarization operator. The case of the polarization operator $\Pi(q^2)$, corresponding to the process $e^+e^- \to$ hadrons, is considered in detail. By the use of the analytical properties of $\Pi(q^2)$ and a perturbation expansion of $\Pi(q^2)$ for $q^2<0$, the function $\mathrm{Im}\Pi(q^2)$ at $q^2>0$ is defined in such a way that the infrared pole is eliminated. The convergence of the perturbation series for $R(q^2)=\sigma(e^+e^- \to \text{hadrons})/(e^+e^- \to \mu^+\mu^-)$ is improved. After substitution of $R(q^2)$ into the dispersion relation an improved Adler function $D(q^2)$ is obtained, having no infrared pole and a frozen $\alpha_s(q^2)$. Good agreement with experiment is achieved. © *1999 American Institute of Physics.* [S0021-3640(99)00215-7]

PACS numbers: 12.38.Bx, 13.65.+i

It has been well known for years that perturbative calculations of amplitudes in field theories are legitimate if the virtualities k_i^2 of all external legs are negative, $k_i^2<0$. In this case the polarization operators and vertex functions (two- and three-point functions) are off mass shell and have no singularities. However, in order to get physical predictions, it is necessary to go to $k_i^2>0$ (at least for some of them). This can be achieved by analytical continuation using known analytical properties of the amplitudes. A typical example is e^+e^- annihilation into hadrons in QCD. The total cross section $\sigma(e^+e^- \to \text{hadrons})$ is proportional to the imaginary part of the polarization operator $\Pi_{\mu\nu}(q^2)$ of the virtual photon at $q^2>0$. At large enough $q^2<0$ the operator $\Pi_{\mu\nu}(q^2)$ can be calculated perturbatively in QCD in terms of an expansion in the running coupling constant $\alpha_s(q^2)=4\pi/\beta_0 \ln(-q^2/\Lambda^2)$. The tensor structure of $\Pi_{\mu\nu}(q)$ is

$$\Pi_{\mu\nu}(q)=(q_\mu q_\nu - q^2\delta_{\mu\nu})\Pi(q^2), \tag{1}$$

where $\Pi(q^2)$ is an analytic function of q^2 in the whole complex q^2 plane with a cut along the positive q^2 semiaxes. Analytical continuation from $q^2<0$ to $q^2>0$ results in the substitution $\ln(q^2/\Lambda^2) \to \ln(Q^2/\Lambda^2) - i\pi$, $Q^2=|q^2|$. Since small α_s corresponds to large $\ln(Q^2/\Lambda^2)$, the standard procedure (see, e.g., Ref. 1) is to consider $\ln(Q^2/\Lambda^2)$ as large compared with π and to perform the expansion in $\delta=\pi/\ln(Q^2/\Lambda^2)$. However, in practice it is not a good expansion parameter. At the typical scale of e^+e^- annihilation, $Q^2 \sim 10\,\mathrm{GeV}^2$ and $\Lambda \sim 300-400\,\mathrm{MeV}$, one has $\ln(Q^2/\Lambda^2) \approx 4-5$ and $\delta \approx 0.7$.

In this paper we present a systematic method of improving perturbation theory in QCD, which is free from this drawback. Besides e^+e^- annihilation, this method can be applied to any polarization operators, for example, to those used in the QCD sum rule approach. The idea of the method has been suggested by Radyushkin[2] and considered also by Pivovarov,[3] but many important features and consequences of this method were not touched upon in Refs. 2 and 3 (in particular, Eq. (10) below was not obtained and analyzed). Consider the Adler function

$$D(q^2)=-q^2\frac{d\Pi(q^2)}{dq^2}=-q^2\int_0^\infty\frac{R(s)ds}{(s-q^2)^2}, \tag{2}$$

where $R(s)=\sigma(e^+e^-\to\text{hadrons})/\sigma(e^+e^-\to\mu^+\mu^-)$. In the parton model $R(s)=R_p=3\Sigma_q e_q^2$, where e_q is the charge of the quark of flavor q. It is convenient to write:

$$D(q^2)=R_p(1+d(q^2)),\quad R(q^2)=R_p(1+r(q^2)),\quad \Pi(q^2)=R_p(1+p(q^2)). \tag{3}$$

Equation (3) implies the equation

$$d(q^2)=-q^2\frac{dp(q^2)}{dq^2}, \tag{4}$$

which has the solution

$$p(q^2)-p(\mu^2)=-\int_{\mu^2}^{q^2}\frac{ds}{s}d(s); \tag{5}$$

$r(q^2)$ is proportional to the discontinuity of $p(q^2)$ at $q^2>0$:

$$r(q^2)=\frac{1}{\pi}\operatorname{Im}p(q^2)=\frac{1}{2\pi i}[p(q^2+i\varepsilon)-p(q^2-i\varepsilon)]. \tag{6}$$

At negative $q^2<0$, $q^2=-Q^2$ the perturbation expansion of $d(Q^2)$ in the $\overline{MS}$ renormalization scheme is known up to the third order:[4,5]

$$d(Q^2)=a(1+d_1a+d_2a^2),\quad d_1=1.986-0.115N_f,$$
$$d_2=18.244-4.216N_f+0.086N_f^2, \tag{7}$$

where $a(Q^2)=\alpha_s(Q^2)/\pi$, N_f is the number of flavors and the small gluon–gluon scattering terms are omitted. With the same accuracy, the three-loop expression for $\alpha_s(Q^2)$ in $\overline{MS}$ is given by[6,7]

$$a(Q^2)=\frac{4}{\beta_0 L}\left\{1-\frac{2\beta_1}{\beta_0^2}\frac{\ln L}{L}+\frac{4\beta_1^2}{\beta_0^4L^2}\left[\left(\ln L-\frac{1}{2}\right)^2+\frac{\beta_2\beta_0}{8\beta_1^2}-\frac{5}{4}\right]\right\}, \tag{8}$$

where $L=\ln(Q^2/\Lambda^2)$ and

$$\beta_0=11-\frac{2}{3}N_f,\quad \beta_1=51-\frac{19}{3}N_f,\quad \beta_2=2857-\frac{5033}{9}N_f+\frac{325}{27}N_f^2. \tag{9}$$

Substitution of (7), (8) into (5) and (6) leads to perturbative corrections up to the third order in the physically measurable quantity $r(q^2)$. By taking the discontinuity, any dependence on the normalization point μ^2 is eliminated. It should be stressed that in such

a calculation no expansion in $\pi/\ln(Q^2/\Lambda^2)$ is performed — the only assumptions used (which are actually not assumptions but theorems), are the analytical properties of $\Pi(q^2)$. The result is $(q^2 \geqslant 0)$:

$$r(q^2)=\frac{4}{\pi\beta_0}\kappa-8\frac{\beta_1}{\beta_0^3}\frac{1}{\pi^2\tau^2}[\ln(\pi\tau)+1-\kappa t]+\left(\frac{4}{\beta_0}\right)^2\frac{d_1}{\pi^2}\frac{1}{1+t^2}$$
$$+16\frac{\beta_1^2}{\beta_0^5}\frac{1}{\pi^3\tau^4}\left\{\left(\frac{\beta_2\beta_0}{8\beta_1^2}-1\right)t+\kappa(1-t^2)\ln(\pi\tau)+t[\ln^2(\pi\tau)-\kappa^2]\right\}$$
$$-4d_1\left(\frac{4}{\beta_0^2}\right)^2\frac{\beta_1}{\pi^3\tau^4}\left\{t\left[\ln(\pi\tau)+\frac{1}{2}\right]+\frac{1}{2}\kappa(1-t^2)\right\}+d_2\left(\frac{4}{\beta_0}\right)^3\frac{t}{\pi^3\tau^4}, \qquad (10)$$

where

$$t=\frac{1}{\pi}\ln\frac{q^2}{\Lambda^2}, \quad \tau=(1+t^2)^{1/2}, \quad \kappa=\frac{\pi}{2}-\arctan t. \qquad (11)$$

The essential features of (10) are: 1) unlike the standard perturbation expansion, $r(q^2)$ has no infrared poles at $q^2=\Lambda^2$ and tends to a finite limit at $q^2\to 0$, viz., $r(0)=4/\beta_0 \approx 0.414$, corresponding to $\alpha_s(0)=4\pi/\beta_0\approx 1.3$, and all higher order terms vanish; 2) the convergence of the perturbation series in (10) is much better than for the standard ones: the ratio of the second-order term to the first-order term is smaller than 0.2 everywhere, and the ratio of the third-order to the second-order term is less than 0.1, while in the standard approach the ratio of the third-order term to the second-order term exceeds 0.5 below $q^2=10\,\mathrm{GeV}^2$ and is larger than 1 at $q^2\to 1\,\mathrm{GeV}^2$; 3) the α_s corrections given by (10) are remarkably smaller in the low-energy domain, $q^2\to 5\,\mathrm{GeV}^2$, than the standard ones, e.g., at $q^2=1\,\mathrm{GeV}^2$ one finds r (Eq. (10)) $/r_{\mathrm{stand}}=0.72$.

In order to get $r(q^2)$ at some lower values of q^2 by starting from the value of α_s at the Z-boson mass, $\alpha_s(m_z)$, which is now rather well known, it is necessary to use the renormalization group equations (8) and perform matching at the thresholds of new flavor production for b and c quarks and, if we would like to go to $q^2<1\,\mathrm{GeV}^2$, even at the s-quark threshold. This matching procedure introduces some uncertainty. The matching may be performed at $2m_q$ (or, what is practically equivalent, at m_Υ and $m_{J/\psi}$) or at m_q. The former seems to be preferable in the case of e^+e^- annihilation for obvious reasons. There are some arguments in favor of the latter choice, based on minimal sensitivity of the results to the matching-point value.[8] In the standard approach the results are rather sensitive to the choice of matching points – the ratio of r's in the two above mentioned cases is about 1.10–1.15 at $q^2\to 5\,\mathrm{GeV}^2$. We calculated the q^2 dependence of $r(q^2)$ starting from the point $q^2=m_z^2$ and going down. The value $r(m_z^2)$ was found from the requirement that $\alpha_s(m_z^2)$ determined in the standard way have the value $\alpha_s(m_z^2)=0.119\pm 0.002$ (Ref. 9). Then $\Lambda_5=230^{+27}_{-27}\,\mathrm{MeV}$ was found. In the evolution down to lower energies a matching of $r(q^2)$ at the masses of Υ, J/ψ, and φ was performed, resulting in $\Lambda_4=335^{+35}_{-33}\,\mathrm{MeV}$, $\Lambda_3=414^{+41}_{-37}\,\mathrm{MeV}$, and $\Lambda_2=490^{+51}_{-47}\,\mathrm{MeV}$. It was found, in particular, that $\pi r(1\,\mathrm{GeV}^2)=0.41$. If instead of matching at quarkonium masses a matching at m_q were done, the values of $r(q^2)$ would be only 4% smaller below $q^2=10\,\mathrm{GeV}^2$, practically independent of Q^2. Therefore this method has also some advan-

tages in this regard. The performed comparison with experiment demonstrated good agreement starting at $\sqrt{q^2}=0.7\,\mathrm{GeV}$, i.e., in a much broader interval than in a recent paper.[10]

After substituting $r(q^2)$ given by (10) into the dispersion relation (2) we get back the Adler function $D(q^2)$. The improved $D(q^2)_{\mathrm{impr}}$ obtained in this way has the correct analytical properties and no unphysical singularities. Therefore the procedure adopted here has an important advantage: the required analytical properties of the Adler function are restored. If $D(q^2)_{\mathrm{impr}}$ is represented in terms of an improved effective QCD coupling constant $\alpha_s(q^2)_{\mathrm{impr}}$, this would mean that $\alpha_s(q^2)_{\mathrm{impr}}$ has no infrared pole and is frozen at $q^2\to 0$. In this respect our approach has some resemblance to the approach of Shirkov and Solovtsov[11] (see also Ref. 12), where the condition of analyticity of $\alpha_s(q^2)$ in the cut complex q^2 plane was imposed. The difference is that we exploit the analyticity of the polarization operator $\Pi(q^2)$, which is a rigorous result in field theory, and do not use any hypothesis about analyticity of $\alpha_s(q^2)$.

The method of defining the improved QCD coupling constant $\alpha_s(q^2)_{\mathrm{impr}}$ in terms of $\underline{D(q^2)_{\mathrm{impr}}}$ looks very promising. For this goal, perhaps, the most suitable is to use not the $\overline{MS}$ but the Brodsky–Lepage–Mackenzie renormalization scheme,[13] where e^+e^- annihilation is considered as the basic process for the definition of $\alpha_s(q^2)$, with no higher-order α_s corrections. This problem requires further investigation.

The method presented above can be applied to the treatment of perturbative corrections to any polarization operators and may therefore lead to improvement of the QCD sum rule approach.

This work was supported in part REBR Grant 97-02-16131.

*)e-mail:geshken@vitep5.itep.ru
†)e-mail:ioffe@vitep5.itep.ru

[1] J. D. Bjorken, SLAC-PUB-5103 (1989).
[2] A. V. Radushkin, JINR preprint E2-82-159 (unpublished), JINR Rapid Communications, 4[78]-96, 9 (1996).
[3] A. A. Pivovarov, Nuovo Cimento A **105A**, 813 (1992).
[4] K. G. Chetyrkin, A. L. Kataev, and F. V. Tkachev, Nucl. Phys. B **174**, 345 (1980).
[5] A. L. Kataev and V. V. Starshenko, Mod. Phys. Lett. A **10**, 235 (1995).
[6] O. V. Tarasov, A. A. Vladimirov, and A. Yu. Zharkov, Phys. Lett. B **93**, 429 (1980).
[7] S. A. Larin and J. A. M. Vermaseren, Phys. Lett. B **303**, 304 (1993).
[8] W. Bernreuther, Ann. Phys. (Leipzig) **151**, 127 (1983).
[9] *Review of Particle Physics*, Eur. Phys. J. C **3**, 1 (1998).
[10] S. Eidelman, F. Jegerlehner, A. L. Kataev, and O. Veretin, preprint DESY-98-206, http://xxx.lanl.gov/abs/hep-ph/9812521.
[11] D. V. Shirkov and I. L. Solovtsov, Phys. Rev. Lett. **79**, 1204 (1997).
[12] E. Gardi, G. Grunberg, and M. Karliner, J. High Energy Phys. **9807**, 007 (1982).
[13] S. Brodsky, G. P. Lepage, and P. B. Mackenzie, Phys. Rev. D **28**, 228 (1983).

Published in English in the original Russian journal. Edited by Steve Torstveit.

On a possibility for observing the neutron electric polarizability

L. V. Mitsyna, A. B. Popov, and G. S. Samosvat
Frank Laboratory of Neutron Physics, JINR, 141980 Dubna, Moscow Region, Russia

(Submitted 23 June 1999)
Pis'ma Zh. Éksp. Teor. Fiz. **70**, No. 3, 171–174 (10 August 1999)

A new method is proposed for setting a lower or upper limit α_n^* on the neutron electric polarizability α_n. It is based on the fact that the real part of the *s*-wave scattering amplitude changes sign near the *s*-wave neutron resonance at $E=E^*$. The methods consist of the observation of the energy behavior of the forward–backward scattering asymmetry ω_1 which experiences a jump at $E=E^*$. If the jump is such that $d\omega_1/dE>0$, then $\alpha_n>\alpha_n^*$, while if $d\omega_1/dE<0$, then $\alpha_n<\alpha_n^*$, and if $d\omega_1/dE\sim 0$ then $\alpha_n\sim\alpha_n^*$. Seven even–even nuclei are found with α_n^* from 0.5 to 3.1 in 10^{-3} fm^3. Some details of a possible experiment with ^{182}W are described. © *1999 American Institute of Physics.* [S0021-3640(99)00315-1]

PACS numbers: 25.40.Fq, 14.20.Dh

1. All of the methods that have been used up to now to evaluate the neutron electric polarizability α_n consist of the extraction of a very small α_n effect against a large background caused by the strong nuclear interaction. As a result, all of them are essentially quantitative methods. The method we have found is, in essence, a qualitative one though it is also connected with the observation of a very small effect.

It is known[1–3] that the α_n effect can be observed in the neutron energy (E) dependence of the forward–backward asymmetry coefficient

$$\omega_1=\frac{\sigma(0)-\sigma(\pi)}{\sigma(0)+\sigma(\pi)}$$

($\sigma(\vartheta)$ is the differential scattering cross section) for neutron scattering by heavy nuclei at small E. The behavior of $\omega_1(E)$ is mostly determined by the interference between *s*- and *p*-waves and is illustrated in Fig. 1, where ω_1 is calculated for different α_n for the ^{238}U nucleus as if it had no neutron resonances. This picture is obtained using the approximate expressions

$$\sigma(\vartheta)=(f_0+f_1\cos\vartheta)^2, \tag{1}$$

$$\omega_1=2f_1/f_0, \tag{2}$$

where f_0 is the *s*-wave scattering amplitude and

$$f_1=f_1^{\mathrm{N}}+f_1^{\mathrm{pol}} \tag{3}$$

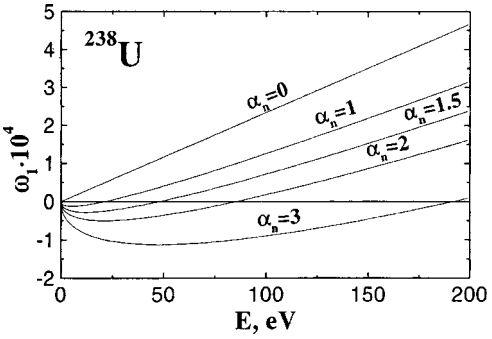

FIG. 1. The dependence of ω_1 on the neutron energy and for various α_n (in 10^{-3} fm^3) for ^{238}U nuclei when the resonances are not taken into account.

is the sum of the nuclear and polarizability contributions to the *p*-wave amplitude. For ^{238}U, they are

$$f_0 = -9.4 \text{ fm}, \qquad f_1^{\mathrm{N}} = -1.09\times 10^{-5} E \text{ fm}, \qquad f_1^{\mathrm{pol}} = 5.05\times 10^{-5}\alpha_n\sqrt{E} \text{ fm} \tag{4}$$

(here and below, E is in eV, α_n is in 10^{-3} fm^3) and $\omega_1(E)$ is as in Refs. 1 and 3. The main peculiarity in Fig. 1 is that each $\alpha_n > 0$ curve intersects the abscissa at a certain energy E'. This means that the *p*-wave amplitude f_1 changes sign from positive at $E < E'$ to negative at $E > E'$ provided only that f_0 is simply the positive *s*-wave scattering radius R_0' taken with a minus sign.

In spite of a large α_n contribution to ω_1 at eV energies it is hardly possible to obtain the corresponding curve $\omega_1(E)$ experimentally because this requires not only a measurement accuracy $\sim 10^{-5}$ but also an equal degree of removal of various distorting effects.

2. Instead of measuring the whole curve $\omega_1(E)$ we think it is possible to evaluate α_n by investigating ω_1 only near *s*-wave resonances, using a wonderful property of theirs. Such a resonance with energy E_0 for an even–even nucleus leads to the circumstance that the total *s*-wave amplitude f_0 (a potential of R_0' plus resonant) becomes zero at $E^* \cong E_0 - \Gamma_n/2kR_0'$ (k and Γ_n are the resonant values of the neutron wave number and neutron width) while $f_0 < 0$ at $E < E^*$ and $f_0 > 0$ at $E > E^*$. So, according to (2), ω_1 also changes sign at E^* from plus at $E < E^*$ to minus at $E > E^*$ if $f_1 < 0$. If $f_1 > 0$, the ω_1 situation is opposite. In turn, the sign of f_1, as we have already seen, depends on α_n and E, because f_1^{N} and f_1^{pol} in (3) have opposite signs and different E dependences. Thus the observation of any changes in the sign of ω_1 at a certain E^* from plus to minus or minus to plus gives at minimum an upper or lower limit of α_n, respectively.

3. All necessary calculations can be performed using instead of Eqs. (1)–(4) the following equations based on Ref. 4:

$$\sigma(\vartheta) = B_0 + B_1 \cos\vartheta, \qquad \omega_1 = B_1/B_0, \tag{5}$$

$$B_0 = \frac{1}{k^2}\left[\sin^2\delta_0 + 3\sin^2\delta_1 + \frac{1}{4}\,\frac{\Gamma_n^2}{\Delta E^2 + \Gamma^2/4} - \frac{\Gamma_n \sin\delta_0(\Delta E\cos\delta_0 + \Gamma\sin\delta_0/2)}{\Delta E^2 + \Gamma^2/4}\right], \tag{6}$$

$$B_1=\frac{1}{k^2}\left\{6\sin\delta_0\sin\delta_1\cos(\delta_0-\delta_1)\right.$$
$$\left.-\frac{3\Gamma_n\sin\delta_1[\Delta E\cos(2\delta_0-\delta_1)+\Gamma\sin(2\delta_0-\delta_1)/2]}{\Delta E^2+\Gamma^2/4}\right\}. \quad (7)$$

Here, the phase shifts are the sums of nuclear and polarizability terms:

$$\delta_0=-kR_0'+\frac{6}{5}k\frac{C}{R_q},\qquad \delta_1=-\frac{1}{3}(kR)^2kR_1'+\frac{\pi}{12}k^2C, \quad (8)$$

where R_0' and R_1' are the *s*- and *p*-wave scattering radii, $R=1.35\,\mathrm{A}^{1/3}$fm and $R_q=1.20\,\mathrm{A}^{1/3}$fm are the channel and charge radii, $C=M_n\alpha_n(Ze/\hbar)^2$ is a constant, M_n is the neutron mass, and Z is the charge number of the nucleus. Also Eqs. (6) and (7) contain the total width Γ of the resonance and $\Delta E=E-E_0$.

To choose a proper resonance which can give a suitably low limit for α_n, it is necessary to solve the equation $\delta_1=0$ at the energy E^* of this resonance. As a result, Eq. (8) gives

$$\alpha_n^*=14.7\frac{A^{2/3}R_1'\sqrt{E^*}}{Z^2},$$

where R_1' is in fm and E^* is in eV. It is just the value of α_n for which one must not see any peaks of ω_1 around E^*. A ω_1 jump will be observed there with $d\omega_1/dE<0$ if $\alpha_n<\alpha_n^*$ and with $d\omega_1/dE>0$ if $\alpha_n>\alpha_n^*$.

4. Unfortunately, the even–even nuclei ^{238}U and ^{232}Th have a lot of *p*-wave resonances, which make f_1 irregular and are therefore unsuitable for our purpose. We find only seven suitable nuclei whose first *s*-wave resonances do not give too high a value of α_n^* and have no known *p*-wave resonances at low energies. They are enumerated in Table 1 together with the necessary parameters. The approximate values of R_1' are obtained for six nuclei from Ref. 5 by interpolation and for ^{182}W from Refs. 6 and 7. The scattering cross section $\sigma_s=4\pi B_0$ and capture cross section σ_γ are given for $E=E^*$.

Two most informative nuclei have been chosen to illustrate (see Fig. 2) the proposed method of α_n observation. Doppler broadening is taken into account by the corresponding integration of (6) and (7) and of the cross sections σ_s and σ_γ in Table I.

5. Turning to the question of experiment, we should emphasize first that there is no need to try to obtain a ''clean'' picture of ω_1 like those in Fig. 2 when $\omega_1\to 0$ (or to a small value) on both sides of E^*. The presence of some secondary effects, such as scattering anisotropy in the laboratory system, different detectors at different angles, moderate backgrounds of various natures, etc., which cannot simulate a false jump in ω_1 at E^*, is quite permissible. This is the main advantage of our method.

At the same time, the implementation of the proposed method involves considerable difficulties. Principal among these are the necessity of having a large amount of a high-purity isotope for fabricating a scatterer and the necessity of accumulating very high statistics.

TABLE I.

Nucleus	R_0', fm	R_1', fm	E_0, eV	E^*, eV	α_n^*,10^{-3} fm^3	σ_s, b	σ_γ, b
$^{198}_{80}$Hg	10.3	4.5	23.00	22.69	1.7	1.2	300
$^{188}_{76}$Os	9.3	6.0	38.73	37.37	3.1	0.072	35
$^{182}_{74}$W	9.0	3.0	4.16	3.94	0.5	0.23	260
$^{178}_{72}$Hf	7.5	6.8	7.78	2.29	0.9	0.0004	16
$^{176}_{72}$Hf	7.5	6.8	7.93	6.34	1.5	0.0076	33
$^{170}_{70}$Yb	7.3	8.0	8.13	7.95	2.1	0.67	380
$^{162}_{66}$Dy	7.5	10.0	5.44	2.71	1.6	0.0058	72

The isotope ^{182}W seems to be the most promising tool for set the first experimental lower limit of α_n. The experiment can be carried out at Dubna on the 10-m flight path of the booster IREN, which is under construction, at a neutron intensity of $2.7 \times 10^5 E^{-0.9}\,\mathrm{cm}^{-2}\mathrm{s}^{-1}\mathrm{eV}^{-1}$ (E in eV). It is necessary to build a setup consisting of an aluminum vacuum tube about 4 m long and two identical detectors consisting of many ^{3}He counters. The neutron beam goes inside the tube and hits a scatterer whose plane is at an angle of 45° to the beam. One of the detectors is situated around the tube and counts neutrons scattered backwards. Another detector is set near the tube and counts neutrons scattered around $\vartheta = 90°$. In order to distinguish with confidence one type of singular ω_1 picture from another, it is sufficient to collect $\sim 5 \times 10^{10}$ counts in the area of a smaller ω_1 peak (negative if $\alpha_n < 0.5$, positive if $\alpha_n > 0.5$, or about zero if $\alpha_n \sim 0.5$) with a width of $\sim$0.18 eV. Using $\sim$1000 g of an isotope enriched to 99% as a scatterer in a beam 40 cm in diameter, one will have an average-over-peak neutron outlet probability of $\sim 7 \times 10^{-3}$. The necessary statistics can then be reached in $\sim$100 days if each detector has a solid angle of 10% of 4π and an efficiency of 40%.

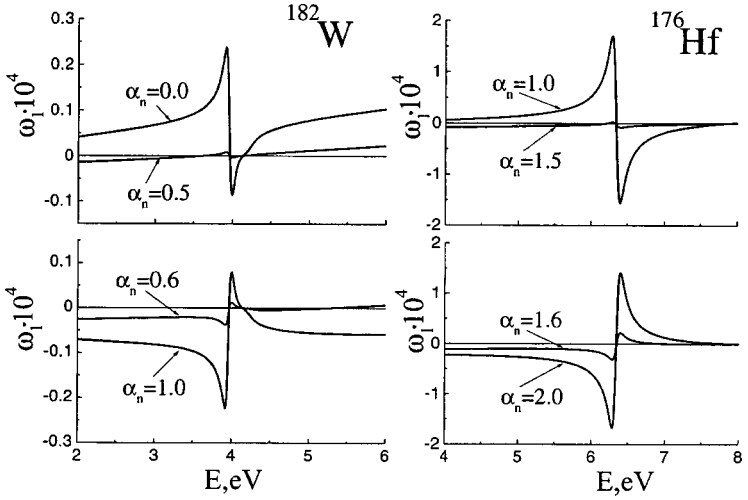

FIG. 2. The singular pictures near the 4.16 eV resonance of ^{182}W and the 7.93 eV resonance of ^{176}Hf for different α_n.

In conclusion, some additional difficulties that the experimentalist may face should be also mentioned. They are the background of delayed neutrons from the booster which are scattered by the target into the detectors, and the background of fast neutrons scattered into the room and re-scattered to the detectors. To avoid overloading the electronics it may be necessary to unlock the detectors only for the investigated interval of the time of flight.

This work has been made with the RFBR support, Grant 97-02-16213.

[1] R. M. Thaler, Phys. Rev. **114**, 827 (1959).
[2] Yu. A. Alexandrov, G. S. Samosvat, Zh. Sereeter, and Tsoj Gen Sor, JETP Lett. **4**, 134 (1966).
[3] G. S. Samosvat, J. Phys. (Paris), Colloq. **45**, Colloq. C3-51 (1984).
[4] J. M. Blatt and L. C. Biedenharn, Rev. Mod. Phys. **24**, 258 (1952).
[5] G. S. Samosvat, Fiz. Elem. Chastits At. Yadra **26**, 1567 (1995) [Phys. Part. Nuclei **26**, 655 (1995)].
[6] A. Langsdorf, Jr., R. O. Lane, and J. E. Monahan, Phys. Rev. **107**, 1077 (1957).
[7] L. V. Kuznetsova, A. B. Popov, and G. S. Samosvat, Preprint JINR R3-87-393 [in Russian], Joint Institute for Nuclear Research, Dubna (1987).

Published in English in the original Russian journal. Edited by Steve Torstveit.

A new escape channel for ultracold neutrons in traps

P. Geltenbort and V. V. Nesvizhevsky*)
Institute Laue-Langevin B. P 156, 38042, Grenoble Cedex 9, France

D. G. Kartashov, E. V. Lychagin, A. Yu. Muzychka,
G. V. Nekhaev, V. N. Shvetsov, and A. V. Strelkov
Joint Institute for Nuclear Research, 141980 Dubna, Moscow Region, Russia

A. G. Kharitonov, A. P. Serebrov, and R. R. Tal'daev
Petersburg Nuclear Physics Institute, 188350 Gatchina, Leningrad Region, Russia

J. M. Pendlebury
University of Sussex, Brighton BN1 9RH, UK

(Submitted 28 June 1999)
Pis'ma Zh. Éksp. Teor. Fiz. **70**, No. 3, 175–180 (10 August 1999)

A surprising new escape channel for ultracold neutrons (UCNs) in traps was reported recently. It could be relevant to the long-standing puzzle of the ''too high'' loss rate of UCNs from traps, which has yet to be completely understood and eliminated. In the present work we positively identify the new phenomenon and investigate it in detail. The escape of UCNs from traps is due to rare events in which their energy undergoes a small increase ($\sim 10^{-7}$ eV). The reason for such an energy gain and its impact on the physics of UCN storage is still to be investigated. © *1999 American Institute of Physics.*
[S0021-3640(99)00415-6]

PACS numbers: 28.20.Gd

Storage of ultracold neutrons (UCNs, $E \sim 10^{-7}$ eV, $V \sim 5$ m/s) in traps is a unique tool in fundamental physics experiments, particularly for precision measurement of the neutron lifetime. The total reflection of UCNs from trap walls allows their storage in closed traps. Thermal equilibrium is not achieved between such trapped neutrons and the walls: UCNs reflect elastically from trap surfaces up to $\sim 10^5$ times in succession, although the surface temperature is $\sim 10^5$ times higher than the temperature $\sim 10^{-3}$ K corresponding to the UCN kinetic energy. Inelastic upscattering of UCNs results in a neutron energy in the $\sim kT$ range.[1] UCNs could be also absorbed in a surface. However, these two known loss factors at trap walls are not sufficient to account for the too high loss rate of UCNs from traps. This is particularly evident in the so-called anomalous loss of UCNs on a beryllium surface: an additional temperature-independent loss with a probability of $\sim 10^{-5}$ per collision.[2] A general and detailed overview of UCN physics and the application of UCNs in fundamental physics, covering the time period until 1990–91, can be found in Refs. 3 and 4.

Unsuccessful attempts to achieve the theoretically predicted long storage times constrain the progress in experiments involving UCN storage. Also, the poor storage times indicate a complementary phenomenon that is not yet understood. Such inconsistency has

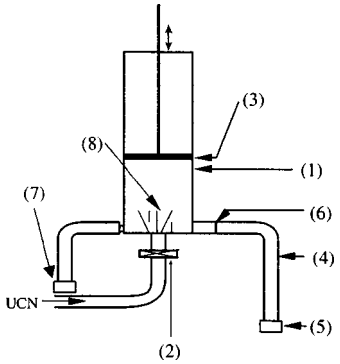

FIG. 1. Diagram of the setup: *1* — gravitational spectrometer, *2* — entrance shutter, *3* — polyethylene absorber, *4* — curved neutron guide, *5* — UCN detector, *6* — thin Al foil, *7* — monitor detector, *8* — samples.

stimulated searches for UCN upscattering to a different energy range than the standard thermal range.

UCN loss from traps as a result of surprising events involving a small increase in the energy of stored UCNs has been reported in several publications.[5–7] In the present work we positively identify such a process. The energy gain is due to an interaction of UCNs with the trap surface and is approximately equal to the initial UCN kinetic energy of $\sim 10^{-7}$ eV. In this article we investigate events involving a small increase or decrease in energy of UCNs in traps.

We used the method of UCN spectroscopy in the Earth's gravitational field. It is adequate in the investigated energy range of $\sim 10^{-7}$ eV, which corresponds to a jump height of ~ 1 m in the Earth's gravitational field. UCNs and ''slightly heated'' neutrons are stored simultaneously in one volume. A diagram of the setup is shown in Fig. 1. A more detailed account of the setup and the method of measurement is given in Refs. 5, 6, 8 and 9.

UCNs from a source via an entrance neutron guide fill the gravitational spectrometer (= storage volume) *1*. They are trapped in it when the entrance shutter *2* is closed. The gravitational spectrometer is a cylinder with a diameter of 60 cm and a height of 200 cm, pumped down to a residual pressure of $\sim 10^{-5}$ torr. It is made of polished stainless steel. The critical energy is $\sim$190 neV ($mg \cdot 1\ \mathrm{cm} \approx 1$ neV). Inside the spectrometer a polyethylene absorbing disk *3* is installed. It moves up or down along the total spectrometer height. UCNs with energy $E > mgh_{\mathrm{absor}}$ (where m is the neutron mass, g is the acceleration in the Earth's gravitation field, and h_{absor} is the absorber height above the bottom of the spectrometer) can penetrate in the absorber. The absorber has no reflecting potential and it has high upscattering cross section. Such properties provide perfect absorbing efficiency. The kinetic energy of a neutron that has been upscattered in the polyethylene is in the $\sim kT$ range. Such a neutron is not trapped. It leaves the spectrometer. Thus, after UCNs have filled the spectrometer and have been stored in it for some time (with the entrance valve closed), the spectrum is shaped so that there are no neutrons in it with energy $E > mgh_{\mathrm{absor}}$. A ^{3}He gaseous UCN detector *5* with a thin Al entrance window is installed ~ 1 m lower than the bottom of the spectrometer. It is connected to the spectrometer via a curved neutron guide *4*. The curvature of the neutron guide allows protec-

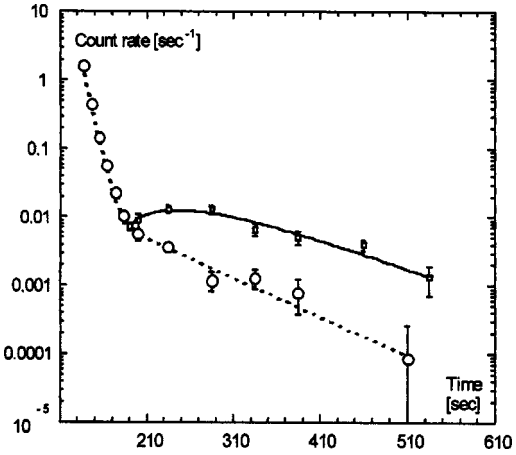

FIG. 2. Time dependence of the count rate of neutrons penetrating through the Al foil in the stainless-steel spectrometer. The lower curve corresponds to a fixed-height absorber. The upper curve corresponds to an absorber that is raised up 80 s after the entrance shutter is closed. The background has been subtracted.

tion of the detector against thermal neutrons produced in/on the separating foil *6* and spectrometer surfaces. Besides, this neutron guide provides an increase in the efficiency of UCN detection due to their acceleration in the Earth's gravitational field. Such increase in the UCN velocity allows their easier penetration through the potential barrier of the detector's Al window. The curved neutron guide and the detector are separated from the storage volume by a vacuum-tight 10.5-μm-thick Al foil *6*. The UCN flux in the spectrometer is measured with a monitor detector *7*, which is analogous to the main detector *5*. It is separated from the storage volume by a thick foil with a small ($\sim 1\ \mathrm{cm}^2$) hole. Samples *8* with a large surface area can be placed on the bottom of the spectrometer.

Separation of the storage volume from the detector by a vacuum-tight Al foil with a critical energy $E_{\mathrm{Al}} \sim 52$ neV allows detection of UCNs with energy $E > 52$ neV only. During filling the absorber is at a lower height $h_{\mathrm{absor}} < E_{\mathrm{Al}}/mg$ (in the present measurement $h_{\mathrm{absor}} = 46$ cm). The count rate is expected to fall rather rapidly to the background level after closure of the entrance shutter. The characteristic time for this decrease corresponds to the cleaning time for UCNs with energy $E > mgh_{\mathrm{absor}}$. In fact, after this fast dropoff of the count rate with the expected characteristic time there is still some count rate significantly above the background. This count rate decreases in time in parallel (with the same characteristic time) with the UCN density in the spectrometer (Fig. 2, lower curve). After raising the absorber (for $\sim$12 s, starting 80 s after closure of the entrance shutter) the count rate increases by $\sim$25 times (Fig. 2, upper curve). We believe that the only reasonable interpretation for such data is a small gain in energy of the stored UCNs that allows them to overcome the potential barrier of the Al separating foil. Neutrons with energy $E_{\mathrm{Al}} < E < mgh_{\mathrm{absor}}$ are not absorbed (when the absorber is raised) and they are detected more efficiently than with the absorber down.

The generation of these slightly heated UCNs in traps is similar to a vaporizing process. We therefore call them VUCNs. Raising the absorber to different heights allows measurement of the VUCN spectrum (Fig. 4).

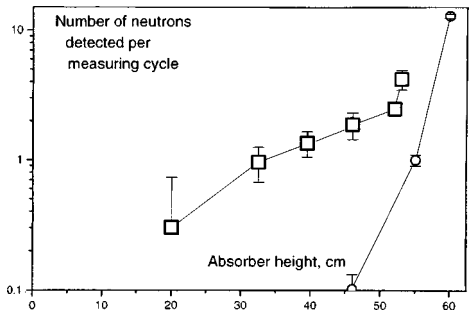

FIG. 3. ''Integral'' spectrum of cooled-down neutrons in the stainless-steel spectrometer. The squares correspond to the number of cooled-down neutrons versus the absorber height during the spectrum cleaning (the absorber height during filling is 160 cm). The circles correspond to a fixed-height absorber (''background'' measurement).

For studies of this process at different surfaces the corresponding samples were placed inside the spectrometer, and the additional rate of generation of VUCNs was measured. For many samples it was relatively low compared to the generation rate at the spectrometer walls. We therefore later replaced the stainless-steel spectrometer by a copper cylindrical spectrometer with a diameter of 20 cm and a height of 180 cm.

Reverse (as compared to an increase in energy of the UCNs) events involving a decrease in energy were measured in the stainless-steel spectrometer. A 10.5-μm-thick Al foil was installed just above the entrance shutter. At the spectrometer exit a shutter replaced the thin separating foil that had been used in the measurement of an increase in energy. After UCNs have filled the spectrometer (with the exit shutter closed) the entrance shutter is closed also. The UCN spectrum in the spectrometer is shaped so that there are no neutrons with energy $E<E_{\mathrm{Al}}$ or $E>mgh_{\mathrm{absor.up.}}$. If, after some time period, the absorber is moved down to a height lower than E_{Al}/mg (in the present measurement $h_{\mathrm{absor}}=46$ cm), then it absorbs all the UCNs in the spectrometer. If some of the UCNs are downscattered to an energy $E/mg<46$ cm, then those neutrons survive because they never hit the absorber. Later they are counted when the exit shutter is open (Fig. 3). Variation of the maximal absorber height (during filling and storage) and the minimal absorber height (during cleaning) permits estimation of the energies from/to which the UCNs are downscattered.

The generation rate for both measured processes (increase and decrease in energy of UCNs) is proportional to the surface area. This indicates that it is collisions of UCNs with the surface that are responsible for the phenomenon of small energy changes.

The average probability of UCN heating to VUCN range equals the ratio of the VUCN generation rate to the UCN surface collision rate. The storage times for UCNs and VUCNs in the spectrometer, the collision frequency, and the detection efficiency for VUCNs depend on energy. Therefore the estimation of the average heating probability should be based on a precise knowledge of the initial spectrum, its evolution, the VUCN spectrum, and the spectral dependence of the VUCN detection efficiency. A significant disadvantage of the present setup is its complete insensitivity to VUCNs with energies in the approximate range $E<E_{\mathrm{Al}}+15$ neV. Such slightly above-barrier neutrons do not penetrate the foil efficiently because of the high probability of back reflection and losses

TABLE I.

Sample	$\mu \cdot 10^{-4}$	$P_+ \cdot 10^{-7}$	$P_- \cdot 10^{-7}$
Surface of stainless-steel spectrometer	18.3 ± 0.2	$>5.5 \pm 0.4$	1.0 ± 0.1
Surface of copper spectrometer	12.7 ± 0.5	$>0.68 \pm 0.13$	
Sample of stainless steel	6.2 ± 1.4	$>3.1 \pm 0.6$	
Degassed sample of stainless steel	0.1 ± 0.9	$>1.4 \pm 0.3$	
Sample of beryllium	~ 5.0	$>1.0 \pm 0.25$	
Degassed sample of beryllium	<1	$>1.0 \pm 0.25$	

In the columns: 1st) The sample material. 2nd) The loss probability under the assumption of a 46 neV UCN monoline spectrum and for the experimentally measured storage times. 3rd) Lower bound on the probability P_+ of an increase in energy, calculated using the model described above. 4th) The probability P_- of a decrease in energy. The actual values of the probability of an increase in energy are significantly higher than the minimum estimates presented here.

in the foil. On the other hand the present setup and methods in principal allow direct measurement of just such changes in energy that cause UCN losses in standard storage experiments. Also the probability estimate depends on whether one uses a model of one-step or many-step changes in energy.

We therefore present only lower bounds on the heating probabilities and leave more accurate estimations for the future. We assumed here a one-step process, monolines with energies 46 neV and 110 neV, respectively, for the UCN and VUCN spectra, and equality of storage times for UCNs and VUCNs. Each of these assumptions corresponds to the most conservative, lowest estimate for the heating probability.

The estimate for the probability of a small decrease in UCN energy is almost model-independent.

The estimates are listed in Table I. The stainless-steel sample was degassed at $\sim$1100 K for $\sim$30 min. Such heating of the sample decreased the magnetic permeability by $\sim 10^3$ times, but the VUCN generation did not change significantly. This means that VUCN generation has no direct relation to the ferromagnetic properties of the sample.

Investigation of the VUCN spectrum in the stainless-steel spectrometer shows that it is shaped from above at the energy $\sim$110 neV, while the initial spectrum was shaped at $\sim$46 neV (Fig. 4). It should be underscored once again that the setup is insensitive to VUCNs with energies in the approximate range $E < E_{\mathrm{Al}} + 15$ neV. Therefore Fig. 4 could be used only for qualitative estimation of the VUCN spectrum.

In Fig. 3 the number of cooled-down neutrons is shown versus the minimal absorber height. This corresponds to the integral spectrum of cooled-down neutrons.

We have verified and positively identified the new phenomenon[5,6] of a small energy heating of UCNs at trap surfaces, which causes additional losses of UCNs from traps. The nature of these energy changes is not quite clear yet.

At a stainless-steel surface the kinetic energy for some UCNs increases at most by about a factor of two. The probability of such an energy gain is higher than $\sim 10^{-6}$ per collision. It does not depend strongly on the loss coefficient and magnetic permeability of the material. This seems to contradict the idea of quasi-elastic scattering of UCNs on

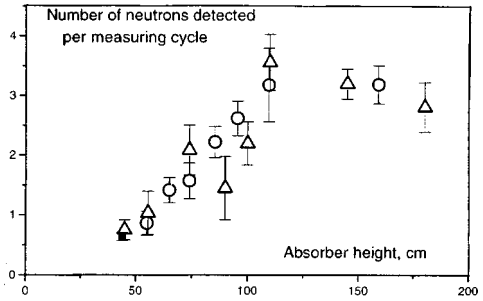

FIG. 4. ''Integral'' VUCN spectrum. The circles correspond to VUCN generation at the stainless-steel spectrometer walls. The triangles correspond to VUCN generation at a stainless-steel sample in the copper spectrometer. The square is for a fixed-height absorber in the stainless-steel spectrometer.

surface hydrogen impurities is also at odds with a linking of the process to the ferromagnetic properties of the wall materials. The measured absolute probabilities and their qualitative behavior (their independence of the standard inelastic scattering probability) contradict the results presented in Ref. 7. However, the different energy spectra measured in these experiments do not allow a clear comparison. We have also identified for the first time a small energy increase for UCNs at copper and beryllium surfaces. This indicates that the phenomenon is of a universal nature.

We have also measured events involving a small decrease in energy of UCNs at stainless-steel surfaces. This phenomenon was earlier reported in Ref. 10. It probably has a common physical cause with the small heating of UCNs. The probability of such a decrease in energy is at least 10 times lower than that for an increase in energy.

In the future we intend to measure directly the impact of the small energy heating on UCN storage times and particularly on the additional ''unavoidable'' anomalous UCN losses. The temperature dependence of such a process is of significant interest because it could clarify the nature of this effect.

*)e-mail: nesvizhevsky@ill.fr

[1] A. D. Stoica, A. V. Strelkov, and M. Hetzelt, Z. Phys. B **29**, 349 (1978).
[2] V. P. Alfimenkov, V. V. Nesvizhevsky, A. P. Serebrov *et al.*, JETP Lett. **55**, 84 (1992).
[3] V. K. Ignatovich, in *The physics of ultracold neutrons* (Clarendon Press, Oxford, 1990).
[4] R. Golub, D. Richardson and S. K. Lamoreaux, in *Ultracold Neutrons* (Adam Hilger, Bristol, 1991).
[5] V. V. Nesvizhevsky, A. V. Strelkov, P. Geltenbort, and P. S. Yaidjiev, ILL, Annual Report (1997), p. 62, also accepted for publication in EPJ Applied Physics.
[6] V. V. Nesvizhevsky, A. V. Strelkov, P. Geltenbort, and P. S. Yaidjiev, JINR Preprint R3-98-79 (1998) [in Russian]; Yad. Fiz. **62**, 832 (1999).
[7] S. Arzumanov, L. Bondarenko, S. Chernyavsky *et al.*, in *Proceedings of the International Seminar on Interaction of Neutrons with Nuclei ISINN-6*, JINR, Dubna, Russia, 13–16 May, 1998, p. 108.
[8] A. V. Strelkov, V. V. Nesvizhevsky *et al.*, in *Particle Physics with Slow Neutrons*, 22–24 October, 1998 (publ. in Nucl. Instrum. Methods).
[9] P. Geltenbort, A. G. Kharitonov, V. V. Nesvizhevsky *et al.*, ILL Preprint ILL97GE5051 (1997).
[10] L. Bondarenko, V. Morozov, E. Korobkina *et al.*, *Proceedings of the International Seminar on Interaction of Neutrons with Nuclei ISINN–6* JINR, Dubna, Russia, 13–16 May, 1998, p. 101.

Published in English in the original Russian journal. Edited by Steve Torstveit.

Transverse spectra of radiation processes in a medium

B. G. Zakharov
Institut für Kernphysik, Forschungszentrum Jülich D-52425 Jülich, Germany;
L. D. Landau Institute of Theoretical Physics, Russian Academy of Sciences, 117334 Moscow, Russia

(Submitted 1 July 1999)
Pis'ma Zh. Éksp. Teor. Fiz. **70**, No. 3, 181–186 (10 August 1999)

A formalism is developed for evaluation of the transverse momentum dependence of the cross sections of radiation processes in a medium. The analysis is based on the light-cone path integral approach to the induced radiation. The results are applicable in both QED and QCD.
 [S0021-3640(99)00515-0]

PACS numbers: 11.80.La, 12.20.Ds, 12.38.−t

It is well known that at high energies, multiple scattering can considerably modify the cross sections of radiation processes in a medium.[1,2] Recently this effect (called the Landau–Pomeranchuk–Migdal (LPM) effect) in QED and QCD has attracted much attention[3–10] (see also Ref. 11 and references therein). In Ref. 6 we developed a rigorous new light-cone path integral approach to the LPM effect. There we have discussed the p_T-integrated spectra. For many problems it is highly desirable also to have a formalism for the p_T dependence of the radiation rate. In the present paper we derive the corresponding formulas. Like those of Ref. 6, our results are applicable in both QED and QCD.

For simplicity we describe the formalism for an induced $a\to bc$ transition in QED for scalar particles with an interaction Lagrangian $L_{\rm int}=\lambda[\hat{\psi}_b^+\hat{\psi}_c^+\hat{\psi}_a+\hat{\psi}_a^+\hat{\psi}_c\hat{\psi}_b]$ (it is assumed that $m_a<m_b+m_c$ and that the decay $a\to bc$ is absent in vacuum). The S-matrix element for the $a\to bc$ transition in an external potential reads

$$\langle bc|\hat{S}|a\rangle = i\int dtd\mathbf{r}\lambda\,\psi_b^*(t,\mathbf{r})\psi_c^*(t,\mathbf{r})\psi_a(t,\mathbf{r}), \tag{1}$$

where ψ_i are the wave functions (incoming for $i=a$ and outgoing for $i=b,c$). We write ψ_i as

$$\psi_i(t,\mathbf{r}) = \frac{1}{\sqrt{2E_i}}\exp[-i(t-z)p_{i,z}]\phi_i(t,\mathbf{r})\,. \tag{2}$$

We consider the case when the particle a approaches the target from infinity, and normalize the flux to unity (it corresponds to $|\phi_i|=1$) at $z=-\infty$ for $i=a$ and at $z=\infty$ for $i=b,c$. The case when the particle a is produced in a hard reaction in a medium (or at a

FIG. 1. The diagram representation of the inclusive spectrum (5) (a), and (7) (b).

finite distance from a medium) will be discussed later. At high energy, $E_i \gg m_i$, the dependence of ϕ_i on the variable $\tau=(t+z)/2$ at $t-z=\text{const}$ is governed by the two-dimensional Schrödinger equation

$$i\frac{\partial \phi_i}{\partial \tau}=H_i\phi_i\,, \tag{3}$$

$$H_i=-\frac{1}{2\mu_i}\left(\frac{\partial}{\partial \boldsymbol{\rho}}\right)^2+e_iU+\frac{m_i^2}{2\mu_i}, \tag{4}$$

where $\mu_i=p_{i,z}$, $\boldsymbol{\rho}$ is the transverse coordinate, e_i is the electric charge, and U is the potential of the target.

In the high-energy limit one can obtain from (1), (2) the inclusive cross section

$$\frac{d^5\sigma}{dx\,d\mathbf{q}_b\,d\mathbf{q}_c}=\frac{2}{(2\pi)^4}\,\mathrm{Re}\int d\boldsymbol{\rho}_1 d\boldsymbol{\rho}_2\int_{z_1<z_2} dz_1 dz_2\, g\langle F(z_1,\boldsymbol{\rho}_1)F^*(z_2,\boldsymbol{\rho}_2)\rangle\,, \tag{5}$$

where $F(z,\boldsymbol{\rho})=\phi_b^*(t,\mathbf{r})\phi_c^*(t,\mathbf{r})\phi_a(t,\mathbf{r})|_{t=z}$, $\mathbf{q}_{b,c}$ are the transverse momenta, $x=p_{b,z}/p_{a,z}$ (note that for the particle c $p_{c,z}=(1-x)p_{a,z}$), $g=\lambda^2/[16\pi x(1-x)E_a^2]$, and $\langle\ldots\rangle$ means averaging over the states of the target. Since the wave functions enter (5) only at $t=z$, ϕ_i can be regarded as functions of z and $\boldsymbol{\rho}$. In the Schrödinger equation (3) z will play the role of time. We represent the z dependence of ϕ_i in terms of the Green's function K_i of the Hamiltonian (4). Then, diagrammatically, (5) is described by the graph of Fig. 1a. We depict K_i (K_i^*) by $\rightarrow$ ($\leftarrow$). The dotted line shows the transverse density matrices at large longitudinal distances in front of ($z=z_i$) and behind ($z=z_f$) the target[1)]. We will consider first the $\mathbf{q}_c$-integrated spectrum. For the sake of generality we assume that all the particles are charged in this case. Later we will give the formula for the totally inclusive spectrum when at least one of the final particles has zero charge. For the $\mathbf{q}_c$-integrated case the transverse density matrix for the final particle c is given by a δ function, and by making use of the relation

$$\int d\boldsymbol{\rho}_2 K(\boldsymbol{\rho}_2,z_2|\boldsymbol{\rho}_1,z_1)K^*(\boldsymbol{\rho}_2,z_2|\boldsymbol{\rho}_1',z_1)=\delta(\boldsymbol{\rho}_1-\boldsymbol{\rho}_1') \tag{6}$$

one can transform the graph of Fig. 1a into that of Fig. 1b. The corresponding analytical expression reads

$$\frac{d^3\sigma}{dxd\mathbf{q}_b}=\frac{2}{(2\pi)^2}\,\mathrm{Re}\int d\boldsymbol{\rho}_{b,f}d\boldsymbol{\rho}'_{b,f}d\boldsymbol{\rho}_b d\boldsymbol{\rho}'_b d\boldsymbol{\rho}_a d\boldsymbol{\rho}'_a d\boldsymbol{\rho}_{a,i}d\boldsymbol{\rho}'_{a,i}\,\exp[-i\mathbf{q}_b\cdot(\boldsymbol{\rho}_{b,f}-\boldsymbol{\rho}'_{b,f})]$$
$$\times\int_{z_i}^{z_f}dz_1\int_{z_1}^{z_f}dz_2\,gS_b(\boldsymbol{\rho}_{b,f},\boldsymbol{\rho}'_{b,f},z_f|\boldsymbol{\rho}_b,\boldsymbol{\rho}'_b,z_2)M(\boldsymbol{\rho}_b,\boldsymbol{\rho}'_b,z_2|\boldsymbol{\rho}_a,\boldsymbol{\rho}'_a,z_1)$$
$$\times S_a(\boldsymbol{\rho}_a,\boldsymbol{\rho}'_a,z_2|\boldsymbol{\rho}_{a,i},\boldsymbol{\rho}'_{a,i},z_i), \tag{7}$$

where

$$S_i(\boldsymbol{\rho}_2,\boldsymbol{\rho}'_2,z_2|\boldsymbol{\rho}_1,\boldsymbol{\rho}'_1,z_1)=\langle K_i(\boldsymbol{\rho}_2,z_2|\boldsymbol{\rho}_1,z_1)K_i^*(\boldsymbol{\rho}'_2,z_2|\boldsymbol{\rho}'_1,z_1)\rangle \tag{8}$$

is the evolution operator for the transverse density matrix, and the factor M is given by

$$M(\boldsymbol{\rho}_2,\boldsymbol{\rho}'_2,z_2|\boldsymbol{\rho}_1,\boldsymbol{\rho}'_1,z_1)=\langle K_b(\boldsymbol{\rho}_2,z_2|\boldsymbol{\rho}_1,z_1)K_c(\boldsymbol{\rho}'_2,z_2|\boldsymbol{\rho}_1,z_1)K_a^*(\boldsymbol{\rho}'_2,z_2|\boldsymbol{\rho}'_1,z_1)\rangle\,. \tag{9}$$

We assume that the target density does not depend on $\boldsymbol{\rho}$. Then a considerable part of the calculations can be done analytically. In (8), (9) we represent the Green's functions in the path integral form. In the corresponding path integral formulas for S_i and M the interaction of the particles with the target potential after averaging over the target states turns out to be transformed into the interaction between trajectories described by the Glauber absorption factors. For S_i the corresponding absorption cross section is given by the dipole cross section $\sigma_{i\bar{i}}$ for interaction with the medium constituent of the $i\bar{i}$ pair. The absorption factor for M involves the three-body cross section σ_{abc}, which depends on the relative transverse vectors $\boldsymbol{\tau}_{bc}=\boldsymbol{\rho}_b-\boldsymbol{\rho}_c$ and $\boldsymbol{\tau}_{ab}=\boldsymbol{\rho}_a-\boldsymbol{\rho}_b$. The factor S_i can be evaluated analytically. The corresponding formulas are given in Refs. 12 and 6. The factor M after the analytical path integration over the center-of-mass coordinates can be expressed in terms of the Green's function K_{bc} describing the relative motion of the particles b and c in a fictitious $\bar{a}bc$ system. The formula for M can be obtained from that given in Ref. 6 by replacing the final transverse coordinate $\boldsymbol{\rho}_2$ by $\boldsymbol{\rho}'_2$ for the particle c. The expression for the probability of the $a\to bc$ transition at a given impact parameter, which we obtain by integrating analytically over all the transverse coordinates (except for $\boldsymbol{\tau}_b=\boldsymbol{\rho}_{b,f}-\boldsymbol{\rho}'_{b,f}$) in (7), has the form

$$\frac{d^3P}{dxd\mathbf{q}_b}=\frac{2}{(2\pi)^2}\mathrm{Re}\int d\boldsymbol{\tau}_b\exp(-i\mathbf{q}_b\cdot\boldsymbol{\tau}_b)$$
$$\times\int_{z_i}^{z_f}dz_1\int_{z_1}^{z_f}dz_2\,g\Phi_b(\boldsymbol{\tau}_b,z_2)K_{bc}(\boldsymbol{\tau}_b,z_2|0,z_1)\Phi_a(\boldsymbol{\tau}_a,z_1), \tag{10}$$

where

$$\Phi_a(\boldsymbol{\tau}_a,z_1)=\exp\left[-\frac{\sigma_{a\bar{a}}(\boldsymbol{\tau}_a)}{2}\int_{z_i}^{z_1}dzn(z)\right],$$
$$\Phi_b(\boldsymbol{\tau}_b,z_2)=\exp\left[-\frac{\sigma_{b\bar{b}}(\boldsymbol{\tau}_b)}{2}\int_{z_2}^{z_f}dzn(z)\right] \tag{11}$$

are the eikonal initial- and final-state absorption factors,[2)] and $\boldsymbol{\tau}_a=x\boldsymbol{\tau}_b$. The Hamiltonian for the Green's function K_{bc} reads

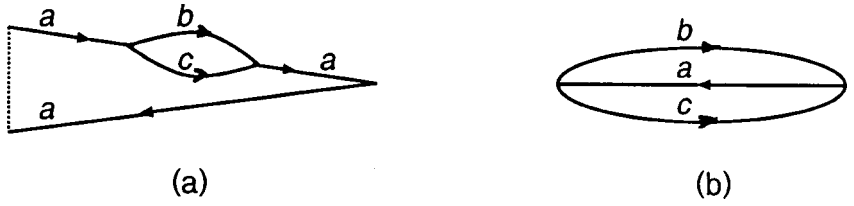

FIG. 2. The diagram representation of the radiative correction to the probability of $a\to a$ transition.

$$H_{bc}=-\frac{1}{2\mu_{bc}}\left(\frac{\partial}{\partial\boldsymbol{\tau}_{bc}}\right)^2-\frac{in(z)\sigma^{-}_{abc}(\boldsymbol{\tau}_{bc},\boldsymbol{\tau}_{ab})}{2}-\frac{i}{L_f}, \tag{12}$$

where $\mu_{bc}=E_a x(1-x)$, $\boldsymbol{\tau}_{ab}=-[\boldsymbol{\tau}_a+(1-x)\boldsymbol{\tau}_{bc}]$, and $L_f=2E_a x(1-x)/[m_b^2(1-x)+m_c^2 x-m_a^2 x(1-x)]$ is the so-called formation length. In (11), (12) $n(z)$ is the number density of the target. If the target occupies the region $0<z<L$ one can drop in (10) the contribution from the configurations with $z_{1,2}<0$ and $z_{1,2}>L$. This follows from the relation for the Green's function K^0_{bc} for the Hamiltonian (12) in vacuum:

$$\mathrm{Re}\int_0^\infty dz K^0_{bc}(\boldsymbol{\tau},z|0,0)=\mathrm{Re}\int_0^\infty dz\left(\frac{\mu_{bc}}{2\pi iz}\right)\exp\left\{i\left[\frac{\mu_{bc}\boldsymbol{\tau}^2}{2z}-\frac{z}{L_f}\right]\right\}=0\,. \tag{13}$$

This allows one to rewrite (10) in another form:

$$\begin{aligned}\frac{d^3P}{dxd\mathbf{q}_b}=\frac{2}{(2\pi)^2}\mathrm{Re}\int d\boldsymbol{\tau}_b\exp(-i\mathbf{q}_b\cdot\boldsymbol{\tau}_b)\int_{z_i}^{z_f}dz_1\int_{z_1}^{z_f}dz_2\, g\{&\Phi_b(\boldsymbol{\tau}_b,z_2)\\ &\times[K_{bc}(\boldsymbol{\tau}_b,z_2|0,z_1)-K^0_{bc}(\boldsymbol{\tau}_b,z_2|0,z_1)]\Phi_a(\boldsymbol{\tau}_a,z_1)\\ &+[\Phi_b(\boldsymbol{\tau}_b,z_2)-1]K^0_{bc}(\boldsymbol{\tau}_b,z_2|0,z_1)[\Phi_a(\boldsymbol{\tau}_a,z_1)-1]\},\end{aligned} \tag{14}$$

which demonstrates explicitly that the configurations with $z_{1,2}<0$ and $z_{1,2}>L$ do not contribute to the radiation rate. Equations (10), (14) establish the theoretical basis for evaluation of the transverse momentum dependence of the LPM effect.

The integration over $\mathbf{q}_b$ in (14) gives the x spectrum

$$\frac{dP}{dx}=2\mathrm{Re}\int_{z_i}^{z_f}dz_1\int_{z_1}^{z_f}dz_2\, g[K_{bc}(0,z_2|0,z_1)-K^0_{bc}(0,z_2|0,z_1)], \tag{15}$$

which we obtained earlier in Ref. 6. There it has been derived using the unitarity connection between the probability of the $a\to bc$ transition and the radiative correction to the $a\to a$ transition. The latter is described by the diagram of Fig. 2a, which in turn, using (6), can be transformed into the graph of Fig. 2b.[3)] It can also be obtained directly from the graph of Fig. 1b after integrating over $\mathbf{q}_b$.

In the low-density limit Eq. (14) can be written in terms of the light-cone wave function Ψ_a^{bc}:

$$\frac{d^3P}{dxd\mathbf{q}_b}=\frac{1}{(2\pi)^2}\int d\boldsymbol{\rho}d\boldsymbol{\rho}'\ \exp(-i\mathbf{q}_b\cdot\boldsymbol{\rho}')\Psi_a^{bc*}$$
$$\times(x,\boldsymbol{\rho}-\boldsymbol{\rho}')T\sigma_{\bar{a}bc}(\boldsymbol{\rho}_{bc},\boldsymbol{\rho}_{ab})\Psi_a^{bc}(x,\boldsymbol{\rho}), \tag{16}$$

where $\boldsymbol{\rho}_{bc}=\boldsymbol{\rho}$, $\boldsymbol{\rho}_{ab}=-[(1-x)\boldsymbol{\rho}+x\boldsymbol{\rho}']$, and $T=\int dzn(z)$. This formula can be obtained from (14) by taking advantage of the representation of Ψ_a^{bc} in terms of K_{bc}^0 which was established in Ref. 7:

$$\Psi_a^{bc}(x,\boldsymbol{\rho})=\frac{i\lambda}{4E_a\sqrt{\pi x(1-x)}}\int_{-\infty}^{0}dzK_{bc}^0(\boldsymbol{\rho},0|0,z).$$

When divided by T, Eq. (16) gives a convenient formula for the Bethe–Heitler cross section in terms of the light-cone wave function. It worth noting that (16) (and (10) and (14) as well) is valid if one can neglect the transverse motion effects on the scale of the medium constituent size. This assumes that the typical value of $|z_2-z_1|$ in (10), (14), which can be regarded as the formation length associated with the $a\to bc$ transition at a given $\mathbf{q}_b$, $L_f(q_b)$, is much larger than the size of the medium constituent. If the LPM effect is not very strong the $L_f(q_b)$ can be estimated by replacing $m_{b,c}^2$ by $m_{b,c}^2+\mathbf{q}_b^2$ in the above formula for L_f. Note that for $L_f(q_b)\gg L$ the radiation rate can be written in terms of Ψ_a^{bc} for an arbitrary target density. In this case the target acts as a single scattering center and Eq. (14) can be written in a form like (16) but with the product $T\sigma_{\bar{a}bc}$ being replaced by $2\{1-\exp[-\frac{1}{2}T\sigma_{\bar{a}bc}]\}$. This representation generalizes the formula for the p_T-integrated spectrum derived in Ref. 13.

In the general case one can estimate the radiation rate using the parametrizations $\sigma_{\bar{i}i}=C_{ii}\boldsymbol{\rho}_i^2$, $\sigma_{\bar{a}bc}=C_{ab}\boldsymbol{\rho}_{ab}^2+C_{bc}\boldsymbol{\rho}_{bc}^2+C_{ca}\boldsymbol{\rho}_{ca}^2$ (here $\boldsymbol{\rho}_{ca}=-(\boldsymbol{\rho}_{ab}+\boldsymbol{\rho}_{bc})$). Then the Hamiltonian (12) takes the oscillator form with the frequency

$$\Omega(z)=\frac{(1-i)}{\sqrt{2}}\left[\frac{n(z)C(x)}{E_ax(1-x)}\right]^{1/2},$$

where $C(x)=C_{ab}(1-x)^2+C_{bc}+C_{ca}x^2$. The Green's function for the oscillator Hamiltonian with the z-dependent frequency can be written in the form

$$K_{\rm osc}(\boldsymbol{\rho}_2,z_2|\boldsymbol{\rho}_1,z_1)=\frac{\gamma(z_1,z_2)}{2\pi i}\exp\{i[\alpha(z_1,z_2)\boldsymbol{\rho}_2^2+\beta(z_1,z_2)\boldsymbol{\rho}_1^2-\gamma(z_1,z_2)\boldsymbol{\rho}_1\boldsymbol{\rho}_2]\}. \tag{17}$$

The functions α, β and γ in (17) can be evaluated in the approach of Ref. 14. Then we can integrate analytically over $\boldsymbol{\rho}_b$ in (10), and represent the radiation rate as

$$\frac{d^3P}{dxd\mathbf{q}_b}=\frac{1}{(2\pi)^2}\,\mathrm{Re}\int_{z_1<z_2}dz_1dz_2\,g\,\frac{\gamma(z_1,z_2)}{Q(z_1,z_2)}\exp\left[-\frac{i\mathbf{q}_b^2}{4Q(z_1,z_2)}+\frac{i(z_1-z_2)}{L_f}\right], \tag{18}$$

where the factor $Q(z_1,z_2)$ can be expressed through in terms of the parameters C_{ij}, the functions α, β, and γ, and n. The formula for this factor is cumbersome to be presented here.

Consider now the case when the particle a is produced in a medium or at finite distance from a target. Equation (10) holds in this case as well, but now z_i equals the coordinate of the production point. Given the representation (10) and making use of (13), one can obtain a formula similar to (14) but with $[\Phi_a-1]$ being replaced by Φ_a in the second term. Note, however, that, due to the infinite time required for the formation of Ψ_a^{bc}, Eq. (16) (and its analog for arbitrary density at $L_f(q_b)\gg L$) does not hold in this case.

Let us briefly discuss the totally inclusive radiation rate. It can be evaluated almost in the same way as the $\mathbf{q}_c$-integrated spectrum if one of the final particles has a zero charge, as this occurs for the $e\to\gamma e$ transition in QED. Consider the case when $e_c=0$. Since the particle c does not interact with the medium, the graph of Fig. 1a can be transformed into a graph like that of Fig. 1b but with the propagator K_c being connected to the lower abc vertex through the density matrix of the particle c. The corresponding formula [which is the analog of (10)] reads

$$\frac{d^5P}{dx\,d\mathbf{q}_b\,d\mathbf{q}_c}=\frac{2}{(2\pi)^2}\,\mathrm{Re}\int d\boldsymbol{\tau}_b\,d\boldsymbol{\tau}_c\exp[-i(\mathbf{q}_b\cdot\boldsymbol{\tau}_b+\mathbf{q}_c\cdot\boldsymbol{\tau}_c)]$$

$$\times\int_{z_i}^{z_f}dz_1\int_{z_1}^{z_f}dz_2\,g\Phi_b(\boldsymbol{\tau}_b,z_2)K_{bc}(\boldsymbol{\tau}_b-\boldsymbol{\tau}_c,z_2|0,z_1)\Phi_a(\boldsymbol{\tau}_a,z_1)\,, \qquad (19)$$

where $\boldsymbol{\tau}_a=x\boldsymbol{\tau}_b+(1-x)\boldsymbol{\tau}_c$. The z integration in (19) can also be written as in (14). In the low density limit and at $L_f(q_b)\gg L$ the initial- and final-state interactions vanish. For this reason the analog of (16) and a similar equation for arbitrary density at $L_f(q_b)\gg L$ which can be obtained from (19) are valid even when all the particles are charged.

The generalization of the above results to the realistic QED and QCD Lagrangians reduces to trivial replacements of the two- and three-body cross sections and the vertex factor g. The latter, due to spin effects in the vertex $a\to bc$, becomes an operator. The corresponding formulas are given in Refs. 6 and 15.

The formalism developed here can be applied to many problems. In particular, in QCD this approach can be used for evaluation of high-p_T hadron spectra, the p_T dependence of Drell–Yan pairs and heavy-quark production in hA collisions, and the angular dependence of the parton energy loss in hot QCD matter produced in AA collisions. It is also of interest for studying the initial condition for the quark–gluon plasma in AA collisions. Some of these problems will be discussed in further publications.

I would like to thank N. N. Nikolaev and D. Schiff for discussions. I am grateful to J. Speth for the hospitality at FZJ, Jülich, where this work was completed. This work was partially supported by INTAS Grant 96-0597 and DFG Grant 436RUS17/11/99.

[1)]Strictly speaking, in (1) and (5) a coupling which vanishes adiabatically at $|z|\sim|z_{i,f}|$ should be used. For simplicity we do not indicate the coordinate dependence of the coupling.

[2)]Note that the appearance of the eikonal absorption factors in (10) is a nontrivial consequence of the specific form of the evolution operators $S_{a,b}$ (Ref. 12) and is not connected with the applicability of the eikonal approximation in itself.

[3)]The diagram of Fig. 2b gives only the term $\propto K_{bc}$ in (15) (the corresponding integral is divergent in itself). Nonetheless, it yields the same result as (15). Indeed, by adding and subtracting the contribution from the configurations $z_1<z_f<z_2$, one can represent the contribution of the vacuum term as a sum of the imaginary term connected with the radiative correction to m_a [which is $\propto(z_f-z_i)$] and the real term related to the wave

function renormalization. The latter comes from the configurations $z_1<z_f<z_2$. This boundary effect is absent if the coupling vanishes at large $|z|$. In this case the vacuum term in (15) does not affect the x spectrum. It is, however, convenient to keep the vacuum term to simplify the troublesome z integration in (15). Again, it allows one to use a constant coupling.

[1] L. D. Landau and I. Ya. Pomeranchuk, Dokl. Akad. Nauk SSSR **92**, 535, 735 (1953).
[2] A. B. Migdal, Phys. Rev. **103**, 1811 (1956).
[3] R. Baier, Yu. L. Dokshitzer, S. Peigne, and D. Schiff, Phys. Lett. B **345**, 277 (1995).
[4] J. Knoll and D. N. Voskresenskii, Phys. Lett. B **351**, 43 (1995).
[5] R. Blankenbecler and S. D. Drell, Phys. Rev. D **53**, 6265 (1996);R. Blankenbecler, Phys. Rev. D **55**, 190 (1997).
[6] B. G. Zakharov, JETP Lett. **63**, 952 (1996).
[7] B. G. Zakharov, JETP Lett. **64**, 781 (1996).
[8] R. Baier, Yu. L. Dokshitzer, A. H. Mueller *et al.*, NMR **483**, 291 (1997);B **484**, 265 (1997).
[9] B. G. Zakharov, JETP Lett. **65**, 615 (1997); http://xxx.lanl.gov/abs/hep-ph/9807396; http://xxx.lanl.gov/abs/hep-ph/9805271.
[10] R. Baier, Yu. L. Dokshitzer, A. H. Mueller, and D. Schiff, NMR **531**, 403 (1998); Phys. Rev. C **58**, 1706 (1998).
[11] S. R. Klein, http://xxx.lanl.gov/abs/hep-ph/9802442.
[12] B. G. Zakharov, Yad. Fiz. **46**, 148 (1987) [Sov. J. Nucl. Phys. **46**, 92 (1987)].
[13] N. N. Nikolaev, G. Piller, and B. G. Zakharov, Zh Éksp. Teor. Fiz. **108**, 1554 (1995) [JETP **81**, 851 (1995)].
[14] B. Z. Kopeliovich and B. G. Zakharov, Phys. Rev. D **44**, 3466 (1991).
[15] B. G. Zakharov, Yad. Fiz. **61**, 924 (1998) [Phys. At. Nucl. **61**, 838 (1998)].

Published in English in the original Russian journal. Edited by Steve Torstveit.

Direct measurement of the spatial distribution of light intensity in a scattering medium

A. A. Karabutov, I. M. Pelivanov, N. B. Podymova,*) and S. E. Skipetrov
International Laser Center, M. V. Lomonosov Moscow State University, 119899 Moscow, Russia

(Submitted 7 June 1999)
Pis'ma Zh. Éksp. Teor. Fiz. **70**, No. 3, 187–191 (10 August 1999)

A direct nonperturbative measurement of the spatial distribution of the light intensity in a strongly scattering medium is performed using an optoacoustic method. It is shown that near a surface the intensity can be five times greater than the incident intensity, and the absolute maximum of the intensity is observed at a depth $\ell(1-R)(1-4.0R)$ determined by the photon transport mean free path ℓ and the effective light reflection coefficient R of the boundary separating the scattering and external media. © *1999 American Institute of Physics.* [S0021-3640(99)00615-5]

PACS numbers: 42.25.Fx, 43.35.Sx

Interest in the problem of multiple scattering of classical waves, primarily light, in randomly nonuniform media has undergone a vigorous revival in the last ten years. This is due to the diversity of new physical effects observed (or expected) under multiple scattering conditions — correlations of the scattered radiation, coherent backscattering, Anderson localization of light, and so on[1] — and to important applications of optical diagnostics methods in medicine.[2]

In the vast majority of multiple-scattering experiments the *outgoing* radiation from the medium is detected, since placing the detecting apparatus inside the medium (when it is possible to do so at all) inevitably results in distortion of the scattering pattern. At the same time, the characteristics of the radiation *inside* the scattering medium are also of interest from the fundamental and applied standpoints.

In the present work the spatial light intensity distribution in a scattering medium was measured directly. The method employed for this is based on the optoacoustic effect, wherein ultrasonic waves are excited thermooptically in the experimental medium when pulsed laser radiation is absorbed in it.[3] In recent years the optoacoustic effect has been widely used for diagnostics of randomly inhomogeneous media.[4]

When a laser pulse with duration τ_L much shorter than the transit time of an acoustic wave through the region of heat release ($\alpha v \tau_L \ll 1$, a is the light extinction coefficient and v is the sound velocity in the medium) is absorbed in a medium, the form of the ultrasonic pulse (optoacoustic (OA) signal) replicates the spatial distribution of the thermal sources in the medium.[3] For a uniformly absorbing and scattering medium, this distribution in the plane wave approximation for the light is identical to the spatial distribution of

the light intensity in the medium. Then the intensity of the laser radiation in the medium can be represented as

$$I(z,t)=I(z)f(t)\simeq I(z)\tau_L\delta(t). \tag{1}$$

In turn, the leading edge of the pressure pulse in the traveling acoustic wave excited in the medium is given by the expression[3,4]

$$p(\tau=t-z/v<0)=\frac{\beta v^2}{2c_p}\mu_a E_0\frac{I(-v\tau)}{I_0}, \tag{2}$$

where β is the thermal expansion coefficient, c_p is the specific heat of the medium, μ_a is the light absorption coefficient, and $E_0=I_0\tau_L$ is the laser energy density at the surface of the medium.

As is evident from Eq. (2), the leading edge of the OA signal, $p(\tau<0)$, replicates the spatial distribution of the light intensity in the medium, and the time scale of variation of p and the spatial scale of variation of $I(z)$ are related via the sound velocity in the medium: $z=-v\tau$. Here $\tau=0$ is the time when the OA signal excited at the surface $z=0$ of the sample arrives at the acoustic detector (in the direct scheme for detecting the OA signal in an absorbing medium; see Refs. 3 and 4). After determining the time $\tau=0$ on the experimentally obtained temporal profile of the OA signal with allowance for diffraction,[4] one can use Eq. (2) to convert the time dependence of the leading edge of the OA signal $p(\tau<0)$ into the spatial dependence $I(z)$. Thus the optoacoustic method makes it possible to perform a direct measurement of the spatial light intensity distribution in a scattering medium, if the light absorption coefficient, the sound velocity, and the thermophysical parameters of the medium as well as the incident energy density are known.

In our experiments the model scattering medium, consisting of an aqueous suspension of 0.76 μm in diameter polystyrene beads (the volume concentration of the beads $\Phi=0.75\%$), was irradiated with pulses from a Q-switched Nd:YAG laser (wavelength $\lambda=1.06$ μm, pulse duration $\tau_L=12$ ns) in a direction normal to the surface of the medium. On the surface of the suspension the laser radiation, which had been passed beforehand through a glass diffusing filter, had a nearly Gaussian transverse intensity distribution with a characteristic beam radius $a=2.6$ cm. The acoustic pulses excited in the suspension were detected with a wideband piezoelectric detector, absolutely calibrated in the spectral range 0.03–8 MHz; the low-frequency sensitivity of the detector was 13.5 $\pm$0.1 mV/Pa. The detector was placed on the side opposite to the irradiated surface of the suspension, and it was in acoustic contact with the cell (direct detection scheme). The electric signal from the piezoelectric detector was recorded with a Tektronix TDS 220 digital real-time oscilloscope (the analog frequency band was 100 MHz and the sample rate was 1 GHz) and averaged over 64 time series.

Since the volume concentration of particles was low, we could assume that the refractive index, the light absorption coefficient, and the thermophysical parameters of the suspension have the same as their values as for water ($n=1.326$, $\mu_a=0.16\,\mathrm{cm}^{-1}$, $\beta=1.82\,\mathrm{K}^{-1}$, $c_p=4.18$ J/g·K). The ultrasonic absorption coefficient in water in the experimental frequency range does not exceed $K=2.5\times10^{-2}\mathrm{cm}^{-1}$, so that we neglected

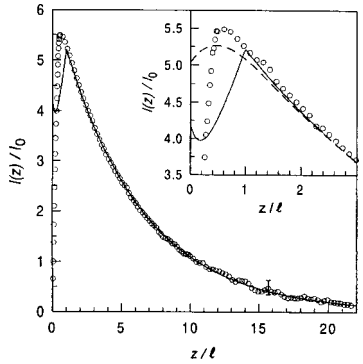

FIG. 1. Spatial distribution of the light intensity in a semi-infinite randomly inhomogeneous medium (aqueous suspension of polystyrene beads 0.76 μm in diameter; the particle volume concentration is 0.75%; the photon transport mean free path $\ell = 628$ μm): circles — experimental data, solid line — analytical calculation in the diffusion approximation, dashed line — Monte Carlo calculation.

the effect of absorption on the form of the OA signal as it propagates in the suspension (cell height $L = 2$ cm $\ll K^{-1}$). The measured sound velocity in the suspension was $v = (1.49 \pm 0.01) \times 10^5$ cm/s.

Relation (2) can be used to calculate $I(z)/I_0$ from the measured time dependence of the leading edge of the OA signal $p(\tau < 0)$. However, this relation holds only for $z > z_{\min} = v/f_{\max}$, where $f_{\max}$ is the frequency upper bound of the spectral range of the piezoelectric detector. For our experimental setup $z_{\min} \simeq 200$ μm. On this basis it is possible to perform a direct nonperturbative measurement of the spatial distribution $I(z)/I_0$ of the radiation intensity in a scattering medium for $z > z_{\min}$. The results of such a measurement are displayed in Fig. 1. For convenience, we normalize z to the transport photon mean free path ℓ/μ_s' in the medium, where μ_s' is the reduced light scattering coefficient.

We shall now compare the measured distribution $I(z)/I_0$ with the distributions calculated analytically and numerically by the Monte Carlo method. For the analytical calculation of the spatial distribution of the radiation intensity in a randomly nonuniform medium, we shall assume that the medium occupies the half space $z > 0$ and that the radius of the beam incident on it is infinite. Such an approximation is admissible if the thickness of the medium and the beam radius are much greater than ℓ. We represent the radiation intensity in the medium as a sum of the coherent and diffuse components,

$$I(z,t) = I_{\text{coh}}(z,t) + I_{\text{dif}}(z,t), \tag{3}$$

where I_{dif} is the radiation intensity averaged over a 4π solid angle. The coherent component decays exponentially as a function of distance: $I_{\text{coh}}(z,t) = I_0 f(t) \exp[-(\mu_a + \mu_s)z]$, μ_s is the light-scattering coefficient in the medium, and for $\mu_a \ll \mu_s'$ the diffuse component is described by the diffusion equation[5,6]

$$\left[\nabla^2 - \alpha^2 - \frac{1}{D}\frac{\partial}{\partial t}\right] I_{\text{dif}}(z,t) = -\frac{cI_0 f(t)}{D}\delta(z - z_1). \tag{4}$$

Here $I_0 f(t)$ is the intensity of the radiation incident on the medium, c is the speed of light in the medium, D is the diffusion coefficient of light, $\alpha^2 = 3\mu_a \mu_s'$, $z_1 \simeq \ell$ is the distance at which the collimated incident radiation is converted into diffuse radiation. For $\tau_L \gg (\mu_a c)^{-1}$, which in our case holds well, the time derivative on the left-hand side of Eq. (4) can be neglected.

We shall use as the boundary condition for Eq. (4) the condition that I_{dif} vanishes on the so-called extrapolated boundary[7] — the plane $z = -z_0 = -\Delta\ell$, where $\Delta = \frac{3}{2}(1+R)/(1-R)$ and R is the effective internal reflection coefficient for diffuse radiation reflected from the boundary of the scattering and transparent media.[8] This boundary condition gives

$$I_{\text{dif}}(z) = \frac{I_0}{2}\sqrt{\frac{3\mu_s'}{\mu_a}}\{\exp[-\alpha|z-z_1|] - \exp[-\alpha(z+2z_0+z_1)]\}. \tag{5}$$

Assuming the refractive index of water and polystyrene to be $n_1 = 1.326$ and $n_2 = 1.559$, respectively, we obtain[1)] from the Mie theory[5] $\mu_s' = 15.92\,\text{cm}^{-1}$ and $\ell = 628$ μm. The calculation of the parameter Δ using the integral relation obtained for R in Refs. 8 gives $\Delta = 1.66$. The dependence $I(z)/I_0$ obtained in the process is displayed in Fig. 1 (solid line).

To calculate $I(z)$ by the Monte Carlo method we simulated the multiple scattering of a large number of photons ($N = 10^6$) in a randomly nonuniform medium, as done, for example, in Refs. 9. The Henyey–Greenstein formula with anisotropy index $g = 0.782$, calculated according to the Mie theory for scatterers with a diameter of 0.76 μm, was used for the scattering diagram of an individual particle. The probability of internal reflection at the medium–air boundary was calculated using the Fresnel formulas.[10] The simulated curve $I(z)/I_0$ is shown in the inset in Fig. 1 (dashed line). For $z > \ell$ the results of the numerical simulation agree with the analytical results.

As one can see from the figure, for $z > \ell$ the measured dependence $I(z)/I_0$ is in excellent agreement with the computed dependences. In this range $I(z)$ can be described by the simple expression $I(z) \propto \exp(-\alpha z)$ [see Eq. (5)], which makes it possible to determine μ_s' if μ_a is known. The value that we obtained $\mu_s' = 16.45\text{cm}^{-1}$ agrees well with the computed value $\mu_s' = 15.92\,\text{cm}^{-1}$.

For $z < \ell$ the experimental, analytical, and numerical results disagree. The diffusion theory becomes inapplicable in this range, since low-order scattering processes play a large role near the boundary of the medium. The disagreement between the numerical and experimental results is probably due to factors that were neglected in the numerical model but that are important near the boundary of the medium: the vector nature of the electromagnetic radiation, the possibility of interference of scattered waves, the difference between the Henyey–Greenstein model phase function and the phase function corresponding to Mie scattering, and the finite dimensions of the laser beam and cell.

We note that for $z < 10\ell$ the radiation intensity in the scattering medium is greater than the incident radiation intensity ($I(z)/I_0 > 1$). This increase in the intensity in a subsurface layer occurs because of diffuse reflection of the scattered radiation from deeper layers in the medium. A sample of a randomly nonuniform medium can therefore be interpreted as a cavity with one mirror at $z = 0$ (reflection occurs as a result of a difference of the refractive indices of the scattering and external media) and the other

distributed continuously over the half space $z>0$ (reflection is due to scattering). Just as in any cavity, concentration of electromagnetic energy should occur in a sample of the randomly inhomogeneous medium, as is observed experimentally.

For $z=z_{\max}\simeq\ell/2$ the quantity $I(z)$ possesses an absolute maximum, and $I(z_{\max})$ is more than five times greater than the light intensity I_0 incident on the medium. The Monte Carlo calculation of $I(z)$ for various ratios of the refractive indices of the scattering and external media showed that the position of the maximum of the intensity is determined by an effective reflection coefficient R of the air–medium boundary for diffuse radiation and can be approximately described by the formula $z_{\max}\simeq\ell(1-R)(1-0.4R)$.

The factors μ_a and μ_s' can be determined simultaneously by interpolating the experimentally measured function $I(z)$ in the region $z>\ell$ using Eq. (5). This makes it possible to suggest a new method for performing independent measurements of the absorption and scattering coefficients of turbid media. This method is an alternative to the all-optical method based on measurement of the temporal profiles of short pulses transmitted through a turbid medium.[11]

We shall now sum up. In the present work, a direct nonperturbative measurement of the spatial intensity distribution $I(z)/I_0$ of optical radiation in a scattering medium was performed and its features were studied. It was shown that $I(z)\propto\exp(-\sqrt{3\mu_a\mu_s'}z)$ at depths $z>\ell$. Near the boundary of the medium, for $z<10\ell$, the radiation intensity is greater than the intensity I_0 of the incident wave, and at some point $z=z_{\max}$ it reaches an absolute maximum, which can be five times greater than I_0. An approximate formula was found for $z_{\max}$: $z_{\max}\simeq\ell(1-R)(1-0.4R)$. The substantial increase in the radiation intensity near the surface of a scattering medium must be taken into consideration in cases where the light intensity in the medium is limited (for example, in medical applications).

This study was supported by the Russian Fund for Fundamental Research (Grant 98-02-17112). The work of S. E. Skipetrov was also supported by the International Center for Fundamental Physics in Moscow (INTAS Grant 96-0457) and the Moscow Research Center of the Samsung Electronics Company Ltd.

*)e-mail: natasha@gpwp1.phys.msu.su

1)The computater code is available on the Internet at http://www.ilc.msu.su/~skipetr/.

[1] *Diffuse Waves in Complex Media*, edited by J.-P. Fouque (Dordrecht, 1999); P. Sheng, *Introduction to Wave Scattering, Localization, and Mesoscopic Phenomena* (San Diego, 1995).
[2] V. B. Tuchin, *Lasers and Tissue Optics in Biomedical Research* [in Russian] (Izd. Saratovsk. Univ., Saratov, 1998); A. J. Welch and M. C. J. van Gemert (eds.), *Tissue Optics* (New York, 1992).
[3] V. E. Gusev and A. A. Karabutov, *Laser Optoacoustics* (Nauka, Moscow, 1991).
[4] L. A. Aslanov, A. A. Karabutov, N. B. Podymova *et al.*, Laser Phys. **6,** 1105 (1997);A. A. Karabutov, N. B. Podymova, and V. S. Letokhov, Appl. Phys. B: Photophys. Laser Chem. **63,** 545 (1996).
[5] G. van de Hulst, *Light Scattering by Small Particles* (Dover Publications, New York, 1981) [Russian translation, Inostr. Lit., Moscow, 1961].
[6] K. Furutsu and Y. Yamada, Phys. Rev. E **50,** 3634 (1994).
[7] P. M. Morse and H. Feshbach, *Methods of Theoretical Physics* (McGraw-Hill, New York, 1953) [Russian translation, Inostr. Lit., Moscow, 1958].
[8] R. C. Haskell, L. V. Swaasand, T. Tsay *et al.*, J. Opt. Soc. Am. A **11**, 2727 (1994);D. J. Durian, Phys. Rev. A **50**, 857 (1994); J. X. Zhu, D. J. Pine, and D. A. Weitz, Phys. Rev. A **44**, 3948 (1991).
[9] S. E. Skipetrov and S. S. Chesnokov, Kvant. Elektron. (Moscow) **25**, 753 (1998);G. I. Marchuk, G. A.

Mikhaĭlov, M. A. Nazarliev *et al.*, *Monte Carlo Methods in Atmospheric Optics* (Nauka, Nobosibirsk, 1974).
[10] L. D. Landau and E. M. Lifshitz, *Electrodynamics of Continuous Media*, 2nd ed., rev. and enl., with L. P. Pitaevskii (Pergamon Press, New York, 1984) [cited Russian original, Nauka, Moscow, 1992].
[11] J. C. Hebden, F. E. W. Schmidt, M. E. Fry *et al.*, Opt. Lett. **24,** 534 (1999);M. S. Patterson, B. Chance, and B. C. Wilson, Appl. Opt. **28**, 2331 (1989).

Translated by M. E. Alferieff

Two-photon fluorescence spectrum in an atom + dielectric microsphere system

V. V. Klimov*)
P. N. Lebedev Physics Institute, Russian Academy of Sciences, 117924 Moscow, Russia

V. S. Letokhov
Institute of Spectroscopy, Russian Academy of Sciences, 142092 Troitsk, Moscow Region, Russia

(Submitted 9 June 1999; resubmitted 6 July 1999)
Pis'ma Zh. Éksp. Teor. Fiz. **70**, No. 3, 192–197 (10 August 1999)

A strong resonant interaction of a two-level atom with a dielectric microsphere is studied on the basis of quantum electrodynamics. The initial condition considered is one in which the atom is initially excited and the resonant mode of the microsphere has been excited by a single photon. The spectrum of two emitted photons depends strongly on the method used to excite the microsphere, i.e., on the spatial distribution of the photon energy. The most characteristic feature of the two-photon fluorescence spectrum is a strong energy correlation of the emitted photons. This correlation is expressed in the fact that the energies of the emitted photons are related by the equation of an ellipse $(\omega_1+\omega_2-2\omega_A)^2+3(\omega_1-\omega_2)^2=4\Omega_{\rm Rabi}^2$. The relation between the results obtained and the predictions of the theory of dressed states is discussed.
 [S0021-3640(99)00715-X]

PACS numbers: 32.50.+d, 32.80.Wr

The main properties of a dielectric microsphere viewed as a cavity are its high Q in the optical range and the small effective volume of a mode.[1–3] Such a microsphere is a good ''trap'' for photons, and even a single photon can be characterized by a high electric field intensity near the surface of the microsphere. Accordingly, an atom placed in the high-field region can interact strongly with a resonant mode of the microsphere when the latter contains a small number of photons or even no photons at all.

The single-photon fluorescence spectrum of an atom + microsphere system has been well-studied.[4,5] The structure of this spectrum depends strongly on the method used to excite the system. For a sufficiently strong atom–microsphere interaction, the single-photon fluorescence spectrum can possess singlet, doublet, or triplet forms.

The objective of the present work is to investigate further an atom–microsphere system in the strong resonant interaction regime. As initial conditions we consider the case of excitation of the system such that the atom is in an excited state and there is one photon in a resonant mode of the microsphere. It should be noted that the presence of only one photon in a resonant mode of the microsphere does not mean that the field has a single-mode structure. In the present investigation, in accordance with the the general

principles of quantum electrodynamics, we assume that there is a large number (in the limit a continuum) of quantized modes of the electromagnetic field within the contour of a resonant mode of the microsphere.

Such initial conditions are not exotic and can always be realized when the excited atom enters a cavity containing a single photon. Experimental setups of this kind already exist[6] or are under development.[7]

To describe the properties of the two-photon fluorescence spectrum, it is necessary to use the quantum theory of the resonant interaction of an excited atom with a microsphere whose resonant mode contains a single photon. The quantization of the electromagnetic field in spherical geometry is well-known.[8] The quantum theory for a dielectric microsphere has been studied in Refs. 5 and 9.

For a resonant interaction of a two-level atom located at the point $\mathbf{r}$ with a continuum of quantized radiation modes falling within the contour of the whispering-gallery mode, the dipole Hamiltonian can be represented as[10]

$$H = H_A + H_F + H_I, \tag{1}$$

where the Hamiltonians of the atom H_A, the field H_F, and the interaction H_I are

$$H_A = \hbar\omega_A \begin{pmatrix} 1 & \\ & 0 \end{pmatrix}, \quad H_F = \sum_s \hbar\omega_s \left[a_s^+ a_s + \frac{1}{2} \right], \quad H_I = \begin{pmatrix} 0 & -\mathbf{d}\cdot\hat{\mathbf{E}} \\ -\mathbf{d}^*\cdot\hat{\mathbf{E}} & 0 \end{pmatrix}, \tag{2}$$

$$\hat{\mathbf{E}} = \sum_s \frac{a_s \mathbf{e}(s,\mathbf{r}) - a_s^+ \mathbf{e}^*(s,\mathbf{r})}{i\sqrt{2}}. \tag{3}$$

In Eqs. (2) and (3) $\mathbf{d}$ is the matrix element of the transition dipole moment and a_s and a_s^+ are operators creating and annihilating a photon in the sth mode. The index s, characterizing a quantized mode in the presence of a microsphere, is of a vector character, $s=(n,m,\nu)$, where n, m and ν are the orbital, azimuthal, and radial quantum numbers, respectively. The frequency of the quantized mode

$$\omega_s = \nu\frac{\pi c}{\Lambda} + \ldots \tag{4}$$

is determined by the radial wave number ν and the radius of the quantization sphere $\Lambda\to\infty$. Explicit expressions for the electric field intensity of the sth mode $\mathbf{e}(s,\mathbf{r})$ can be found in Ref. 5.

In the rotating-wave approximation the ground state, the first excited manifold, the second excited manifold, and so on do not interact and can be studied separately. Our main problem is to study the interaction of an excited atom with the quantized modes that fall within the contour of one of the resonance modes (the whispering-gallery mode).

To solve this problem, the Schrödinger equation describing the dynamics of the second excited manifold must be solved directly. If the continuum of quantized modes is described by n quantized modes ($n\to\infty$), then the Schrödinger equation reduces to a system of $n(n+3)/2$ linear differential equations for the amplitudes of different states. The vector of the probability amplitudes of the second excited manifold has the form

$$\Psi(t)=[\underbrace{\psi_1^A(t),\ldots,\psi_n^A(t),\ldots}_{1},\underbrace{\psi_{1,1}^{\mathrm{Ph}}(t),\ldots,\psi_{n,n}^{\mathrm{Ph}}(t),\ldots}_{2},\underbrace{\psi_{1,2}^{\mathrm{Ph}}(t),\ldots,\psi_{n-1,n}^{\mathrm{Ph}}(t)\ldots}_{3}], \quad (5)$$

where the first n components describe the probability amplitudes for finding an atom in an excited state and one photon in one of the quantized modes. The second n components describe the probability amplitudes for finding an atom in the ground state and two photons in one of the quantized modes. Finally, the remaining $n(n-1)/2$ components describe the probability amplitudes for finding an atom in the ground state and two photons in various quantized modes.

In the frequency domain, the Schrödinger equation reduces to a system of ordinary linear equations

$$\begin{aligned}
&(\omega-\omega_i-\omega_A)\psi_i^A(\omega)=i\psi_i^A(0)+\sum_{s\neq i}V_s\psi_{i,s}^{\mathrm{Ph}}(\omega)+\sqrt{2}\psi_{i,i}^{\mathrm{Ph}}(\omega)V_i,\\
&(\omega-2\omega_i)\psi_{i,i}^{\mathrm{Ph}}(\omega)=\sqrt{2}V_i^*\psi_i^A(\omega), \quad (6)\\
&(\omega-\omega_i-\omega_j)\psi_{i,j}^{\mathrm{Ph}}(\omega)=V_j^*\psi_i^A(\omega)+V_i^*\psi_j^A(\omega)(i\neq j).
\end{aligned}$$

Here the first n equations describe the frequency evolution of the atomic probability amplitude, and the terms on the right-hand side describe the initial state and the emission of a photon into unoccupied and occupied modes. The second n equations describe the dynamics of photon emission into an occupied mode (stimulated emission by an atom). Finally, the remaining $n(n-1)/2$ equations describe the emission of a photon into an unoccupied mode (spontaneous emission of an atom).

The matrix element of the interaction energy of an atom interacting with different quantized modes within the contour of the resonant mode,

$$V_s=V(\omega_s)=-\frac{\mathbf{d}\cdot\mathbf{e}(s,\mathbf{r})}{i\hbar\sqrt{2}}, \quad (7)$$

will have a resonant dependence on the frequency of the mode. Figure 1 shows the dependence of the dipole interaction energy of a two-level atom interacting with the quantized modes. Here the solid line shows the contour of the whispering-gallery mode, and the vertical lines show the frequencies of the quantized modes. The distances between the modes decrease as the quantization volume increases, and in the limit one can talk about a continuum of quantized modes falling within the resonant contour of a microsphere.

Elimination of the photon modes from the system (6) gives a system of n linear equations for the probability amplitudes for finding an atom in the excited state ($\epsilon\to 0^+$):

$$(\omega-\omega_i-\omega_A)\psi_i^A(\omega)=i\psi_i^A(t=0)+\sum_s\frac{V_sV_s^*\psi_i^A(\omega)+V_sV_i^*\psi_s^A(\omega)}{(\omega-\omega_i-\omega_s+i\epsilon)}. \quad (8)$$

After solving Eq. (8), there is no need to return to the time domain to find the fluorescence spectrum, since the amplitudes of the two-photon states in the limit $t\to\infty$ can be expressed in terms of the frequency components of the atomic states:

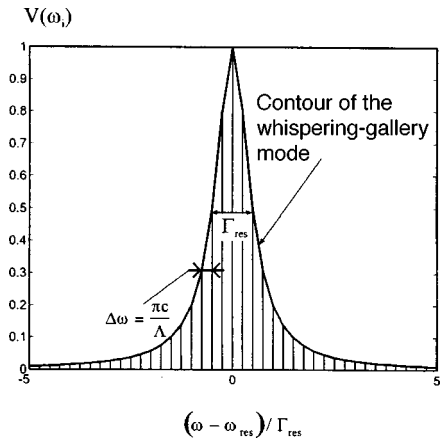

FIG. 1. Interaction energy of an atom interacting with quantized modes modified by the presence of a dielectric microsphere as a function of frequency.

$$\psi^{\mathrm{Ph}}_{i,j}(t\to\infty)=V^*_j\,\psi^A_i(\omega_i+\omega_j)+V^*_i\,\psi^A_j(\omega_i+\omega_j)(i\neq j),\qquad \psi^{\mathrm{Ph}}_{i,i}(t\to\infty)=\sqrt{2}V^*_i\,\psi^A_i(2\omega_i). \tag{9}$$

It is evident from these expressions that the two-photon final states are entangled and strong correlations between them are to be expected.

The asymptotic occupation probabilities of various states of the two-photon continuum, i.e., the two-photon fluorescence spectrum

$$P(\omega_i,\omega_j)=\frac{|\psi^{\mathrm{Ph}}_{i,j}(t\to\infty)|^2}{\Delta\omega^2}, \tag{10}$$

can be found in terms of the asymptotic expressions for the photon amplitudes (9). Figure 2 shows the two-photon radiation spectrum for optimal single-photon excitation of a diamond microsphere ($\epsilon=6$) with radius a. The parameters of the atom and microsphere are chosen so that a resonant interaction would occur with the TM (1, 11, 0) whispering-gallery mode (mode with no zeros in the radial direction).

It is evident, first and foremost, from this figure that the frequencies of the emitted photons lie on an ellipse, i.e., they are strongly correlated. This correlation in the strong-interaction limit (when the vacuum Rabi frequency defined as $\Omega^2_{\mathrm{Rabi}}=\Sigma_i|V_i|^2$ is large compared with the width of the resonance of the microsphere, $\Omega_{\mathrm{Rabi}}\gg\Gamma_{\mathrm{res}}$) is described by the simple equation

$$(\omega_1+\omega_2-2\omega_A)^2+3(\omega_1-\omega_2)^2=4\Omega^2_{\mathrm{Rabi}}. \tag{11}$$

In addition, peaks that can be expected on the basis of the theory of dressed states are present in the spectrum.[11] The peaks arising in the dressed-states picture correspond to two photons, one of which is formed with a transition from an upper sublevel of the second level to the upper sublevel of the first level and the other is formed with a transition from the upper sublevel of the first level into the ground state (transitions *3* and *4* in Fig. 3). A similar photon pair is emitted in a transition between the bottom sublevels

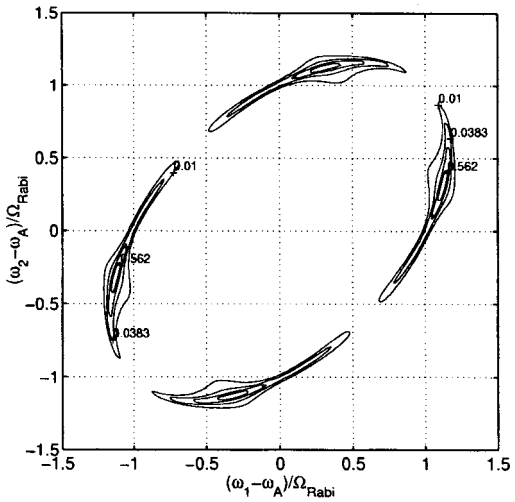

FIG. 2. Two-photon fluorescence spectrum versus the frequencies of the emitted photons with optimal excitation of the microsphere ($\psi_i^A(t=0)\propto V_i^*$, $\epsilon=6$, $\alpha\approx\lambda=0.5$ μm, $\omega=3.77\times10^{15}\,s^{-1}$, $\gamma_0=1.5\times10^8\,s^{-1}$, $\Omega_{Rabi}=1.3\times10^{11}\,s^{-1}$, $r/a=0.8$).

(transitions *5* and *6* in Fig. 3). An important difference of our results from the dressed-states picture is that we do not observe transitions between the top and bottom sublevels (shown by dashed lines in Fig. 3).

It is easy to find the single-photon spectrum from the two-photon spectrum by averaging over one frequency:

$$S_1(\omega_1)=\int d\omega_2 P(\omega_1,\omega_2). \tag{12}$$

Spectra of this kind have been analyzed in Refs. 12 and 13 on the basis of the density-matrix method. In these works it was shown that, besides the standard Rabi components,

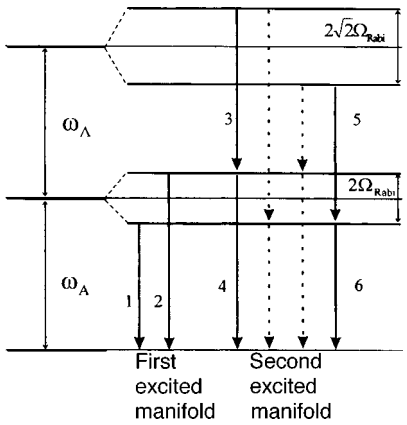

FIG. 3. Structure of the spectrum of dressed states.

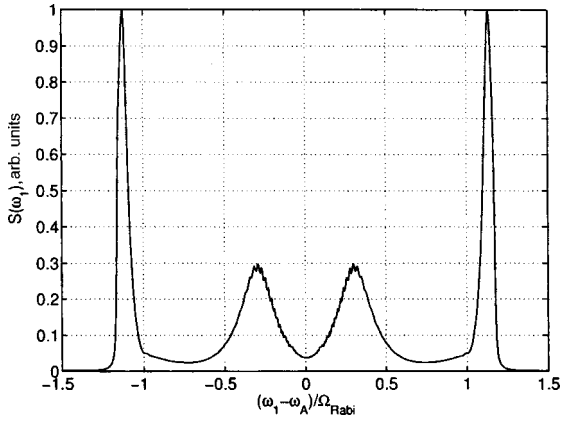

FIG. 4. Single-photon spectrum with optimal excitation of a microsphere ($\psi_i^A(t=0) \propto V_i^*$, $\epsilon=6$, $\alpha \approx \lambda = 0.5$ μm, $\omega = 3.77\times10^{15}\ \mathrm{s}^{-1}$, $\gamma_0 = 1.5\times10^{8}\ \mathrm{s}^{-1}$, $\Omega_{\mathrm{Rabi}} = 1.3\times10^{11}\ \mathrm{s}^{-1}$, $r/a = 0.8$).

components with the difference frequency $\omega_A \pm (\sqrt{2}-1)\Omega_{\mathrm{Rabi}}$ and with the sum frequency $\omega_A \pm (\sqrt{2}+1)\Omega_{\mathrm{Rabi}}$ arise in the one-photon photoluminescence spectrum.

Figure 4 shows the single-photon spectrum which we found for optimal excitation of a microsphere by one photon, i.e., for the case where initially the maximum field acts on the atom. Two components, one close to the frequency $\omega_A \pm \Omega_{\mathrm{Rabi}}$ and the other close to the difference frequency $\omega_A \pm (\sqrt{2}-1)\Omega_{\mathrm{Rabi}}$, are clearly expressed in the spectrum. The sum frequencies do not arise in our approach.

To check experimentally the existence of elliptic correlations between the energies of the emitted photons, it is not enough to measure the spectrum of one of the photons, since the basic features of the two-photon spectrum are effaced in it. A complete reconstruction of the elliptical structures requires measurements of the spectrum of one of the photons for various fixed energies of the other photon.

In summary, we have shown that in the two-photon fluorescence spectrum in the atom + microsphere system the emitted photons are strongly energy-correlated. This correlation is expressed in the fact that clearly defined elliptical structures arise in the two-dimensional spectrum. The results obtained are also applicable to other cases of two-photon fluorescence in an atom + cavity system.

We thank the Russian Fund for Fundamental Research for providing financial support for this work.

*)e-mail: klimov@rim.phys.msu.su

[1] V. B. Braginsky, M. L. Gorodetsky, and V. S. Ilákhenko, Phys. Lett. A **137**, 393 (1989).
[2] L. Collot, V. Lefevre, M. Brune *et al.*, Europhys. Lett. **23**, 327 (1993).
[3] M. L. Gorodetsky, A. A. Savchenkov, and V. S. Ilchenko, Opt. Lett. **21**, 453 (1996).
[4] V. V. Klimov and V. S. Letokhov, JETP Lett. **68**, 124 (1998).
[5] V. V. Klimov, M. Ducloy, V. S. Letokhov, Phys. Rev. A **59**, 2996 (1999).
[6] C. J. Hood, M. S. Chapman, T. W. Lynn, and H. J. Kimble, Phys. Rev. Lett. **80**, 4157 (1998).
[7] F. Treussart, J. Hare, L. Collot *et al.*, Opt. Lett. **19**, 1651 (1994).

[8] A. S. Davydov, *Quantum Mechanics*, 2nd edition (Pergamon Press, New York, 1976) [Russian original, Nauka, Moscow, 1973].
[9] S. C. Ching, H. M. Lai, and K. Young, J. Opt. Soc. Am. B **4**, 1995 (1987); **4**, 2004 (1987).
[10] D. P. Craig and T. Thirunamachandran, *Molecular Quantum Electrodynamics* (Academic Press New York, 1984).
[11] S. Haroche, ''Cavity quantum electrodynamics,'' in *Fundamental Systems in Quantum Optics*, Proceedings of Les Houches Summer School, Session LIII, 25 June–27 July, 1990, edited by J. Dalibard, J.-M. Raimond, and J. Zinn-Justin (North-Holland, Amsterdam–New York, 1992), p. 766.
[12] G. S. Agarwal, J. Mod. Opt. **45**, 449 (1998).
[13] M. Löffler, G. M. Meyer, and H. Walther, Phys. Rev. A **55**, 3923 (1997).

Translated by M. E. Alferieff

Experimental investigation of the longitudinal relaxation time of electronic polarization of the ground state of potassium atoms in a cell with an antirelaxation coating on the walls

M. V. Balabas, M. I. Karuzin, and A. S. Pazgalev
S. I. Vavilov State Optics Institute, 199034 St. Petersburg, Russia

(Submitted 2 June 1999)
Pis'ma Zh. Éksp. Teor. Fiz. **70**, No. 3, 198–202 (10 August 1999)

We report the results of an experimental investigation of the longitudinal relaxation time T_1 of the electronic polarization of the ground state of potassium atoms in cells with an antirelaxation coating on the walls. Investigations were performed for a number of cells at temperature $T=24°$C. The maximum recorded relaxation times τ are 3.6, 4.3, and 5.2 s for cells with diameter $D=50,75$, and 100 nm, respectively. These are the longest longitudinal relaxation times ever recorded in coated cells. The transverse relaxation time was measured for these cells at the same temperature: $T_2=0.72,1.1$, and 1.4 s, respectively. © *1999 American Institute of Physics.* [S0021-3640(99)00815-4]

PACS numbers: 32.60.+i, 32.10.Dk

Potassium-vapor cells with an antirelaxation coating on the walls[1] are used in precision quantum magnetometers,[2,3] in an experiment being planned for measuring the nuclear anapole moment of potassium,[4] and in experiments on nonlinear magnetooptic rotation in rubidium vapor.[5] Our attention so far has been focused completely on investigating ways to increase the transverse relaxation time T_2, since it determines the dark width of the radio-optic double resonance line and the Q of the M_x signal. The maximum amplitude of the M_z signal depends on the quantity $\sqrt{T_2/T_1}$, and the highest Q for the M_z signal obtains when $T_1=T_2$.

To date there are no comparative experimental data on the longitudinal T_1^C and transverse T_2^C relaxation times on a coating in the same cells. It is generally assumed[6] that $T_1^C=T_2^C$. In the present letter we report the results of our investigations of the longitudinal and transverse relaxation times.

The time T_1 is usually studied experimentally by the Franzen method[7] with Zeeman optical pumping. The measure of relaxation is the change in the absorption of circularly polarized light as a result of a change Δn_i in the distribution of the populations of the Zeeman sublevels of the ground state on account of relaxation transitions between them: $S(t)=\Sigma\Delta n_i(t)W_i$, where W_i are the relative absorption probabilities of σ^+ polarized light. It is well known[8,9] that the detected signal in this case is characterized by two exponentials. For atoms with a nuclear spin I the signal has the form

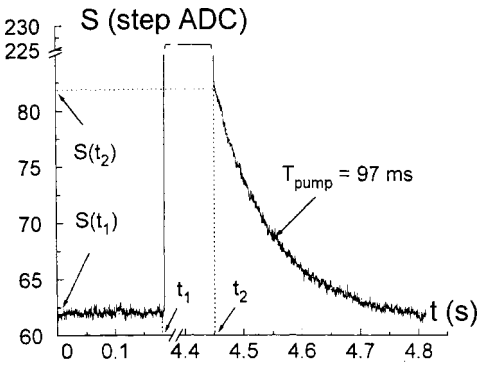

FIG. 1. Form of the signal for a dark pause $t=t_2-t_1=4.27$ s. The signal amplitude is given in units of the least-significant bit of the analog-to-digital converter (ADC). Details are given in the text.

$$S(t)=(1-a)\exp(-t/\tau_1)+a\exp(-t/\tau_2), \tag{1}$$

where $a=2\langle I_z(0)\rangle/(4I^2+4I-1)\langle S_z(0)\rangle$, and $\langle S_z(0)\rangle$ and $\langle I_z(0)\rangle$ are the electronic and nuclear polarizations of the optically pumped atoms. The factors $1/\tau_1$ and $1/\tau_2$ in the arguments of the exponential functions are determined as the weighted sums of the relaxation rates of individual relaxation channels. For spin $I=3/2$ the maximum possible ratio of the exponents in Eq. (1) is $\tau_1/\tau_2=8$ (Ref. 9).

The Franzen signal is formed as follows. A vapor of atoms is irradiated in the direction of the magnetic induction vector by circularly polarized light of the D_1 line of the ground-state doublet, with equal intensities of its hyperfine components. As a result, the ensemble of atoms acquires a macroscopic electronic magnetic moment. After the light source is covered, the electronic polarization of the ground state relaxes in the dark. After a certain time, the cell is irradiated again. The difference of the light intensities $S(t_1)$ at the moment before covering and $S(t_2)$ at the moment irradiation is resumed as a function of the duration $t=t_2-t_1$ of the dark pause describes the relaxation process (Figs. 1 and 2).

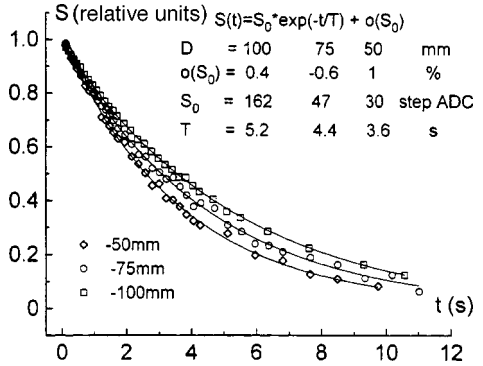

FIG. 2. Experimental and model data for 50, 75, and 100 mm in diameter cells. The signal amplitude is normalized to 1.

The experiment measuring the time T_1 was performed in a stable magnetic field with induction $B=15\ \mu$T and $B=30\ \mu$T, produced in a magnetically shielded solenoid. The light source was a specially constructed rf discharge lamp with a metal-containing branch pipe whose temperature was actively stabilized independently of the discharge regime in the working volume of the lamp. Equality of the intensities of the hyperfine components of the D_1 line for potassium is easily attained, because the Doppler broadening of the line is much greater than the hyperfine splitting. Optical fibers were used to transfer light from the source to the cell and from the cell to the photodetector. The required spectral component (D_1) was extracted with an interference light filter. Interruption of the light was accomplished with an electromechanical shutter. A dc inverting amplifier with current-to-voltage conversion ratio 41.6 V/μA was used to detect the signal. From the amplifier output the signal was fed into an 8-bit analog-to-digital converter, whose least-significant bit corresponded to 19.5 mV. The time interval between the readings was 0.42 ms, and the on and off switching times did not exceed 8 ms. In each dark pause an 8$\times$ oversampling of the signal was performed to improve the signal/noise ratio. A computer was used to control the experiment and for data acquisition and processing.

The characteristic form of the detected signal is presented in Fig. 1. The signal amplitude is given in units of the minimum conversion step and the time in seconds. The pump time was determined from the transient process after the dark pause expired: $T_{\text{pump}}\approx 0.1$ s with a detected photocurrent $I_{ph}=2\ \mu$A. Plots of the reconstructed dark relaxation curve are presented in Fig. 2. The amplitude of the signals is normalized to unity, and the time is given in seconds. The experimental curves can be fit well with a one-exponential function of the form

$$S(t)=S_0\ \exp(-t/\tau)+o(S_1). \tag{2}$$

The reliability of such a model is limited by the maximum dark pause duration, 12 s, realizable in experiment and by the signal/noise ratio. To record a relaxation curve in the form of two exponentials with the maximum possible difference of the exponents, the dark pause must be increased to 80 s, which requires a light reference channel for suppressing the noise associated with the drift of the light intensity.

The error in determining the quantities S_0, τ, and $o(S_1)$ does not exceed 8%. It is estimated from the reproducibility of the relaxation curve (Fig. 2) as a whole and is determined by the signal/noise ratio. The quantity $o(S_1)$ was found to be zero, to within the error with which it is determined, for each relaxation curve. This indicates that the single-exponential model is adequate.

For cells 50 and 75 mm in diameter containing a natural mixture of isotopes and for a cell 100 mm in diameter containing ^{41}K, the maximum times τ achieved are 3.6, 4.2, and 5.2 s, respectively. These are longest longitudinal relaxation times of the electronic polarization of the ground state of alkali metal atoms ever recorded. Previously the maximum longitudinal relaxation time $T_1\approx 1$ s was obtained in rubidium vapor using a deuterated coating.[8] No dependence of τ on the magnetic induction was observed to within the measurement error.

The variance of the times τ for cells of the same size was large. For cells with a diameter of 100 mm the measured times range from 5.2 to 0.7 s. Such a large variance of the times τ can be most naturally explained by domination of relaxation on paramagnetic

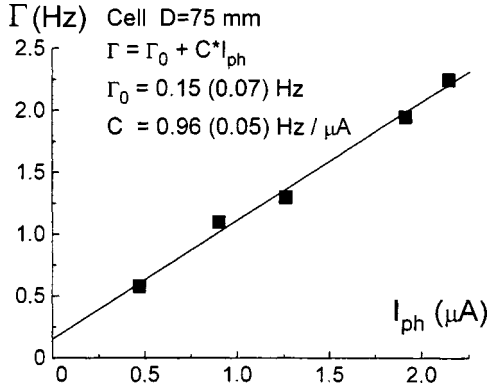

FIG. 3. Linewidth Γ versus the photocurrent I_{ph} for a cell with diameter $D=75$ mm.

centers with a large variance in the number of such centers in different cells of the same size. For example, for a relaxation time $T=1$ s an atom undergoes 5×10^3 collisions with the wall that do not lead to relaxation. Therefore the probability of an atom colliding with a paramagnetic center in this time should be much less than 1%. It is very difficult to obtain a quantitative estimate of the impurity concentration, since dangling bonds formed as a result of thermal destruction during the deposition of the coating must also be regarded as paramagnetic impurities.

The transverse relaxation time T_2 was measured in cells with the maximum values of τ. This time was determined by extrapolating the width Γ_0 of the rf–optic double resonance to zero light intensity and rf field amplitude (Fig. 3). Resonance was detected by synchronous detection on an individual outermost component of the spectrum ($F=2$, $m_f=2\Leftrightarrow F=2$, $m_f=1$) in a uniform stabilized magnetic field of 50 μT as the magnetic induction was varied.[2] At 24 °C it was found that $\Gamma_0=0.22$, 0.15, and 0.11 Hz, which corresponds to $T_2^{\Sigma}=1/2\pi\Gamma_0=0.72$, 1.1, and 1.4 s for cells with diameters of 50, 75, and 100 mm, respectively. The relative error in determining Γ_0 is large (50%) and the absolute error is very small (0.05 Hz). Therefore the recorded longitudinal relaxation times T_1 were much longer than the transverse relaxation times T_2.

We shall now analyze and estimate the contributions of the individual relaxation channels to the total relaxation rate for cells with the maximum relaxation times. The main relaxation mechanisms in cells with an antirelaxation coating are spin exchange between atoms (we denote the corresponding relaxation time by T^S), relaxation on a metal drop when an atom from the interior volume of the cell enters the metal-containing branch pipe through the diaphragm separating them (relaxation on a hole — T^H), and the interaction of atoms with the coating material (relaxation time T^C) and paramagnetic centers (time T').

For potassium vapor at room temperature and a spin exchange cross section $\sigma=3.6\times10^{-14}\,\mathrm{cm}^2$ the time T_2^S due to spin exchange is estimated to be 9.5 s.[10] Spin exchange does not affect T_1 in the case of observation of the electronic polarization.[8,11] We separate out the contribution to T_2 that is independent of spin exchange. Writing

$$1/T_2^{\Sigma}=1/T_2^C+1/T_2^S+1/T_2^H, \tag{3}$$

we obtain $1/T_2 = 1/T_2^{\Sigma} - 1/T_2^{S} = 0.78$, 1.3, and 1.6 s for cells with diameters 50, 75, and 100 mm, respectively. The time T_2 is observed to be directly proportional to the cell size, indicating that relaxation on the cell wall makes the main contribution to T_2. For relaxation on a hole and on a paramagnetic center $T_1^H = T_2^H$ and $T_1' = T_2'$. The large difference between τ and T_2 and the proportionality of T_2 to the cell size indicate that relaxation on the coating material makes the dominant contribution to the transverse relaxation, $T_2^{\Sigma} \approx T_2^C$.

In summary, we arrive at the conclusion that relaxation on paramagnetic centers makes the dominant contribution to the longitudinal relaxation of the electronic polarization of the ground state of potassium atoms in a cell with an antirelaxation coating on the walls, while transverse relaxation is due to the interaction of atoms with the diamagnetic coating material; this is presponsible for the large difference between the longitudinal and transverse relaxation times for relaxation on the coating, $T_1^C \gg T_2^C$.

We thank E. B. Aleksandrov for his constant interest in this work and V. S. Khromov and S. G. Przhibel'skiĭ for a fruitful discussion of the experimental results.

[1] M. V. Balabas, V. A. Bonch-Bruevich, and S. V. Provotorov, *Abstracts the 1st All-Union Seminar on Quantum Magnetometers* (S. I. Vavilov State Optics Institute, 1988), p. 55.
[2] E. B. Aleksandrov, V. A. Bonch-Bruevich, and N. N. Yakobson, Opt. Zh. **11**, 17 (1993).
[3] E. B. Aleksandrov, A. S. Pazgalev, and Zh. L. Rasson, Opt. Spectrosk. **82**, 14 (1997) [Opt. Spectrosc. **82**, 10 (1997)].
[4] E. B. Aleksandrov, M. V. Balabas, D. Budker *et al.*, Preprint NP-61-1998 2275 [in Russian], Russian Academy of Sciences, B. P. Konstantinov St. Petersburg Institute of Nuclear Physics (1998).
[5] D. Budker, V. Yashchuk, and M. Zolotorev, *International Conference on Atomic Physics 1998* (ICAP XVI), Windsor, Canada, 1998.
[6] E. B. Aleksandrov, in *Scientific Works on Optical Orientation of Atoms and Molecules* [in Russian] (A. F. Ioffe Physicotechnical Institute, Leningrad, 1087), p. 7.
[7] W. Franzen, Phys. Rev. **115**, 850 (1959).
[8] M. A. Bouchiat and J. Brossel, Phys. Rev. **147**, 41 (1966).
[9] H. Gibbs, Phys. Rev. **139**, 1374 (1965).
[10] E. B. Aleksandrov, M. V. Balabas, A. K. Vershovskiĭ *et al.*, Opt. Spektrosk. (1999), in press.
[11] A. Moretti and F. Strumia, Phys. Rev. A **3**, 349 (1971).

Translated by M. E. Alferieff

Structural ion-sound plasma turbulence as a self-similar random process

N. N. Skvortsova, N. K. Kharchev, and K. A. Sarksyan
Institute of General Physics, Russian Academy of Sciences, 117942 Moscow, Russia

(Submitted 24 May 1999; resubmitted 21 June 1999)
Pis'ma Zh. Éksp. Teor. Fiz. **70**, No. 3, 203–208 (10 August 1999)

It is shown that the experimentally investigated structural ion-sound plasma turbulence is a self-similar stationary random process. The self-similarity parameter is determined by two temporal laws: the nonrandom character of the appearance of nonlinear structures (nonlinear ion-sound solitons) in the plasma, and the nonlinear interaction between them. As the distance from the threshold of the ion-sound current instability increases, the self-similar random process approaches a Gaussian random process, but this limit has not been attained experimentally. The possibility of recording superlong time series of the fluctuations of the signal of the plasma process and processing of the time series by the R/S analysis method has made it possible to prove self-similarity of the plasma structural turbulence. © *1999 American Institute of Physics.* [S0021-3640(99)00915-9]

PACS numbers: 52.35.Ra, 52.35.Mw, 52.35.Dm

For many years now investigators in plasma physics have been drawn to the study of the nature of ion-sound plasma turbulence. Individual chapters in many books have been devoted to the theoretical description of this phenomenon. As an example, we mention two books, published more than 30 years apart.[1,2] Simultaneously with theoretical investigations, experimental investigations of ion-sound turbulence have also been conducted. The difficulty in performing experimental investigations lay in the need to measure many statistical parameters of turbulence (correlation, spectral, and so on) in order to compare with the theoretical description. For this reason, in the first experiments, as a rule, average values were determined and associated to the intensity of the turbulence. For example, a well-known estimate of the anomalous resistance of a plasma was made in Ref. 3. However, the statistical parameters of the turbulence could not be estimated because it was necessary to measure and analyze large sets of fluctuation data. For this reason, the study of a real structure of ion-sound turbulence was taken up only after the acquisition and analysis of experimental data were automated at the end of the 1980s. Investigations of ion-sound plasma turbulence based on analysis of the turbulence parameters of the plasma are now being conducted on several experimental installations.[4–6] For example, in Refs. 4 and 5 experimental analysis of ion-sound turbulence, whose source was ion-sound current instability, showed the turbulence to be strong and to contain structures that exist statistically stably in plasmas according to definite laws. Structures that are correlated in space and time accounted for up to 20–30% of the total energy of the turbulence. These

structures interact nonlinearly with one another by ''decaying'' and ''merging,'' forming a stable stationary frequency spectrum of turbulence. The observed structures have the nature of nonlinear ion-sound solitons, and it was suggested that the type of turbulence under study be termed structural ion-sound turbulence. Structural ion-sound turbulence exists in a wide range of values of the macroparameters of the plasma. In the experiment, as the instability threshold was approached, it was not possible to obtain a regime in which the ion-sound turbulence exists in the form of weak turbulence, and as the distance from the threshold of instability increased, it was impossible to obtain a regime with structureless ion-sound turbulence. The probability density function of the amplitudes of the fluctuation signals was different from the normal probability density function. The same difference from the normal probability density function was measured in Ref. 6. Thus the questions of the type of process developing in the observed plasma turbulence and of the statistical model corresponding to the recorded probability density functions remained open. The number of potentially possible models of distributions is extremely large. In practice, a relatively small number of models are in a special position — either because they possess desirable mathematical properties or because they describe some part of reality well or for both reasons at the same time.[7] The new experimental data enumerated above cannot be described by a normal (Gaussian) probability density function, and the existence of a long-lived component[4] in the autocorrelation function of the fluctuating quantities indicates a self-similar random process. It is important to note that the problem of determining the relation between the observed structural formations was not posed in previous experiments studying ion-sound turbulence because it was impossible to record superlong time series, without which it is impossible to determine long-range correlation functions reliably. Superlong time series can be observed under the conditions of our experiment on the TAU-1 setup,[8] and this has made it possible to compare the process under study with a self-similar process. The present letter is devoted to proving the existence of structural ion-sound turbulence in the form of a stationary self-similar random process.

Stationary stochastic processes for which the variance of the mean decreases as $n^{-\alpha}$ for any α between 0 and 2 were discovered by Kolmogorov in 1941.[9] These processes were termed self-similar. In the mid-1960s, Mandelbrot[10] introduced self-similar processes in certain statistical applications, and he substantiated their applications in hydrology and geophysics. Mandelbrot called the self-similarity parameter or the parameter of long-range correlation the Hurst[1)] parameter $H=1-\alpha/2$. This parameter can vary from 0 to 1 for stationary increments, $H=0.5$ corresponds to independence of the events in the observed process; $H>0.5$ corresponds to positive correlation, and $H<0.5$ corresponds to negative correlation. Self-similar processes $X(t)$ on the real axis are characterized by the following property: When the time scale of variation is changed by a factor $\alpha>0$, all finite-dimensional distributions change by the factor α^H. The study of the autocorrelation functions of self-similar processes is quite complicated, because the sum of small individual correlations approaches infinity, which results in infinite memory and makes it necessary to take into account the correlation between the distant past and the distant future. There exist several methods for investigating the Hurst parameter of a self-similar process: using correlograms, the spectral function of the variance as a function of time, the method of maximum likelihood, and Mandelbrot's method. In plasma physics Mandelbrot's method was used by Carreras *et al.*[11] to analyze turbulent oscillations of the edge turbulence in toroidal devices. This method is based on R/S analysis, where R/S is

the range of the accumulation process divided by the standard deviation of the incrementation process for a certain time interval $(s,s+t)$, where s is an arbitrary initial moment in time and the quantities R and S are defined below. To a first approximation, the points on a plot of the logarithm of the ratio R/S versus the logarithms of the time for a large number of different time intervals concentrate around a straight line with slope H. The algorithm for calculating the time dependence of R/S corresponds to the calculations of Ref. 11. For a discrete time series of a plasma fluctuation signal of length n, $X \equiv \{X_t : t = 1,2,\ldots,n\}$ with mean $\overline{X}(n)$ and variance $S^2(n)$, the ratio R/S is determined as

$$\frac{R(n)}{S(n)} = \frac{\max(0,W_1,W_2,\ldots,W_n) - \min(0,W_1,W_2,\ldots,W_n)}{\sqrt{S^2(n)}},$$

where $W_k = X_1 + X_2 + \ldots + X_k - k\overline{X}(n)$. Then the Hurst parameter is determined from the expectation value of this ratio $E[R(n)/S(n)]_{n\to\infty} \to \lambda n^H$.

As we have said, an experiment was performed on the TAU-1 setup. Argon plasma in the form of a cylindrical column 4 cm in diameter and 100 cm long was produced in a uniform magnetic field with intensity $\leqslant 800$ Oe by a steady low-energy electron beam with energy $E_b = 60$–150 eV and with argon pressure $p = (2$–$4) \times 10^{-4}$ torr. The plasma density was maintained at the level $n = (0.9$–$1.2) \times 10^{10}$ cm^{-3}. The electron temperature was $T_e = 5$–7 eV and the ion temperature was $T_i \approx 0.1 T_e$. An investigation of structural ion-sound turbulence was performed on this apparatus previously.[4,5] The characteristic frequencies in the plasma were related as follows: $\nu < \Omega_{ci} < \omega_{dr} < \omega_s \leqslant \omega_{Li} \ll \Omega_{ce}, \omega_{Le}$, where Ω_{ci} and Ω_{ce} are the ion and electron gyrofrequencies, ω_{Li} and ω_{Le} are the ion and electron plasma (Langmuir) frequencies, and ω_{dr} and ω_s are the drift and ion-sound frequencies. The characteristic frequency intervals (for $f = \omega/2\pi$) in which plasma oscillations occur in the experiment are: $f_{ci} = 10$–15 kHz; $f_{dr} = 20$–60 kHz; $f_s = 0.1$–$(4$–$5)$ MHz; $f_{Li} = 4$–5 MHz; $f_{ce}, f_{Li} = 1$–1.5 GHz. The amplitudes of the turbulent signals were measured with Langmuir probes, which were in a floating-potential regime for measuring fluctuations of the plasma potential. The autocorrelation coefficients and the Hurst parameter were determined from the recorded time series of the fluctuations of the potential: the length of one time series reached 128 thousand points, and the characteristic sample rate was 10 MHz. All data presented in the present letter were obtained with the stationary macroparameters of the plasma in the TAU-1 setup. A stationary regime in the plasma could be maintained for 3–5 h without changing the magnetic field, gas pressure, beam current, average plasma density, electron temperature, and so on. For this reason, the number of time series that could comprise an ensemble of the ion-sound turbulence process under study was essentially infinite.

Figure 1 shows the characteristic form of the time series of a stationary signal (a) of ion-sound structural plasma turbulence, recorded from an arbitrary time s in the TAU-1 plasma. The autocorrelation function of this signal, calculated in an arbitrary time interval within the given time series, is presented in two time scales in the same figure (b and c). Measurements were performed in the frequency range from 300 kHz (limited by low-frequency filter to remove drift oscillations) up to the Langmuir ion frequency (in the present case, about 5 MHz). This figure illustrates, in the first place, the ion-sound turbulent signal as a random burst (a) and, second, it indicates the presence of a long, weakly decaying temporal component in its autocorrelation function (b, c) (the noise signal in this measurement did not exceed 1%).

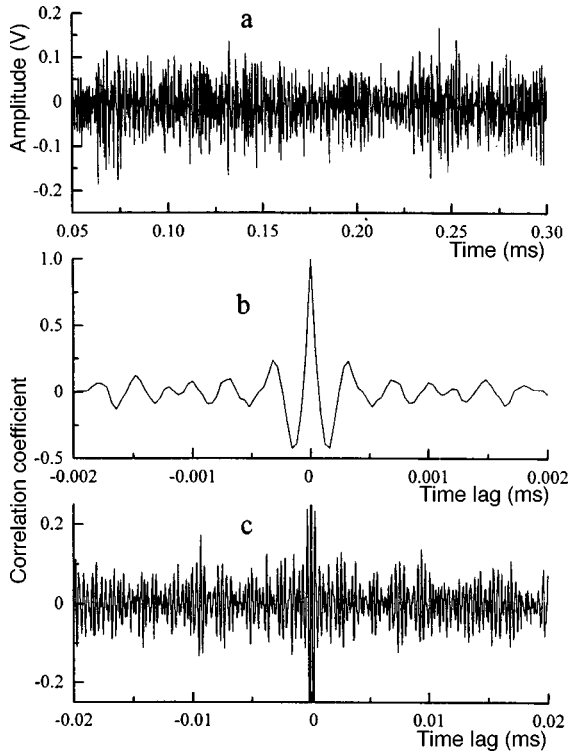

FIG. 1. Stationary temporal signal (a) of ion-sound structural plasma turbulence. Autocorrelation function of the signal in two time scales (b, c). $H=500$ G, $p=3\times10^{-4}$ torr, $U_b=120$ V, $I_b=200$ mA.

Figure 2 shows a plot of the logarithm of the ratio of the range R of ion-sound turbulent data to the standard deviation S of the incrementation process for the same data, versus the logarithm of the measurement time. The length of the data record is 64 000 points. The figure also shows two straight lines corresponding to R/S analysis for a regular process (Hurst parameter $H=1$) and a random process ($H=0.5$). The slope of the experimental R/S dependence is different in the three time intervals. The first time interval up to 10 μs corresponds to the average energy of the turbulent process reaching a stationary level,[5] i.e., the process in this interval is not stationary, so that a Hurst parameter cannot be defined. In the next time interval, from ~10 μs to ~200 μs (1 in the figure), the logarithm of R/S is directly proportional to the logarithm of the observation time, with a Hurst parameter ~0.6–0.7. This time interval corresponds to the characteristic lifetime of the structures, which was found in preceding experiments, or the characteristic memory time between nonrandom appearances of these structures.[5] From ~0.2 ms to $\sim1-2$ ms (2 in the figure) the logarithm of R/S is directly proportional to the observation time, with a Hurst parameter ~0.7–0.8. This time interval has also been determined previously;[5] it reflects the characteristic nonlinear interaction time between the structures. Among the set of measurements was a time series in which a sharp transition occurs between these intervals, which could be caused by an intense low-frequency regular drift wave that has not been inadequately attenuated in this measure-

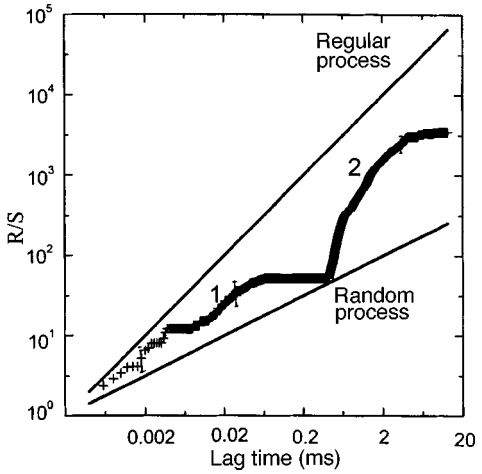

FIG. 2. R/S dependence for the fluctuation signal. The time series contains 64 000 points. $H=500$ G, $p=3\times10^{-4}$ torr, $U_b=120$ V, $I_b=50$ mA.

ment. Thus the stationary structural ion-sound turbulent process observed in the process observed in the plasma is not random, since the Hurst parameter exceeds 0.5 in the entire observation interval. In addition, this process can be said to be self-similar. The self-similarity parameter is determined by two time dependences: the nonrandom appearance of structures in turbulence, and the nonlinear interaction between these structures. The self-similarity parameter is $\alpha=0.6$–0.8 for observation time intervals such that the law describing the nonrandom appearance of structures is the governing factor. For long observation intervals, when the appearance of structures can be regarded as a random event because of the multiplicity of such events, the self-similarity parameter decreases to $\alpha=0.4$, and only the law of their nonlinear interaction makes it possible to preserve a memory of the self-similar process.

Figure 3 shows the dependences obtained by R/S analysis for ion-sound turbulent signals for various electron beam currents in the TAU-1 plasma. The higher beam current, the larger the distortion of the electron distribution is and, as noted above, the farther away the excitation of ion-sound structural turbulence is from the instability threshold. The slope of the experimental R/S dependence is different for different beam currents: As the current increases (correspondingly, as the distance from the instability threshold increases), the R/S experimental plot approaches a direct random process. However, in the experiment we were not able to find a regime where the ion-sound structural turbulence could be described not by a self-similar stochastic process but rather by a random stochastic process.

The present experimental study has shown that the structural ion-sound plasma turbulence is a self-similar stationary stochastic process. The self-similarity parameter is determined by two temporal laws: the random character of the appearance of nonlinear ion-sound solitons in the plasma and the nonlinear interaction between them. As the distance from the threshold of ion-sound current instability increases, the random process approaches a Gaussian random process, but this limit could not be reached experimen-

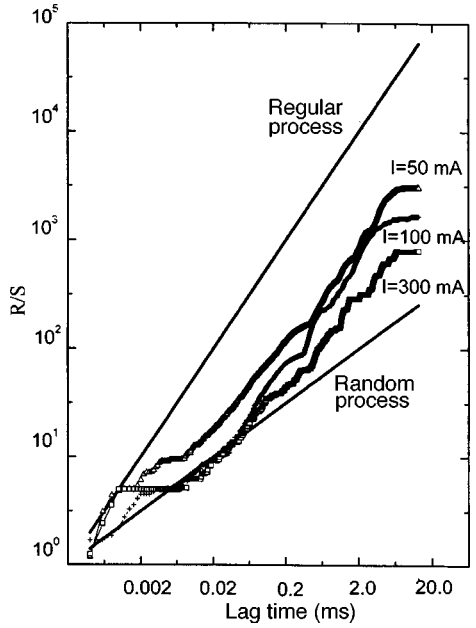

FIG. 3. R/S dependences for fluctuation signals with different cathode emission currents. The length of one time series is 64 000 points, with an averaging over five time series. $H=500$ G, $p=3\times10^{-4}$ torr, $U_b=120$ V.

tally. It should be noted that the ion-sound structural turbulence developing in a stationary plasma can serve as an object for model physical investigations studying the properties of random probabilistic processes with a long memory. The question of the physical mechanism giving rise to the memory of the self-similar process in ion-sound structural turbulence can only be answered tentatively at present. It is possible that the self-similar characteristics of the processes recorded are due to coupling of the ion-sound vibrations with drift oscillations of magnetized plasma, whose intensities are much higher than the intensities of ion-sound vibrations and whose frequencies lie in the range 10–80 kHz. The influence of the form of the spectrum of such drift oscillations on the probability density function of the turbulence under study was ascertained previously,[4] and the characteristic times of such oscillations are tens and hundreds of times longer than the characteristic times of ion-sound vibrations. It is obvious that the latter circumstance requires a corresponding increase in the length of the time series for performing investigations. This problem has now been posed and the solution will be found in the near future.

We thank G. N. Batanov (IOFAN, Moscow) and B. F. van Milligen (CIEMAT, Madrid) for participating in a discussion of the experimental results, and A. E. Petrov for assisting in the experiment.

This work was supported by the Russian Fund for Fundamental Research (Grant 98-02-16345).

[1)]In honor of the scientist H. E. Hurst, who in 1951 empirically described the existence of long-time temporal correlations between water levels in Nile river floods (an example of a self-similar process in hydrology).

[1] B. B. Kadomtsev, *Plasma Turbulence* (Nauka, Moscow, 1963).
[2] A. S. Kengisep, *Introduction to Nonlinear Plasma Physics* (Moscow Physicotechnical Institute Press, Moscow, 1996).
[3] M. B. Babykin, P. P. Gavrin, E. K. Savoĭskiĭ *et al.*, Zh. Éksp. Teor. Fiz. **43**, 411 (1962) [Sov. Phys. JETP **16**, 295 (1962)].
[4] A. A. Rukhadze, K. A. Sarksian, and N. N. Skvortsova, J. Phys. IV **5**, C653 (1995).
[5] K. A. Sarksyan, N. N. Skvortsova, N. K. Kharchev, and B. F. Milligen, Fiz. Plazmy, No. 4 (1999), in press.
[6] A. H. Nielson, H. L. Pesceli, and J. J. Rassmusen, Phys. Plasmas **3**, 1530 (1996).
[7] N. Hastings and B. Peacock, *Statistical Distributions* (Russian translation, Statistika, Moscow, 1980).
[8] G. M. Batanov, L. M. Kovrizhnykh, L. V. Kolik *et al.*, Trudy Fiz. Inst. Akad. Nauk SSSR **160**, 122 (1985).
[9] A. N. Kolmogorov, Dokl. Akad. Nauk SSSR **30**, 299 (1941).
[10] F. Hampel *et al.*, *Robust Statistics: The Approach Based on Influence Functions* (Wiley, New York, 1986) [Russian translation, Mir, Moscow, 1989].
[11] B. A. Carreras, B. van Milligen, M. A. Pedrosa *et al.*, Phys. Rev. Lett. **80**, 4438 (1998).

Translated by M. E. Alferieff

Current fluctuations in an ideally conducting contact

G. B. Lesovik

L. D. Landau Institute of Theoretical Physics, Russian Academy of Sciences, 117940 Moscow, Russia

(Submitted 10 June 1999)
Pis'ma Zh. Éksp. Teor. Fiz. **70**, No. 3, 209–215 (10 August 1999)

It is shown that the shot noise at finite frequency in an ideally conducting contact is finite. The complete formula for the current correlation function at finite frequency is presented for a quantum conductor, where the electron transport can be adequately described in a model of noninteracting electrons using a scattering matrix. It is indicated that the description of electron transport in Landauer's approach (using a scattering matrix) is equivalent to a description using the Keldysh technique. Noise in an ideally conducting contact is calculated using the general formula. It is shown that in such a contact the spectral density of the noise has a singularity at the ''Josephson'' frequency $\omega = eV/\hbar$, set by the voltage. © *1999 American Institute of Physics.* [S0021-3640(99)01015-4]

PACS numbers: 73.40.Cg, 73.50.Td

In an ideal conductor with electron transport probability equal to 1 ($T=1$) the low-frequency shot noise is suppressed, as has been shown theoretically, using a quantum-mechanical description in terms of the scattering matrix, for a quantum point contact,[1–4] and even earlier, using a quasiclassical description, for ballistic point contacts,[5,6] and as has been confirmed experimentally[7,8] for quantum point contacts. The same phenomenon has been predicted theoretically[9] and confirmed experimentally[10,11] for conductors in the fractional quantum Hall effect regime. Nonetheless, at finite frequency the noise remains finite even in an ideal quantum conductor, and it is this effect that is discussed in the present letter.

In a conductor where electron transport can be adequately described in a model of noninteracting electrons using the scattering matrix, the spectral density of the shot noise at zero frequency is given by[1–4]

$$S(0)=2e^3V/h\sum_n T_n(1-T_n), \tag{1}$$

where V is the pulling voltage, e is the electron charge, T_n is the transmittance in the intrinsic channel n, h is Planck's constant, and the temperature θ is assumed to be zero. From this expression it follows directly that shot noise is completely suppressed for $T=1$.

The behavior of shot noise with $T=1$ at low frequencies has been discussed qualitatively many times, and we shall repeat only briefly the corresponding arguments. The first condition for the existence of shot noise is discreteness of the electron charge. Indeed, if the charge is set equal to zero at a fixed current, then the noise vanishes, since $S(0)/I \propto e$.

At zero temperature and finite voltage the only reason for fluctuations of the current (besides the already mentioned discreteness of the charge) transported by noninteracting electrons is the probabilisitc nature of tunneling through a barrier (or scattering by impurities), more accurately, the probabilistic nature of the measurement process in which the electrons are detected either in a left-hand reservoir (electrons which have passed through a barrier) or in the right-hand reservoir (electrons which have been reflected from a barrier). For this reason, if the transmittance T becomes 1, this reason for fluctuations disappears. The absence of low-frequency fluctuations due to the irregularity of the electron injection from a reservoir is due to the fact that electrons obey Fermi statistics.

We shall now discuss noise at a finite frequency. To understand why noise is finite in this case, we must refine the arguments presented above. Noise at zero frequency could be due to fluctuations of the charge transported through the conductor in time t as follows:[12] $\lim_{t\to\infty}\langle(\delta Q_t)^2\rangle/t = S(0)$. For this reason, if fluctuations of the transported charge grow more slowly than t, noise at zero frequency is zero. This is what happens for a conductor with $T=1$. At the same time, even in an ideal conductor at zero temperature and finite voltage charge fluctuations are not zero:

$$\langle(\delta Q_t)^2\rangle = 2e^2/\pi^2 \ln t\Omega + e^2/4\pi^2[(eV/2\epsilon_F)^2 - \sin^2(eVt/2\hbar)(\hbar/\epsilon_F t)^2],$$

where Ω is a cutoff frequency and ϵ_F is the Fermi energy. The first term in this expression is related with the existence of zero-point oscillations[13] and, in turn, with the fact that the Fermi correlations cannot completely suppress fluctuations and fix the position of electrons relative to one another. The second term depends on the applied voltage and is (conventionally speaking) a result of fluctuations which is due to the transitions of left-hand electrons into right-hand electrons and vice versa.

The finiteness of the noise at finite frequency can now be argued as follows. Although for $T=1$ a wave packet leaving one reservoir completely passes into the other reservoir and the probability of detecting an electron there in time approaches 1, the charge transport process is nonetheless not completely uniform in time, and oscillations occur at the frequency of the applied voltage. Specifically, for a symmetrized current–current correlation function the main (at long times $t \gg \hbar/eV$) contribution to the oscillatory dependence has the form

$$\langle I(0)I(t)\rangle = \frac{e^2}{\pi^2}\frac{(eV)^3}{8\epsilon_F^2\hbar t}\sin(eVt/\hbar).$$

Technically, the existence of such fluctuations is due to the fact that the matrix element of the current operator between two plane waves with wave vectors having opposite signs,

$$\langle \exp(ik_1x)|\hat{I}|\exp(-ik_2x)\rangle = \frac{ie\hbar}{2m}[-ik_1+ik_2]\exp(-[ik_1+ik_2]x),$$

is nonzero if the absolute magnitudes of the vectors are not equal to one another. This gives rise to transitions between ''left-hand'' and ''right-hand'' electrons. At zero frequency such transitions do not contribute to single-particle quantities, such as the conductivity, but they do appear in the two-particle correlation functions, specifically, the current correlation function.

We shall now calculate the total current correlation function whence follow the expressions presented above. The description of transport in a nonequilibrium system can be given most systematically using Keldysh's approach.[15] In this approach to transport, just as with the use of a transport equation, the disequilibrium caused by the presence of an electromotive force in the circuit is described by prescribing boundary conditions on the ''Keldysh'' or ''$-+$'' Green's function $G_{-+}(x_1,x_2)=i\langle\Psi^{\dagger}(x_2)\Psi(x_1)\rangle$ at the edges:

$$G_{-+}(x_1,x_2)|_{x_n=X_\beta}=G^{eq}_{-+}(X_\beta,X_\beta). \tag{2}$$

Here $G^{eq}_{-+}(X_\beta,X_\beta)$ is the equilibrium Green's function at the edges. It can be shown that for noninteracting system of electrons this approach is completely equivalent to the approach initiated by Landauer and others.[16] In Landauer's approach it is assumed that the electrons leaving different reservoirs are uncorrelated. The occupation numbers for the corresponding states are determined by the chemical potential and the temperature in the corresponding reservoir. Electron scattering by a static potential inside the conductor joining the reservoirs can be described purely quantum mechanically using wave functions which are exact solutions of the scattering problem.

What we have said above can be conveniently described in the second-quantization formalism. The electronic ψ operators are written in a basis of Lippman–Schwinger scattering states, $\hat{\Psi}(r)=\Sigma_{\alpha,\epsilon,n}\hat{c}_{\alpha,\epsilon,n}\varphi_{\alpha,\epsilon,n}(r)$, which have (in the reservoir β) the asymptotic form

$$\varphi_{\alpha,\beta,\epsilon,n}(r)=\frac{\exp(-ik_{nn}|x|)}{\sqrt{v_{nn}}}\chi_{\beta,\epsilon,n,-}(y)\,\delta_{\beta,\alpha} + \sum_m S_{\alpha,\beta,\epsilon,n,m}\frac{\exp(+ik_{nm}|x|)}{\sqrt{v_{nm}}}\chi_{\beta,\epsilon,m,+}(y). \tag{3}$$

The creation operators $\hat{c}^{\dagger}_{\alpha,\epsilon,n}$ create states of electrons emitted from reservoir α with energy E in the transverse channel n. The indices $\pm$ in the functions χ describing motion along the y axis (for simplicity, the conductor is assumed to be two-dimensional) indicate motion in the direction of the x axis along the conductor. Such indices must be introduced in the presence of a magnetic field. The wave vectors are chosen to be positive, and $\hbar^2k^2_{nm}+\epsilon_m=\epsilon$, where ϵ_m is the quantization energy in the mth transverse mode (channel).

The density matrix of the system can be written, in accordance with the assumption that the reservoirs are uncorrelated, as a direct product of independent factors describing each reservoir:

$$\hat{\rho}=\Pi_\alpha\exp\left[-\sum_{\epsilon,n}\hat{c}^{\dagger}_{\alpha,\epsilon,n}\hat{c}_{\alpha,\epsilon,n}(\epsilon-\mu_\alpha)\right]/\theta_\alpha, \tag{4}$$

where μ_α and θ_α are the chemical potential and temperature in reservoir α.

Describing a conductor whose transverse cross section contains n channels and a reservoir with N channels, we obtain that the nonequilibrium part of the distribution function, or the Keldysh Green's function, will have a small correction, if the ratio n/N is small, since in this case the fraction of nonequilibrium electrons arriving in each reservoir from other reservoirs will be small to the extent of the inequality $n/N \ll 1$. Thus the ansatz (3)–(4) used in the Landauer approach (the approach using a scattering matrix) satisfies, to a high degree of accuracy, the boundary conditions on the Keldysh function (2) (see also Ref. 17). The number of channels in the reservoir must be determined at a distance of the order of the inelastic mean free path L_{inel} from the conductor, where we assume $L_{\text{inel}} \gg L$ and L is a characteristic dimension of the conductor. For a dirty conductor with a constant cross section, the ratio of the number of open channels to the total number of channels, $n/N \sim l/L \ll 1$, where l is the elastic mean free path, plays the role of the small parameter $n/N \ll 1$.

Now using Eqs. (3)–(4) to calculate the correlation function of the total currents in the reservoirs β' and β in the sections x_1 and x_2 at finite frequency,

$$\langle\langle I_{-\omega}(\beta',x_1) I_\omega(\beta,x_2)\rangle\rangle = \int dt \exp(i\omega t) \mathrm{Tr}\{\hat{\rho}\hat{I}_{\beta'}(x_1) e^{i\hat{H}t} \hat{I}_\beta(x_2) e^{-i\hat{H}t}\} - \langle \hat{I}_{\beta'}(x_1)\rangle \langle \hat{I}_\beta(x_2)\rangle \tag{5}$$

(here $\hat{H} = \Sigma_{\alpha,\epsilon,n} \hat{c}^\dagger_{\alpha,\epsilon,n} \hat{c}_{\alpha,\epsilon,n} \epsilon$), we obtain the expression

$$\langle\langle I_{-\omega}(\beta',x_1) I_\omega(\beta,x_2)\rangle\rangle = 2e^2 \sum_{\alpha' n' \alpha n} \int \frac{d\epsilon}{h} n_{\alpha'}(\epsilon')[1-n_\alpha(\epsilon)] \times J^{\beta'\alpha'\epsilon'n'}_{\beta'\alpha\epsilon n}(x_1) J^{\beta\alpha\epsilon n}_{\beta\alpha'\epsilon',n'}(x_2). \tag{6}$$

Here (and in the formulas below) $\epsilon' = \epsilon + \hbar\omega$, $\epsilon' = \epsilon(k')$, and Zeeman splitting is neglected. The index β enumerates the reservoirs where the current is measured and the index α enumerates the reservoirs from which electrons are injected. The current matrix elements can be expressed in terms of the scattering matrix elements $S_{\alpha,\beta,\epsilon,n,m}$ as follows:

$$J^{\alpha',\epsilon',n'}_{\alpha,\epsilon,n} = \sum_{m',m} S^*_{\alpha',\beta,\epsilon',n,m} S_{\alpha,\beta,\epsilon,n,m} \left(\frac{e\hbar(k'_{n',m'} + k_{n,m})}{2M} \langle m'\epsilon'_+ | m\epsilon_+\rangle - \frac{e^2}{Mc} \langle m'\epsilon'_+ | A_x(y) | m\epsilon_+\rangle \right) \frac{\exp(-i(k'_{n',m'} - k_{n,m})x)}{\sqrt{v'_{n'm'} v_{nm}}} + \left(\frac{e\hbar(-k'_{n,n} - k_{n,n})}{2M} \langle n\epsilon'_- | n\epsilon_-\rangle - \frac{e^2}{Mc} \langle n\epsilon'_- | A_x(y) | n\epsilon_-\rangle \right) \frac{\exp(i(k'_{n,n} - k_{n,n})x)}{v_{nn}} \delta_{R,\alpha'} \delta_{R,\alpha}$$

$$+S^{*}_{\alpha',\beta,\epsilon',n',m'}\left(\frac{e\hbar(k'_{n',m'}-k_{n,n})}{2M}\langle m'\epsilon'_{+}|n\epsilon_{-}\rangle\right.$$

$$\left.-\frac{e^{2}}{Mc}\langle m'\epsilon'_{+}|A_{x}(y)|n\epsilon_{-}\rangle\right)\frac{\exp(-i(k'_{n',m'}+k_{n,n})x)}{\sqrt{v'_{n'm'}v_{nn}}}\delta_{R,\alpha}$$

$$+S_{\alpha,\beta,\epsilon,n,m}\left(\frac{e\hbar(-k'_{n',n'}+k_{n,m})}{2M}\langle n'\epsilon'_{-}|m\epsilon_{+}\rangle\right.$$

$$\left.-\frac{e^{2}}{Mc}\langle n'\epsilon'_{-}|A_{x}(y)|m\epsilon_{+}\rangle\right)\frac{\exp(i(k'_{n',n'}+k_{n,m})x)}{\sqrt{v'_{n'n'}v_{nm}}}\delta_{R,\alpha'}; \qquad (7)$$

here $v=\partial\epsilon(k)/\hbar\partial k$. The last two terms in the expressions presented above are zero at zero frequency, and these are the terms that give finite noise at finite frequency in an ideal conductor, where the scattering matrix has the trivial form (for two reservoirs denoted by the indices L and R) $|S_{\alpha,\beta,\epsilon,n,m}|^{2}=\delta_{L,\alpha}\delta_{R,\beta}\delta_{n,m}+\delta_{R,\alpha}\delta_{L,\beta}\delta_{n,m}$.

In the presence of a magnetic field the overlap of the transverse wave functions is $\langle n'\epsilon'_{+}|m\epsilon_{-}\rangle=\int dy\chi^{*}_{\epsilon',n',+}(y)\chi_{\epsilon,n,-}(y)$, and the matrix element $\langle n'\epsilon'_{+}|A_{x}(y)|m\epsilon_{-}\rangle=\int dy\chi^{*}_{\epsilon',n',+}(y)A(y)\chi_{\epsilon,n,-}(y)$ depends on the energies and the signs of the k vectors $(\pm)$. The contributions of interest to us, which are due to the nonlinearity of the spectrum, contain matrix elements of the transverse wave functions describing the edge states on two different edges. If the width of the conductor is much greater than the effective magnetic length, $d\gg\tilde{a}_{H}$, then noise in an ideal conductor at finite frequency is exponentially suppressed. As an illustration, we present an expression for the overlapping of the zeroth-order transverse wave functions in the presence of a magnetic field for a conducting channel formed by a square confining potential $U(y)=m\Omega_{0}^{2}y^{2}/2$:

$$\langle k',0|k,0\rangle=\exp\left(-\frac{\hbar(k'-k)^{2}\omega_{H}^{2}}{4m\Omega^{3}}\right),$$

$$\langle k',0|A(y)|k,0\rangle=-\frac{\hbar(k'+k)e\omega_{H}}{|e|2m\Omega^{2}}\langle k',0|k,0\rangle.$$

For convenience the wave vectors in these expressions, in contrast to all other formulas in this letter, are determined with the sign. Here $\Omega^{2}=\Omega_{0}^{2}+\omega_{H}^{2}$,

$$\omega_{H}=|e|H/mc,\quad \epsilon(k)=\frac{\Omega_{0}^{2}\hbar^{2}k^{2}}{\Omega^{2}2m}+(n+1/2)\hbar\Omega=\frac{\Omega^{2}mv^{2}}{\Omega_{0}^{2}2}+(n+1/2)\hbar\Omega.$$

If the form of the confining potential is more complicated, for example, because of Coulomb effects,[18] the expressions change accordingly.

Without a magnetic field $\langle m'|m\rangle=\delta_{m',m}$. In the single-channel case without a magnetic field we obtain

$$\langle\langle \hat{I}_{-\omega}(x_1)\hat{I}_{\omega}(x_2)\rangle\rangle=\frac{2e^2\hbar^2}{(2m)^2}\int\frac{d\epsilon}{v_{\epsilon'}v_{\epsilon}h}\{n_L(\epsilon')(1-n_L(\epsilon))(k+k')^2T_{\epsilon'}T_{\epsilon}e^{i(k-k')(x_1-x_2)}$$

$$+n_L(\epsilon')(1-n_R(\epsilon))[(k+k')^2T_{\epsilon'}(1-T_{\epsilon})e^{i(k-k')(x_1-x_2)}$$

$$+(k'^2-k^2)T_{\epsilon'}e^{-ik'(x_1-x_2)}(r_{\epsilon}e^{ik(x_1+x_2)}+r_{\epsilon}^{*}e^{-ik(x_1+x_2)})$$

$$+(k'-k)^2T_{\epsilon'}e^{-i(k+k')(x_1-x_2)}]n_R(\epsilon')(1-n_L(\epsilon))[(k+k')^2T_{\epsilon}$$

$$\times(1-T_{\epsilon'})e^{i(k-k')(x_1-x_2)}+(k^2-k'^2)T_{\epsilon}e^{ik(x_1-x_2)}(r_{\epsilon'}e^{ik'(x_1+x_2)}$$

$$+r_{\epsilon'}^{*}e^{-ik'(x_1+x_2)})+(k'-k)^2T_{\epsilon}e^{i(k+k')(x_1-x_2)}]n_R(\epsilon')(1-n_R(\epsilon))$$

$$\times[(k+k')^2e^{-i(k-k')(x_1-x_2)}+(k+k')^2R_{\epsilon'}R_{\epsilon}e^{i(k-k')(x_1-x_2)}$$

$$-(k+k')^2[r_{\epsilon'}^{*}r_{\epsilon}e^{i(k-k')(x_1+x_2)}+r_{\epsilon}^{*}r_{\epsilon'}e^{-i(k-k')(x_1+x_2)}]$$

$$+(k^2-k'^2)[r_{\epsilon}^{*}e^{-i(k-k')x_1-i(k+k')x_2}-r_{\epsilon'}e^{i(k+k')x_2}$$

$$+r_{\epsilon'}^{*}e^{i(k-k')x_2}e^{-i(k+k')x_1}-r_{\epsilon}e^{i(k+k')x_1}]+(k^2-k'^2)$$

$$\times[r_{\epsilon'}^{*}R_{\epsilon}e^{i(k-k')x_1-i(k+k')x_2}-r_{\epsilon}R_{\epsilon'}e^{i(k+k')x_2}$$

$$-R_{\epsilon'}r_{\epsilon}^{*}e^{-i(k-k')x_2-i(k+k')x_1}-R_{\epsilon}r_{\epsilon'}e^{i(k+k')x_1}]$$

$$-(k-k')^2[r_{\epsilon'}^{*}e^{-i(k+k')x_1}-r_{\epsilon}e^{i(k+k')x_1}]$$

$$\times[r_{\epsilon}^{*}e^{-i(k+k')x_2}-r_{\epsilon'}e^{i(k+k')x_2}]]\}, \tag{8}$$

where $R_{\epsilon}=|r_{\epsilon}|^2=1-T_{\epsilon}$. From this expression we obtain the estimate $(1-T)\ll(\hbar\omega)^2/\epsilon_F^2$ for values of the transmittance such that the ''unusual'' contributions are substantial at finite frequency.

We shall now write out an expression for the noise in a quantum point contact, if one channel is completely opened and the wave functions can be represented in the quasiclassical form

$$\langle\langle \hat{I}_{-\omega}(x_1)\hat{I}_{\omega}(x_2)\rangle\rangle = \frac{2e^2\hbar^2}{(2m)^2}\int \frac{d\epsilon}{h}\left\{ \frac{4\omega^2}{(v_1'+v_1)(v_2'+v_2)\sqrt{v_1'v_2'v_1v_2}} \right.$$
$$\times\left\{ n_L(\epsilon')(1-n_R(\epsilon))\exp\left(-i\int_{x_1}^{x_2}(k'(x)+k(x))dx \right) \right.$$
$$\left.+ n_R(\epsilon')(1-n_L(\epsilon))\exp\left(i\int_{x_1}^{x_2}(k'(x)+k(x))dx \right)\right\}$$
$$+\frac{(k_1'+k_1)(k_2'+k_2)}{\sqrt{v_1'v_2'v_1v_2}}\left\{ n_L(\epsilon')(1-n_L(\epsilon))\left(\exp\left(-i\int_{x_1}^{x_2}(k'(x)\right.\right.\right.$$
$$\left.\left.\left.-k(x))dx\right) n_R(\epsilon')(1-n_R(\epsilon))\exp\left(i\int_{x_1}^{x_2}(k'(x)-k(x))dx \right)\right\}\right\}. \quad (9)$$

It is evident from this expression that the fluctuations are maximum near a constriction, where the kinetic energy of the longitudinal motion is minimum, and they decrease into the reservoir. This means that electron motion near the constriction makes the main contribution to the fluctuations.

The frequency dependence has a singularity at $\hbar\omega = eV$ similar to that studied previously in a normal contact with scattering[19,20] and in a contact between Luttinger liquids.[21] For a symmetrized correlation function at voltages much lower than the minimum Fermi energy, the spectral density has the form

$$\left\langle\left\langle \frac{1}{2}[\hat{I}_{-\omega}(x)\hat{I}_{\omega}(x)+\hat{I}_{\omega}(x)\hat{I}_{-\omega}(x)]\right\rangle\right\rangle = \frac{2e^2}{h}\left(\hbar\omega + \frac{(\hbar\omega)^2}{16\epsilon_F^2(x)}f(\hbar\omega)\right), \quad (10)$$

where $f(\hbar\omega)=eV$ for frequencies $\hbar\omega<eV$ and $f(\hbar\omega)=\hbar\omega$ for $\hbar\omega>eV$. Such a singularity can be observed in direct measurements[22] and in an experiment with an additional external frequency; see Refs. 20 and 23.

In experiments where the noise is measured at a finite frequency, if the measurements are performed using a resonant loop with high Q, only ''positive frequencies'' make a contribution, and the excess noise is $e^2(\hbar\omega)^2/(h8\epsilon_F^2)^{-1}(eV-\hbar\omega)$.[24]

In closing, we note that in previously presented expressions for noise at finite frequency[1,19] the terms making a finite contribution in an ideal conductor were omitted; the main motive, for example, for the present author, was that the corresponding terms are small. However, the substantial advances made in recent years in measuring noise and in preparing new mesoscopic conductors hold forth the hope either that it will be possible to measure even weaker noise in existing structures or that conductors with a very low Fermi energy and high mobility, where the effect is large, will become available.

I thank D. C. Glattli, M. Reznikov, D. Prober, and especially H. Bouchiat for helpful and stimulating discussions of the possibility of observing this effect experimentally. This letter is due to H. Bouchiat's interest and enthusiasm.

[1] G. B. Lesovik, JETP Lett. **49**, 592 (1989).
[2] B. Yurke and G. P. Kochanski, Phys. Rev. B **41**, 8184 (1990).
[3] M. Buttiker, Phys. Rev. Lett. **65**, 2901 (1990).
[4] Th. Martin and R. Landauer, Phys. Rev. B **45**, 1742 (1992).
[5] I. O. Kulik and A. N. Omel'yanchuk, Fiz. Nizk. Temp. **10**, 305 (1984) [Sov. J. Low Temp. Phys. **10**, 158 (1984)].
[6] V. A. Khlus, Zh. Éksp. Teor. Fiz. **93**, 2179 (1987) [Sov. Phys. JETP **66**, 1243 (1987)].
[7] M. Reznikov, M. Heiblum, H. Shtrikman, and D. Mahalu, Phys. Rev. Lett. **75**, 3340 (1995).
[8] A. Kumar, L. Saminadayar, D. C. Glattli *et al.*, Phys. Rev. Lett. **76**, 2778 (1996).
[9] C. L. Kane and M. P. A. Fisher, Phys. Rev. Lett. **72**, 724 (1994); see also Ref. 14.
[10] L. Saminadayar, D. C. Glattli, Y. Jin, and B. Etienne, Phys. Rev. Lett. **79**, 2526 (1997).
[11] de-Picciotto, M. Reznikov, M. Heiblum *et al.*, Nature **389**, 162 (1997).
[12] W. Schottky, Ann. Phys. (Leipzig) **57**, 16432 (1918).
[13] L. S. Levitov and G. B. Lesovik, JETP Lett. **58**, 230 (1993).
[14] G. B. Lesovik and R. Loosen, Z. Phys. B: Condens. Matter **91**, 531 (1993).
[15] L. V. Keldysh, Zh. Éksp. Teor. Fiz. **47**, 1515 (1964) [Sov. Phys. JETP **20**, 1018 (1965)].
[16] R. Landauer, IBM J. Res. Dev. **1**, 223 (1957); Philos. Mag. **21**, 863 (1970); P. W. Anderson, D. J. Thouless, E. Abrahams, and D. S. Fisher, Phys. Rev. B **22**, 3519 (1980); D. S. Fisher and P. A. Lee, Phys. Rev. B **23**, 6851 (1981); M. Buttiker, Phys. Rev. Lett. **57**, 1761 (1986); Y. Imry, in *Directions in Condensed Matter Physics*, edited by G. Grinstein and G. Mazenko (World Scientific Press, Singapore, 1986), p. 101.
[17] I. B. Levinson, Zh. Éksp. Teor. Fiz. **95**, 2175 (1989) [Sov. Phys. JETP **68**, 1257 (1989)].
[18] D. B. Chklovskii, B. I. Shklovskii, and L. I. Glazman, Phys. Rev. B **46**, 4026 (1993).
[19] S.-R. Eric Yang, Solid State Commun. **81**, 375 (1992).
[20] G. B. Lesovik and L. Levitov, Phys. Rev. Lett. **72**, 538 (1994).
[21] C. de C. Chamon, D. E. Freed, and X. G. Wen, Phys. Rev. B **53**, 4033 (1996).
[22] R. J. Schoelkopf, B. J. Burke, A. A. Kozhevnikov *et al.*, Phys. Rev. Lett. **78**, 3370 (1997).
[23] R. J. Schoelkopf, A. A. Kozhevnikov, D. E. Prober, and M. J. Rooks, Phys. Rev. Lett. **80**, 2437 (1998).
[24] G. B. Lesovik and R. Loosen, JETP Lett. **65**, 295 (1997).

Translated by M. E. Alferieff

Optical properties of excitons in CdS semiconductor–insulator quantum wires

S. A. Gavrilov
Moscow Institute of Electronics (Technical University), 103498 Moscow, Russia

V. V. Gusev,*) V. S. Dneprovskiĭ, E. A. Zhukov, A. N. Syrnikov, and I. V. Yaminskiĭ
M. V. Lomonosov Moscow State University, 119899 Moscow, Russia

E. A. Muljarov
Institute of General Physics, Russian Academy of Sciences, 117942 Moscow, Russia

(Submitted 17 June 1999)
Pis'ma Zh. Éksp. Teor. Fiz. **70**, No. 3, 216–220 (10 August 1999)

The characteristic features of the luminescence spectra of CdS semiconductor nanocrystals, crystallized in hollow channels in a dielectric template, are explained in terms of excitonic transitions in semiconductor–insulator quantum wires. The excitonic transition energies agree with the values calculated taking into account the effects of size quantization and the ''dielectric enhancement of excitons'' — the large increase in the electron–hole attraction as a result of the difference between the permittivities of the semiconductor and insulator. The theoretically computed binding energies of excitons in CdS quantum wires with a diameter of 10 nm reach 170 meV. It is shown that the excitonic transition energy is constant for a wide range of wire diameters. © *1999 American Institute of Physics.*
[S0021-3640(99)01115-9]

PACS numbers: 78.66.Hf, 78.55.Et, 71.35.Cc

In semiconductor quantum wires (QWs) — nanostructures in which free carrier motion is possible only in one direction, the electron–hole Coulomb attraction is intensified and excitonic transitions dominate in the absorption and luminescence spectra.[1,2] For QWs with semiconductor barriers the exciton binding energy is greater than in a bulk semiconductor (up to 20–30 meV in GaAs/GaAlAs structures[3,4]). The binding energy and oscillator strengths of an excitonic transition can be substantially increased by replacing the semiconductor barriers with insulators having much lower permittivities than the semiconductor.[5–7]

For semiconductor–insulator QWs, the dielectric enhancement of excitons, predicted in Ref. 8, can be explained by the fact that although both charges (electron and hole) are located in the semiconductor wire, the Coulomb interaction energy is concentrated in the insulator because of the large difference of the permittivities (the electric field lines connecting the electron and hole partially or, for thin wires, mainly pass

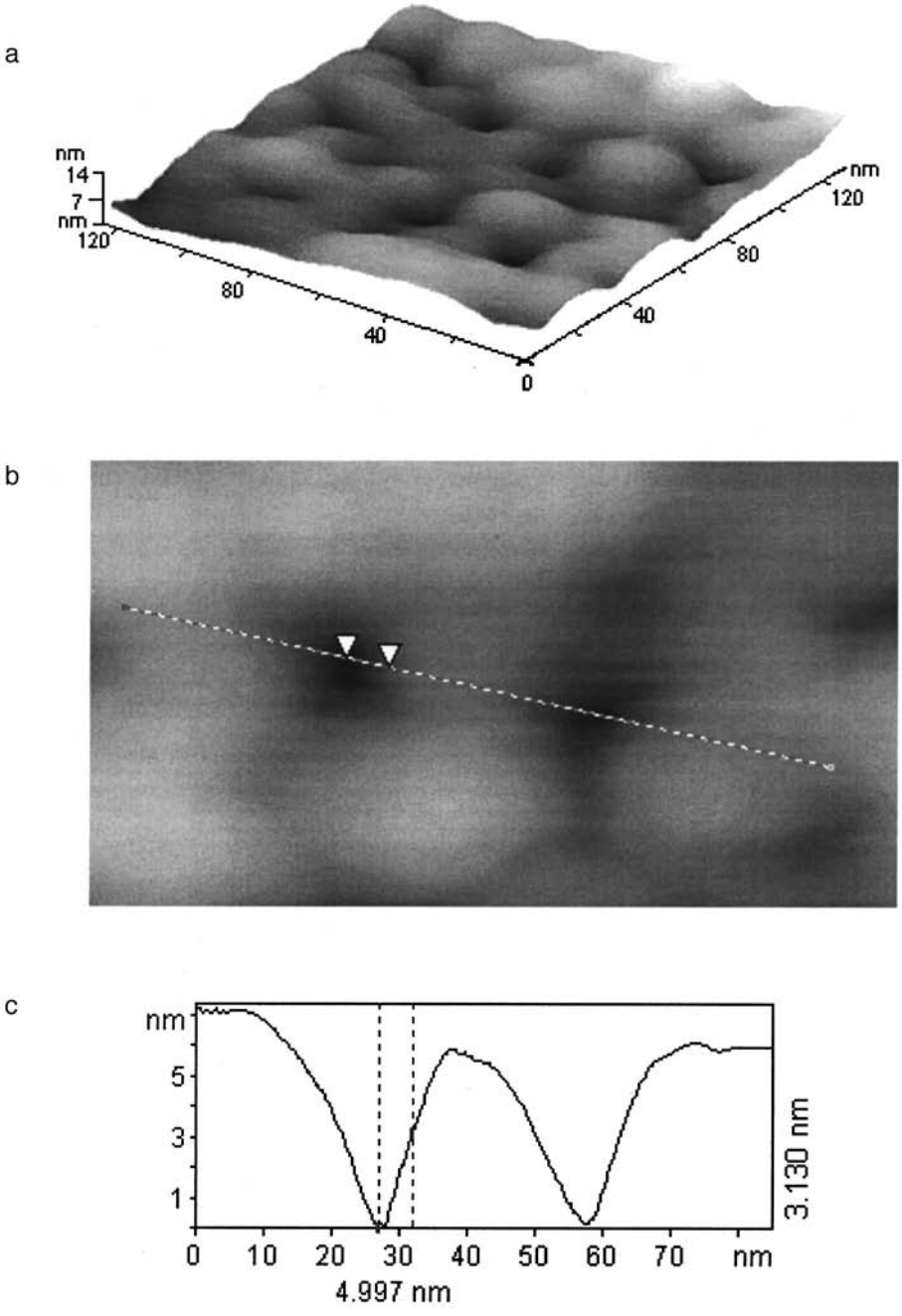

FIG. 1. (a, b) Atomic force microscope image of the surface of the template — porous Al_2O_3 and (c) profile of a section of the surface in the direction indicated in the fragment (b).

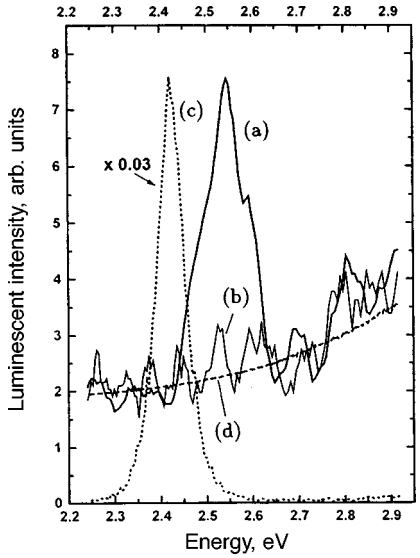

FIG. 2. Photoluminescence spectra of CdS nanocrystals crystallized in hollow channels of an Al_2O_3 insulating matrix, measured at room temperature with pump radiation polarized at angles 45° (a) and 90° (b) with respect to the direction of the channels in the matrix, as well as the spectra of bulk CdS (c) and a porous Al_2O_3 matrix with hollow channels (d).

through the insulator). The binding energy and oscillator strengths of excitons in semiconductor–insulator QWs can be varied over wide limits by choosing semiconductors and insulators with different permittivities — the Coulomb interaction can be ''engineered.''[7]

In the present letter we report the results of measurements of the luminescence spectra of CdS nanostructures crystallized in hollow channels with diameters of 10–12 nm in a transparent insulating template, when the structures are excited with polarized light. The rapid increase in the luminescence intensity with excitation by light polarized along the axis of the channels, as compared with light polarized perpendicular to the axis, showed that the nanostructures crystallize predominantly in the form of QWs. The exciton parameters — the binding energy, the wave functions, and the excitonic transition energies — are calculated in a theoretical model that takes into account the size quantization of the electrons and holes and the dielectric enhancement of the excitons.

Crystallization of the semiconductor in an insulating template[9] prepared by anodic oxidation of an aluminum substrate was used to obtain the semiconductor nanocrystals. Oxidation of a substrate electropolished beforehand was conducted with a 1 mA/cm^2 dc current in a 10% solution of sulfuric acid at room temperature. CdS was formed in the resulting pores, which were approximately 10 nm in diameter and several microns long (Fig. 1), by cathodic electrodeposition in an aqueous solution of 0.1 M $Na_2S_2O_3$ and 0.1 M $CdSO_4$ at room temperature with a dc current of 1 mA/cm^2 for 300 s. The samples were annealed in vacuum for 1 h at 300 °C to permit crystallization of the CdS deposited in the pores (hollow channels in the matrix).[1)]

Figure 2 shows the luminescence spectra of samples containing CdS nanocrystals

for different polarizations of the excitation radiation. For comparison, the luminescence spectra of bulk CdS (a single crystal grown from the vapor phase) and of the insulating matrix are presented in the same figure. Comparing the spectra, we can conclude that the luminescence band with a maximum at 2.54 eV and a half-width of about 150 meV is due to CdS nanocrystals. It can be attributed either to the lowest electron–hole transition in quantum dots (QDs), to excitonic transitions in the QWs, or to transitions in nanostructures of both types. If the nanostructures are assumed to consist of QDs, then using the computed[10] dependences of the energy of the lowest electron–hole transition on the radius of the CdS QD, whose dimensions are comparable to the Bohr radius in the bulk semiconductor, the average radius (R) of the nanostructures can be determined. The energy of the luminescence band maximum corresponds to the lowest electron–hole transition in a QD with $R \approx 6$ nm. When the dielectric enhancement of the electron–hole interaction in the dielectric environment surrounding the QD is taken into account,[11] the transition energy decreases substantially and the estimated radius is 3–4 nm. These estimates agree with the measured transverse size of the template channels in which the CdS was crystallized. However, it should be noted that the well-expressed luminescence band of CdS nanocrystals arises only if the excitation radiation contains a field component parallel to the axis of the channels. This suggests that in the hollow channels of the template the nanostructures crystallize primarily in the form of wires and not quantum dots. Inside thin (nanometer size) parallel wires surrounded by an insulator, the field component of the exciting radiation perpendicular to the axis of the wire is substantially weakened as a result of the boundary conditions, which decreases the luminescent intensity and the absorption of light with such polarization.[12] Thus, we attribute the characteristic features of the spectra of the structures obtained to the luminescence of excitons in semiconductor–insulator QWs.

Figure 3 shows the theoretically computed excitonic transition energy as a function of the QW radius and the renormalized band gap of the semiconductor and the exciton binding energy. The band gap in a QW is greater than in a bulk semiconductor because of size quantization and because of the appreciable effect of the self-action potentials,[13] which lead to additional repulsion of charges from the boundary with the insulator. The electron–hole Coulomb interaction potential, which is strongly amplified by the image potentials, leads to large binding energies (about 170 meV with $R = 5$ nm) and exciton oscillator strengths. Comparing the experimentally determined excitonic transition energy 2.54 eV with the theoretically computed values (Fig. 3, curve a), we find that the QW radius can lie in the range 5 nm $\leqslant R \leqslant$ 15 nm. As one can see from Fig. 3, in this region substantial changes in the energy of a free transition are essentially completely compensated by changes in the binding energy. As a result, the excitonic transition energy is independent of the radius over a wide range of values of R, which largely suppresses the inhomogeneous broadening of the excitonic absorption and luminescence bands in samples with large QW-size variance. We attribute the appreciable broadening observed in the luminescence spectra (Fig. 2, curve a) to structural nonuniformities arising during growth of CdS nanocrystals. This affects primarily the parameters of the semiconductor, such as, the carrier effective masses and the band gap, on which the computed excitonic transition energy depends strongly. The parameters of bulk CdS are used in the calculations: the effective masses $m_e = 0.2m_0$, $m_h^{\perp} = 0.7m_0$, and $m_h^{\parallel} = 5m_0$, the high-frequency permittivity $\varepsilon_\infty = 5.32$, the band gap at low temperature[2)] $E_g = 2.58$ eV, and the parameters of Al_2O_3 — $\varepsilon = 1.65$ and $E_g = 3.5$ eV.

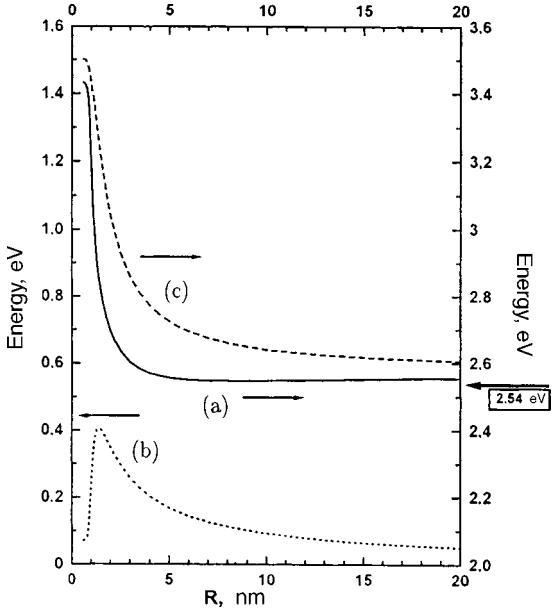

FIG. 3. (a) Theoretically computed excitonic transition energy, (b) exciton binding energy, and (c) the renormalized band gap as functions of the radius R of a cylindrical CdS quantum wire surrounded by Al_2O_3. The arrow on the right-hand side of the figure indicates the experimentally measured excitonic transition energy.

In summary, analysis of the luminescence spectra of CdS semiconductor structures crystallized in hollow channels in an Al_2O_3 insulating matrix shows that nanocrystals are formed predominantly in the form of QWs approximately 10 nm in diameter. The dielectric enhancement effect results in large oscillator strengths and binding energies of excitons in such structures. Despite the strong dependence of the exciton binding energy on the QW diameter, the excitonic transition energy is essentially constant over a wide range of diameters, which results in strong narrowing of the lines in the absorption and photoluminescence spectra of the QWs.

This work was partially supported by the Russian Fund for Fundamental Research (Grants Nos. 99-02-18327 and 97-02-17600) and by the program ''Physics of Solid-State Nanostructures'' (Grants 97-1083 and 97-1072).

*)E-mail: vlad@krfpt.ilc.msu.su

1)The formation of CdS nanocrystals was confirmed by measurements of the phonon spectra of the experimental structures by IR Fourier spectroscopy, performed by A. I. Belogorokhov and L. I. Belogorokhova.

2)In QWs the mechanism of renormalization of the band gap as a result of the electron–phonon interaction is largely suppressed because of size quantization of the phonons, which leads to a weaker temperature dependence of E_g than in a bulk semiconductor.

[1] R. Zimmermann, Jpn. J. Appl. Phys., Part 1 **34**, 228 (1995).
[2] S. Glutsch and D. S. Chemla, Phys. Rev. B **53**, 15902 (1996).
[3] W. Weigscheider, L. N. Pfeiffer, M. M. Dignam *et al.*, Phys. Rev. Lett. **71**, 4071 (1993).
[4] T. Someya, H. Akiyama, and H. Sakaki, Phys. Rev. Lett. **76**, 2965 (1996).
[5] E. A. Mulyarov and S. G. Tikhodeev, Zh. Éksp. Teor. Fiz. **111**, 274 (1997) [JETP **84**, 151 (1997)].

[6] V. S. Dneprovskiĭ, E. A. Zhukov, E. A. Mulyarov, and S. G. Tikhodeev, Zh. Éksp. Teor. Fiz. **114**, 700 (1998) [JETP **87**, 382 (1998)].
[7] L. V. Keldysh, Phys. Status Solidi A **164**, 3 (1997).
[8] N. S. Rytova, Dokl. Akad. Nauk SSSR **163**, 1118 (1965) [Sov. Phys. Dokl. **10**, 754 (1966)]; L. V. Keldysh, JETP Lett. **29**, 658 (1979).
[9] S. Bandyopadhyay, A. E. Miller, and M. Chandrasekhar, Proc. SPIE **2397**, 11 (1995).
[10] S. V. Nair, S. Sinha, and K. C. Rustagi, Phys. Rev. B **35**, 4098 (1987).
[11] T. Takagahara, Phys. Rev. B **47**, 4569 (1993).
[12] N. A. Gippius, S. G. Tikhodeev, J. Rubio *et al.*, Phys. Status Solidi B **188**, 269 (1995).
[13] E. A. Muljarov, S. G. Tikhodeev, N. A. Gippius, and T. Ishihara, Phys. Rev. B **51**, 14370 (1995).

Translated by M. E. Alferieff

New type of excitonic radiation in the solid solutions $CdS_{1-x}Se_x$

B. V. Novikov,*) N. R. Grigor'eva, R. V. Grigor'ev, and B. A. Kazennov
St. Petersburg State University, 198904 St. Petersburg, Russia

R. Schwabe and J. Lenzner
Leipzig University, Leipzig, Germany

F. Bigl, D. Hirsch, and K. Otte
Institute of Surface Modification, Leipzig, Germany

(Submitted 21 June 1999)
Pis'ma Zh. Éksp. Teor. Fiz. **70**, No. 3, 221–225 (10 August 1999)

Manifestations of bulk crystalline regions with stacking faults are detected in the reflection and photoluminescence spectra of $CdS_{1-x}Se_x$ crystals with a variety of compositions. The magnitude of the crystal-field anisotropy and the spin–orbit splitting in these crystals are estimated. It is shown that reabsorption affects the form of the photoluminescence in crystals with stacking faults. © *1999 American Institute of Physics.* [S0021-3640(99)01215-3]

PACS numbers: 78.55.Et, 61.72.Nn, 71.70.Ch, 71.70.Ej, 71.35.Cc

The solid solutions $CdS_{1-x}Se_x$ are well-known model objects for investigating exciton localization by large-scale volume fluctuations of the composition.[1–3] The radiative recombination of excitons[4] and the shape of the long-wavelength absorption edge[4,5] have been studied in detail. It has been shown in a number of works that in $CdS_{1-x}Se_x$ solid solutions with a low concentration of one of the anionic components ($x=0.01$) the excitonic reflection spectrum (ERS) and the photoluminescence (PL) can be strongly altered.[6,7] This is due to exciton localization in near-surface potential wells formed by a solid solution with band gap E_g less than in the interior volume.

The question of near-surface exciton localization in $CdS_{1-x}Se_x$ solid solutions with large x remained open. To date only broadened $A,B,$ and C bands of excitons, monotonically shifting (as x changes), and characteristic PL, consisting of a localized-exciton line (zero line) and its photon replicas, have been observed in the ERS.[3,4] For this reason, our main goal in the present work was to observe near-surface radiative localization of excitons in $CdS_{1-x}Se_x$ solid solutions with a high content of anionic components. However, in the course of the investigation it was determined that there exists a different effective channel for radiative recombination of excitons. This channel is associated with structural defects in the experimental crystals.

For the investigations $CdS_{1-x}Se_x$ single crystals with $x\approx 0.15$, 0.30, and 0.50 were grown by sublimation at 950 °C. The initial mixture was initially homogenized by repeated sublimation. The maximum dimensions of the single crystals were approximately

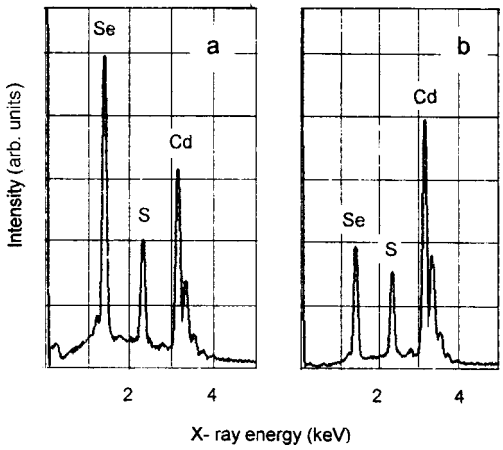

FIG. 1. X-ray emission spectra of $CdS_{50}Se_{50}$ samples for excitation by an electron beam with energy 8 keV (a) and 20 keV (b).

2×5 mm with thickness ranging from 0.1 to 1 mm. The crystals were not intentionally doped during growth. The ERS and the PL spectra were investigated from the native faces. A total of about 20 samples was investigated. The stoichiometric composition of the near-surface region of a number of the experimental crystals was investigated qualitatively. A JEOL JSM-6600 scanning electron microscope (ROENTEC-M3 x-ray detector) was used for x-ray microprobe analysis. The data were adjusted for the background and absorption of the x rays. Figure 1 shows a typical x-ray spectrum of one such sample $CdS_{1-x}Se_x$ ($x\approx0.50$) with excitation by electrons with different energies. Analysis of these spectra showed that excess Se near the surface could comprise 1–3%, and it varied in different parts of the sample within these limits.

In most experimental samples of the solid solutions the well-known ERS, polarized in accordance with the published data,[3] were observed (Figs. 2a and 2d). However, in a

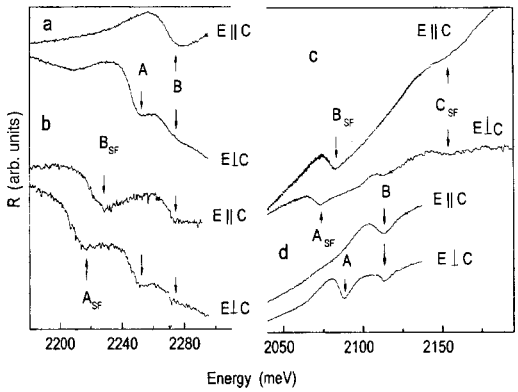

FIG. 2. Exciton reflection spectrum at $T=4.2$ K: a — classical ERS of $CdS_{70}Se_{30}$ samples; b — anomalous ERS of $CdS_{70}Se_{30}$ samples; c — anomalous ERS of $CdS_{50}Se_{50}$ samples; d — classical ERS of $CdS_{50}Se_{50}$ samples.

number of samples different reflection spectra were also observed. Their main feature was the presence of a new polarized structure (A_{SF} and B_{SF}) on the long-wavelength side of the exciton *A*. The new features of the ERS had the form of dispersion contours and were sharply polarized: $A_{SF} \perp C$, $B_{SF} \parallel C$ (Figs. 2b and 2c). The distance between the new lines (features) ranged from 5 to 15 meV in different samples. Sometimes these new lines could be observed simultaneously with the well-known ERS lines when different parts of the same crystal were investigated (Figs. 2a and 2b). In this case the $A-A_{SF}$ distance could be estimated, and it was found to be ~ 35 meV for the solid solution with $x \sim 0.30$. In some samples the new lines predominated in the spectrum. In this case another feature could be observed in the reflection spectrum, shifted from A_{SF} in the short-wavelength direction by ~ 75 meV (Fig. 2c).

We assumed initially that the new features could be due to localization of excitons near the surface of a Se-enriched crystal. In this case a potential well could arise near the surface because of the decrease in E_g.[8] However, the high intensity of the new lines in the reflection spectrum, comparable to the well-known ERS of the solid solution, their unique polarization, and the splitting led us to a different conjecture.

As is well known,[9] II–VI compounds and solid solutions based on them crystallize in the cubic (sphalerite) and hexagonal (wurtzite) lattices. The characteristic structural feature of these crystals is their tendency to form stacking faults (SF), i.e., alternation of the layers that is incorrect from the standpoint of a given sequence. The effect of the stacking faults on the ERS in II–VI compounds and their solid solutions has been investigated in detail by Suslina, Fedorov, and co-workers.[10] The appearance of stacking faults in the sphalerite structure results in splitting of the single excitonic line into a doublet with oppositely polarized components. The splitting is determined by the strength of the anisotropic crystal field.[9,10]

We assume that the additional structure which we observed in the ERS of $CdS_{1-x}Se_x$ solid solutions is due to the appearance in them of crystalline regions containing a sphalerite structure with stacking faults. This results in the appearance of a doublet of excitonic lines (A_{SF},B_{SF}) with opposite polarization. The doublet is shifted in the long-wavelength direction, since E_g for sphalerite is less than E_g for wurtzite in both CdS and CdSe. The quite large splitting of the doublet (up to 15 meV) is indicative of a strong anisotropic crystal field. This value for hexagonal structure is 17 meV in CdS and 25 meV in CdSe, varying monotonically with composition. The new short-wavelength feature in the reflection spectrum should be attributed in this case to the spin–orbit-splitoff state in a structure with stacking faults (C_{SF}).

The new features are clearly seen in the PL spectrum of crystals with stacking faults. Ordinarily, the characteristic radiation of localized excitons (L_A^0) and their phonon replicas ($L_A^{1,2}$) is observed in the PL spectrum of $CdS_{1-x}Se_x$ solid solutions at low temperatures. The zero-phonon line is shifted relative to the excitonic absorption line of the solid solution by an amount that is correlated with the exciton localization energy. In the spectra of the $CdS_{1-x}Se_x$ solid solutions with stacking faults, intense emission lines resonant with the characteristic features in the reflection spectrum are observed together with (and sometimes without) the ordinary PL of localized excitons. Figure 3 shows the PL spectrum of three such $CdS_{1-x}Se_x$ samples with $x \sim 50$. Besides the PL line L_A^0, the A_{SF} line and its phonon replicas are observed. Luminescence due mainly to stacking faults is observed in the spectrum in Fig. 3. An attenuated phonon replica from L_A^0 can

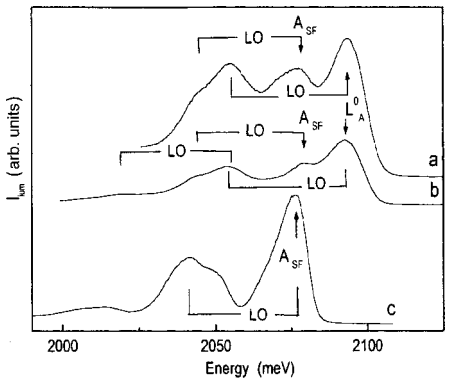

FIG. 3. Photoluminescence spectra of $CdS_{50}Se_{50}$ samples at $T=4.2$ K in $\mathbf{E} \parallel C$ polarization: a, b — PL from regions with hexagonal packing and with stacking faults; c — PL from a region with stacking faults.

also be seen in the spectrum, though the zero-phonon line is not observed, probably because it is reabsorbed. Thus, the characteristic emission line and the system of phonon replicas corresponds in the PL to crystals with stacking faults. A similar additional structure in $CdS_{1-x}Se_x$ ($x=0.15$) was observed previously in Ref. 11, but it was not attributed to stacking faults.

To clarify the role of the surface in radiative processes, the surfaces of a number of samples were treated in a polishing etchant. It is evident from Fig. 4 that after a surface layer was etched off, the zero-phonon luminescence line due to the emission of localized excitons in the hexagonal phase vanished and its phonon replicas were greatly attenuated. We believe that this could be due to localization of excitons of this crystalline phase in a surface region, as mentioned above, and to reabsorption associated with a definite relative arrangement of the layers with stacking faults and layers with a hexagonal phase. Thus for $CdS_{1-x}Se_x$ crystals with $x=0.30$, as the excitation wavelength varied from 350 to

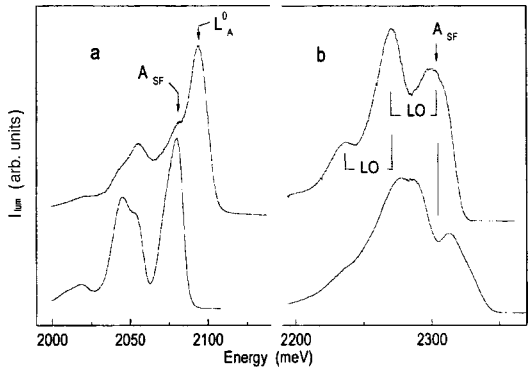

FIG. 4. Photoluminescence spectra at $T=4.2$ K: a — $CdS_{50}Se_{50}$ samples before (top) and after (bottom) etching (polarization $\mathbf{E} \parallel C$); b — $CdS_{85}Se_{15}$ samples before (bottom) and after (top) etching ($\mathbf{E} \perp C$ polarization).

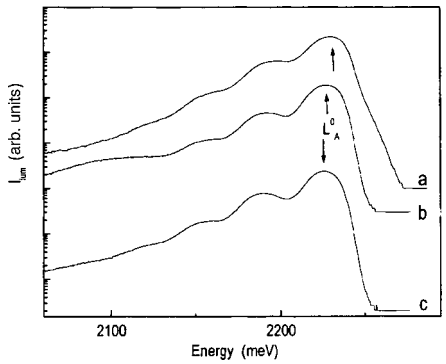

FIG. 5. Photoluminescence spectra at $T=2$ K for $CdS_{70}Se_{30}$ samples excited by a laser with the wavelength: a — 350 nm; b — 476 nm; c — 514 nm.

514 nm (i.e., as the penetration depth of light into the interior volume increased), the maximum shifted in the long-wavelength direction from 2230 to 2226 meV (Fig. 5); this is also evidence of the appearance of reabsorption.

Reabsorption effects are clearly observed in the sample with stacking faults ($x=0.15$) after treatment in a polishing etchant. A minimum at 2.30 eV (Fig. 4b, spectrum *2*), located in the excitonic resonance region, is clearly observed in the PL curve before etching. After etching in a polishing etchant, a distinct radiation peak (A_{SF}) and a distinct system of phonon replicas (Fig. 4b, spectrum *1*) arise in this region. Characteristically, the system of phonon replicas starts from the minimum of the radiation, which once again confirms the role of reabsorption processes (the radiation minimum corresponds to the maximum of the excitonic absorption line).

X-ray investigations using the method of Ref. 12 confirmed the presence of stacking faults in the samples.

In summary, the excitonic states which we observed and which are due to the existence of a phase with stacking faults along with a hexagonal phase in $CdS_{1-x}Se_x$ solid solutions play an important role in the reflection and emission processes in $CdS_{1-x}Se_x$ crystals. Reabsorption processes also play an important role in the formation of the excitonic radiation.

We thank E. P. Denisov for performing the x-ray structural analysis of the samples investigated.

*)E-mail: bono@onti.niif.spb.su

[1] E. Cohen and M. Sturge, Phys. Rev. B **25**, 3828 (1982).
[2] S. Permogorov, A. Reznitsky, V. Travnikov *et al.*, Phys. Status Solidi B **113**, 589 (1982).
[3] T. G. Zabolotnaya and M. I. Strashnikova, Ukr. Fiz. Zh. **18**, 389 (1973).
[4] S. Yu. Verbin, S. A. Permogorov, A. N. Reznitskiĭ *et al.*, Fiz. Tverd. Tela (Leningrad) **31**, 84 (1989) [Sov. Phys. Solid State **31**, 46 (1989)].
[5] A. A. Klyuchikhin, S. A. Permogorov, and A. N. Reznitskiĭ, Fiz. Tverd. Tela (St. Petersburg) **39**, 1170 (1997) [Phys. Solid State **39**, 1035 (1997)].

[6] A. A. Kiselev, B. V. Novikov, S. S. Utnasunov, and A. E. Cherednichenko, Fiz. Tverd. Tela (Leningrad) **28**, 2946 (1986) [Sov. Phys. Solid State **28**, 1655 (1986)].
[7] A. S. Batyrev, N. V. Karasenko, B. V. Novikov *et al.*, JETP Lett. **62**, 408 (1995).
[8] A. A. Kiselev, B. V. Novikov, and A. E. Cherednichenko, *Excitonic Spectroscopy of Near-Surface Regions of Semiconductors* (Leningrad State University Press, Leningrad, 1987).
[9] L. S. Markov and D. L. Fedorov, Kristallografiya **38**, 179 (1993) [Crystallogr. Rep. **38**, 229 (1993)].
[10] G. L. Bir, G. E. Pikus, L. G. Suslina, and D. L. Fedorov, Fiz. Tverd. Tela (Leningrad) **14**, 858 (1972) [Sov. Phys. Solid State **14**, 732 (1972)].
[11] V. Agekyan, R. Bindemann, R. Schwabe *et al.*, Phys. Status Solidi B **116**, K43 (1983).
[12] E. P. Denisov, A. G. Areshkin, D. L. Fedorov, and S. G. Konnikov, Fiz. Tverd. Tela (St. Petersburg) **39**, 49 (1997) [Phys. Solid State **39**, 41 (1997)].

Translated by M. E. Alferieff

Magnetically stimulated hardening of NaCl(Pb) crystals

E. V. Darinskaya and M. V. Koldaeva
Institute of Crystallography, Russian Academy of Sciences,) 117333 Moscow, Russia*

(Submitted 29 June 1999)
Pis'ma Zh. Éksp. Teor. Fiz. **70**, No. 3, 226–228 (10 August 1999)

Dislocation motion in NaCl(Pb) crystals under a pulsed mechanical load with and without a magnetic field is investigated. It is found that the dislocation mobility decreases when these crystals are deformed in a magnetic field. It is inferred that the observed magnetically stimulated hardening of NaCl(Pb) is due to a characteristic feature of spin-dependent electronic transitions in the dislocation–lead impurity system which increase the barrier for dislocation motion. © *1999 American Institute of Physics.* [S0021-3640(99)01315-8]

PACS numbers: 61.72.Lk, 75.80.+q, 81.40.Ef

The magnetoplastic effect — dislocation motion in a static magnetic field in the absence of a mechanical load in NaCl, LiF, CsI, Zn, and Al crystals — has been studied in Refs. 1–7. A detailed investigation of this phenomenon made it possible to conclude that a magnetic field gives rise to evolution of the spins in a dislocation–paramagnetic center system, concluding with spin-dependent electronic transitions in this system which sharply decrease the barrier for dislocation motion. As a result, a dislocation overcomes the barrier and then moves in the internal stress field of the crystal. A similar concept[8,9] underlies the explanation of many processes which are affected by a weak magnetic field. As was shown in Refs. 2 and 3, dislocation motion in a magnetic field in the absence of mechanical load is not observed in NaCl crystals which contain 0.5 ppm calcium and 1–100 ppm lead. This behavior of dislocations in NaCl(Pb) could be due to two factors: first, lead might harden the crystal, so that an additional mechanical load would be required for dislocation motion in a magnetic field; second, the magnetic field might create conditions which impede dislocation motion. This letter is devoted to a study of dislocation mobility in NaCl(Pb) crystals in a magnetic field under an additional mechanical load.

We investigated the mobility of fresh dislocations in annealed NaCl(Pb) crystals containing 0.5 ppm Ca and 10 ppm Pb and in NaCl(Ca) crystals containing a Ca impurity in concentrations not exceeding 10 ppm, deformed in a static magnetic field $B=0.3$ T. A special setup was devised to produce the pressure pulses.[10] Trapezoidal pulses with a 5 min plateau were used (insets in Figs. 1 and 2).

It has been observed previously[2,3] that dislocation mobility in a magnetic field depends on the relative orientation of the dislocation, its Burgers vector, and the magnetic induction vector. Dislocations parallel to the magnetic induction vector are stationary in a magnetic field. Therefore the mobility of two types of dislocations can be investigated

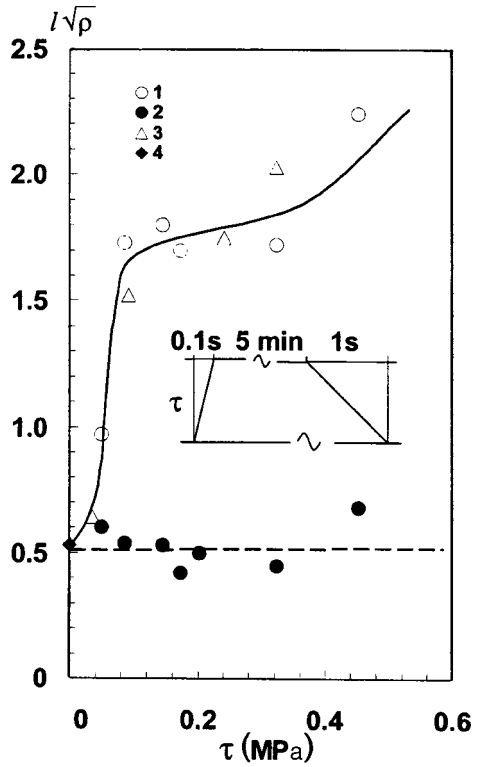

FIG. 1. Average normalized travel distance $l\sqrt{\rho}$ of dislocations versus the shear stress τ for NaCl(Pb) crystals ($B=0.3$ T, $t=5$ min): *1* — L_1 dislocations whose mobility is unaffected by a magnetic field, *2* — L_2 dislocations whose motion is affected by a magnetic field, *3* — control experiments in the absence of a magnetic field, *4* — triple background etching. Inset: Form of the mechanical pulse.

simultaneously when a sample is deformed by a mechanical pulse in a magnetic field: L_1 dislocations, whose motion is unaffected by a magnetic field, and L_2 dislocations, whose mobility is affected by a magnetic field. Control experiments were performed on samples deformed in the absence of a magnetic field. Repeated selective etching was used to reveal the dislocations. The measurements of the travel distances were performed under a Neophot-2 microscope. Since the dislocation density ρ in the samples is different, the average travel distance l was normalized to the distance between dislocations $1/\sqrt{\rho}$. The experimental error from sample to sample was 15%.

Figure 1 shows the dislocation travel distances versus the amplitude of the load pulse for the two types of dislocations in NaCl(Pb) crystals. It is evident that the travel distance of L_1 dislocations (solid curve), whose motion is not influenced by a magnetic field, is almost three times longer than the travel distance of L_2 dislocations (dashed line), whose mobility is influenced by a magnetic field. In the latter case, the travel distance remains essentially at the background level (point *4*) due to etching away of the surface stops.[11] The results of the control experiments (points *3*) performed without a magnetic field fall well on the curve *1* in Fig. 1.

For comparison, the analogous dependences for a NaCl(Ca) crystal (with a Ca

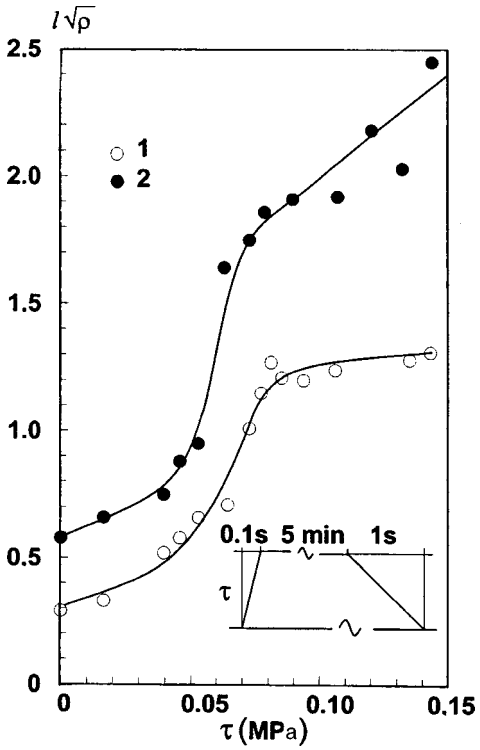

FIG. 2. Average normalized travel distance $l\sqrt{\rho}$ of dislocations versus the shear stress τ for NaCl(Ca) crystals: *1* — no magnetic field, *2* — simultaneous action of a mechanical load and a magnetic field $B=0.3$ T; $t=5$ min. Inset: Form of the mechanical pulse.

impurity), where a magnetoplastic effect in the absence of an additional mechanical load was observed previously,[3,4] are shown in Fig. 2. One can see that a magnetic field increases the dislocation travel distance under a pulsed deformation of the NaCl(Ca) crystals. It is seen in Fig. 1 that the presence of a lead impurity in NaCl(Pb) decreases the dislocation mobility in a magnetic field. This seems to be due to the specific nature of the spin-dependent electronic transitions in the dislocation–lead impurity system, which increase the barrier for dislocation motion.

In summary, our investigations show that the plastic properties of crystals in a magnetic field depend on the impurity composition. The nature of this phenomenon, just as for the positive and negative photoplastic effects,[12,13] is due to a change in the state of the electronic subsystem of the crystals.

We are grateful to V. I. Al'shits for a discussion of the results obtained, to V. P. Kisel' for annealing the crystals, and to the Research Institute of Solid-State Physics and Optics of the Hungarian Academy of Sciences (Budapest) for the NaCl(Pb) crystals. This work was supported by Grant 97-02-16327 from the Russian Fund for Fundamental Research.

*)E-mail: public@mechan.incr.msk.su

[1] V. I. Alshits, E. V. Darinskaya, T. M. Perekalina, and A. A. Urusovskaya, Fiz. Tverd. Tela (Leningrad) **29**, 467 (1987) [Sov. Phys. Solid State **29**, 265 (1987)].
[2] V. I. Alshits, E. V. Darinskaya, and E. A. Petrzhik, Izv. Vyssh. Uchebn. Zaved. Chernaya Metallurgiya **10**, 85 (1990).
[3] V. I. Alshits, E. V. Darinskaya, O. L. Kazakova *et al.*, Y. Alloys. Comp. **211/212**, 548 (1994).
[4] V. I. Alshits, E. V. Darinskaya, O. L. Kazakova *et al.*, Mater. Sci. Eng., A **234-236**, 617 (1997).
[5] Yu. I. Golovin and R. B. Morgunov, Zh. Éksp. Teor. Fiz. **115**, 605 (1999) [JETP **88**, 332 (1999)].
[6] É. P. Belozerova, A. A. Svetashov, and V. L. Krasnikov, Izv. Ross. Akad. Nauk, Ser. Fiz. **61**, 291 (1997).
[7] V. I. Alshits, N. N. Bekkauer, A. E. Smirnov, and A. A. Ursovskaya, Zh. Éksp. Teor. Fiz. **115**, 951 (1999) [JETP **88**, 523 (1999)].
[8] Ya. B. Zel'dovich, A. L. Buchachenko, and E. L. Frankevich, Usp. Fiz. Nauk **155**, 3 (1988) [Sov. Phys. Usp. **31**, 385 (1988)].
[9] A. L. Buchachenko, R. Z. Sagdeev, and K. V. Salikhov, *Magnetic and Spin Effects in Chemical Reactions* [in Russian] (Nauka, Novosibirsk, 1978).
[10] M. V. Koldaeva, E. V. Darinskaya, and V. N. Sytin, Prib. Tekh. Éksp. **3**, 151 (1998).
[11] V. B. Pariĭskiĭ, A. I. Landau, and V. I. Startsev, Fiz. Tverd. Tela (Leningrad) **5**, 1377 (1963) [Sov. Phys. Solid State **5**, 1002 (1963)].
[12] Yu. A. Osip'yan and I. B. Savchenko, JETP Lett. **7**, 100 (1968).
[13] Yu. A. Osip'yan and M. Sh. Shakhsaidov, Fiz. Tverd. Tela (Leningrad) **15**, 3711 (1973) [Sov. Phys. Solid State **15**, 2475 (1973)].

Translated by M. E. Alferieff